Leonhard Treiber, BSc

A transient absorption spectroscopy setup to study the isomerisation of aminoazobenzene

MASTER'S THESIS

to achieve the university degree of

Diplom-Ingenieur

Master's degree programme: Technical Physics

submitted to

Graz University of Technology

Supervisor:
Assoc.-Prof. Dipl.-Ing. Dr. Markus Koch

Institute of Experimental Physics

Graz, September 2018

Affidavit

I declare that I have authored this thesis independently, that I have not used other than the declared sources/resources, and that I have explicitly indicated all material which has been quoted either literally or by content from the sources used. The text document uploaded to TUGRAZonline is identical to the present master's thesis.

Graz, _____   _____

            Date   Signature

Eidesstattliche Erklärung

Ich erkläre an Eides statt, dass ich die vorliegende Arbeit selbstständig verfasst, andere als die angegebenen Quellen/Hilfsmittel nicht benutzt, und die den benutzten Quellen wörtlich und inhaltlich entnommenen Stellen als solche kenntlich gemacht habe. Das in TUGRAZonline hochgeladene Textdokument ist mit der vorliegenden Diplombarbeit identisch

Graz, am _____   _____

            Datum   Unterschrift

Abstract

A femtosecond transient absorption spectroscopy setup was planned, built and characterized, in order to study and compare the isomerisation dynamics of aminoazobenzene in solution and as thin film. Trans aminoazobenzene undergoes isomerisation to its cis configuration after excitation with light at $\sim$390 nm to the S_2 state ($\pi\pi^*$). This molecular rearrangement can be used to build a photo-active switch. Thin film switches of such kind were successfully produced by the group of Assoc. Prof. Anna Maria Coclite at the TU Graz Institute of Solid State Physics. To understand underlying isomerisation dynamics, pulses of a commercial femtosecond laser system with 25 fs pulse duration centered at 800 nm are split into pump and probe. The pump pulse is frequency up-converted to 400 nm using a LBO crystal and pumps the transition ($\pi\pi^*$) that leads to isomerisation. To get information about dynamics happening after excitation the probe pulse is sent into a CaF_2 window to generate a white light continuum (wlc) that spreads the whole visible spectrum up to the ultra violet (UV), $\sim$(320 to 800) nm. The time dependent change of probe light absorption due to the presence of the pump is measured. The molecule relaxes from S_2 to the first excited state S_1 (dipole forbidden from the ground state $n\pi^*$) and further down to the cis or trans ground state. If isomerisation to the cis isomere occurs new transitions ($n\pi^*$), ($\pi\pi^*$) arise. Results of dynamics in solution are in agreement with values found in literature. A new absorption band at $\sim$(320 to 350) nm that has not been documented in literature is assigned to the cis ($\pi\pi^*$) transition. The detection limit of the transient absorption setup was determined to be 1 mOD for pump-probe measurements in solution. The sensitivity turned out to be sufficient to measure the static absorption of the aminoazobenzene thin films, but not their time-resolved change. This is mainly due to a power drift of the laser system and the fact, that the thin films are not homogeneously spread on the substrate. Nevertheless results on thin films offer suggestions for more sophisticated detection methods to further improve the signal-to-noise ratio, which will be the topic of future research.

Kurzfassung

Ein Femtosekunden transiente Absorption Spectrometer Aufbau wurde geplant, gebaut und charakterisiert, um die Isomerisationsdynamiken von Aminoazobenzene in Lösung und als Dünnschicht zu messen und zu vergleichen. Nach Anregung von trans Aminoazobenzene mit Licht der Wellenlänge $\sim$390 nm zum S_2 Zustand ($\pi\pi^*$), isomerisiert es in die cis Konfiguration. Diese molekulare Umstrukturierung kann verwendet werden um photo-aktive Schalter zu bauen. Dünnschicht-Schalter dieser Art wurden erfolgreich von Assoc. Prof. Anna Maria Coclite und ihrer Gruppe am TU Graz Institut für Festkörperphysik produziert. Um die grundlegenden Isomerisationsdynamiken zu verstehen werden Pulse eines kommerziellen Femtosekunden-Laser-Systems mit 25 fs Pulsdauer und zentraler Wellenlänge 800 nm in Pump und Probe aufgespalten. Der Pumppuls wird in einem LBO Kristall frequenzverdoppelt zu 400 nm und pumpt den ($\pi\pi^*$) Übergang, welcher zu Isomerisation führt. Um Informationen über die Dynamiken nach Anregegung zu erhalten, wird der Probe Puls in ein CaF_2 Fenster geschickt um ein Weisslicht-Kontinuum zu erzeugen, welches das gesamte sichtbare Spektrum bis zum Ultravioletten (UV) $\sim$(320 to 800) nm abdeckt. Die zeitabhängige Änderung der Absorption des Probe Lichtes in Gegenwart des Pumpes wird gemessen. Das Molekül relaxiert vom S_2 Zustand in den ersten angeregten S_1 (Dipol verboten vom Grundzustand $n\pi^*$) und weiter in den trans oder cis Grundzustand. Falls Isomerisation in das cis Isomer auftritt, entstehen neue Übergänge ($n\pi^*$), ($\pi\pi^*$). Ergebnisse der Dynamiken in Lösung stimmen mit Literaturwerten überein. Eine neue Absorptionsbande bei $\sim$(320 to 350) nm wird dem cis ($\pi\pi^*$) Übergang zugeschrieben und wurde meinem Kenntnisstand zufolge bisher nicht in transienter Absorption gemessen. Das Detektionslimit des transiente Absorption Pump-Probe Aufbaues für Lösungsexperimente ist 1 mOD. Die Auflösung genügt um statische Absorption der Aminoazobenzen-Dünnschichten zu messen, jedoch nicht für deren zeitabhängige Absorptionsänderung. Dies tritt vor allem wegen Leistungsschwankungen des Laser Systems und aufgrund der Tatsache, dass die Dünnschichten nicht gleichmäßig auf dem Substrat verteilt sind auf. Dennoch bieten die Dünnschicht-Ergebnisse Vorschläge für erweiterte Messmethoden um das Signal-Rausch Level zu verbessern. Dies wird der Inhalt weiterer Forschung.

Contents

CHAPTER 1

Introduction

1.1 Benefits of Transient Absorption Spectroscopy

In order to measure ultrafast phenomena a variety of techniques have been established in past decades. Generally, one can distinguish two approaches. One can ask questions about relaxation dynamics and potential energy surfaces of isolated molecules or of molecules interacting with their environment. Photoelectron/photoion spectroscopy, for instance, is a standard method to measure relaxation dynamics of isolated systems in gas phase. The optical density (OD) is very low and due to its ionising character, the studied molecule/atom is irreversibly modified. Nevertheless it is an excellent technique for finding answers to fundamental problems in relaxation dynamics. Transient absorption spectroscopy on the other hand offers a "softer" interaction of light with the system of interest. In the best case, the system relaxes back into its ground state, after measurement and no damage has been inflicted on the sample. But most importantly, transient absorption spectroscopy can measure dynamics of molecules interacting with the environment and is therefore a reasonable technique to measure ultrafast phenomena of thin films, solutions or materials that cannot be studied in gas phase.

1.2 Transient Absorption

Transient absorption is a widely used technique, a detailed treatment of the underlying principles and how to establish a setup can be found in reference [1, 2]. As the name implies, transient absorption is the time dependent change of absorption after excitation of the system. By definition absorption is the change of light intensity $\mathrm{d}I$, traveling a distance $\mathrm{d}x$ in matter. It is equal to the material dependent effective cross-section for excitation σ (cm^2) times the density of absorbing particles n ($\frac{\mathrm{molecules}}{\mathrm{cm}^3}$) times the initial intensity I ($\frac{\mathrm{W}}{\mathrm{cm}^2}$). In molecular physics σ is

frequently expressed in MegaBarn ($1 \text{ Mb} = 10^{-}22\text{m}^2$).

$$\frac{\mathrm{d}I}{\mathrm{d}x} = -I\sigma n \tag{1.1}$$

By solving this equation, we end up with the law of Lambert-Beer,

$$\frac{I_0}{I} = \exp(\sigma n d) \tag{1.2}$$

with I_0 being the initial intensity, I the intensity after passing the sample and d the thickness of the sample. In scientific literature it is common to use concentration c ($\frac{\text{mol}}{\text{L}}$) instead of density n and the molar extinction coefficient ϵ ($\frac{1}{\text{M cm}}$, M is the molar concentration given in $\frac{\text{mol}}{\text{m}^3}$ or in $\frac{\text{mol}}{\text{L}}$), instead of the effective cross-section σ. ϵ is an empirical value and can be found in corresponding tables. Absorption is therefore defined as optical density (OD),

$$\text{OD} = \log_{10}(\frac{I_0}{I}) = \epsilon c d. \tag{1.3}$$

The relationship,

$$\sigma n = \epsilon c \cdot \ln(10), \tag{1.4}$$

emphasises, that one has to be very careful which units are used in literature.

Transient absorption measures time and wavelength dependent change of OD (ΔOD) after an excitation or other interaction of light with the system of interest.

$$\Delta\text{OD}(\lambda, t) = \log_{10}\frac{I_0(\lambda)}{I_{\text{pumped}}(\lambda, \Delta t)} - \log_{10}\frac{I_0(\lambda)}{I_{\text{probe only}}(\lambda, \Delta t)} \tag{1.5}$$

$$= \log_{10}\frac{I_{\text{probe only}}(\lambda, \Delta t)}{I_{\text{pumped}}(\lambda, \Delta t)} \tag{1.6}$$

The first pulse, that interacts with the system is called probe and carries very little pulse energy as to reduce perturbations of the system. Part of the beam is absorbed, depending on its wavelength. The measured intensity equals I in equation 1.3 and is not to be confused with I_0. As seen in equation 1.6, I_0 is not necessary to measure ΔOD. Next, additionally a second strong laser pulse is sent to interact with the system and perturb it. In its presence, the absorption of the probe pulse will change as can be seen in figure 1.1. This time and wavelength dependent change of absorption of the probe pulse is measured and can give insight into relaxation dynamics of multiple vibronic states. In order to receive information of all states occupied during relaxation, the probe pulse has to carry an adequately broad spectrum. Therefore a white light supercontinuum has to be generated, as is described in section 1.3. The pump pulse has to be powerful enough to excite the sample and, depending on the material, spectrally narrow enough to only pump the desired transition.
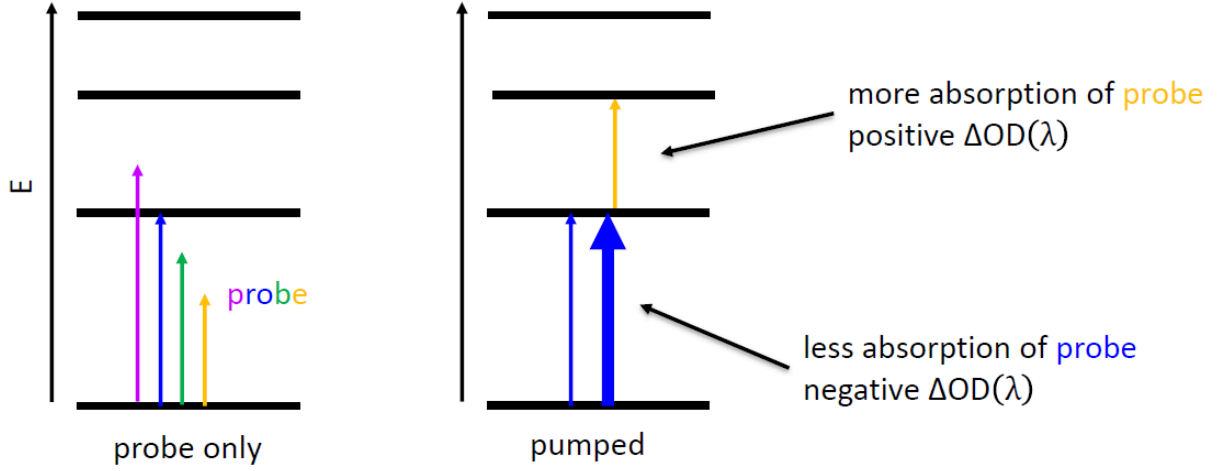
Figure 1.1: Schematic of transient absorption. Absorption of the probe pulse on the left side. Different colored arrows indicate the different frequency components. Only the "blue" part of the pulse is absorbed. On the right, change of absorption due to the presence of a strong pump pulse. As is indicated by the bold blue arrow. Since the first excited state is occupied and the ground state depleted, probe absorption changes.

1.3 White Light Continuum Generation

As mentioned above, an ultrashort spectrally broad probe pulse is needed in order to detect change in absorption (change of population) of different states. This pulse is called a white light continuum (wlc). In order to transfer energy of the used pulse centered at 800 nm to other frequencies a nonlinear process is needed. A short review of nonlinear effects will be given here. A general treatment of nonlinear effects can be found in appendix A.1.3. The electric field $\boldsymbol{E}$ of an electromagnetic wave interacts with a dielectric medium. The response to the electric field $\boldsymbol{E}$ is the polarisation $\boldsymbol{P}$. A Taylor expansion of $\boldsymbol{P}$ leads to,

$$\boldsymbol{P}(t) = \epsilon_0(\chi^{(1)}\boldsymbol{E}(t) + \chi^{(2)}\boldsymbol{E}(t)^2 + \chi^{(3)}\boldsymbol{E}^3(t) + ...),\tag{1.7}$$

with susceptibility χ and vacuum permittivity ϵ_0. $\boldsymbol{P}$ acts as a source term for the wave equation

$$\nabla^2\boldsymbol{E} - \frac{1}{c^2}\frac{\partial^2\boldsymbol{E}}{\partial t^2} = -\mu_0\frac{\partial^2\boldsymbol{P}}{\partial t^2},\tag{1.8}$$

with the speed of light c and permeability μ_0.

For a symmetric potential (centrosymmetric crystals) the $\chi^{(2)}$ effects can be neglected.

$$\boldsymbol{P}(t) = \epsilon_0(\chi^{(1)}\boldsymbol{E}(t) + \chi^{(3)}\boldsymbol{E}^3(t)).\tag{1.9}$$

The $\boldsymbol{E}^3(t)$ term can be reduced to $|E_0|^2\boldsymbol{E}$ and is therefore dependent on intensity I of the pulse ($|E_0|^2 \propto I$). Only same frequency components are regarded and $\boldsymbol{P}(t)$ can be rewritten as,

$$\boldsymbol{P}(t) = \epsilon_0(\chi^{(1)} + \chi^{(3)}I)\boldsymbol{E}. \tag{1.10}$$

The refractive index n is defined as,

$$n = \sqrt{1 + \chi} = \sqrt{1 + \chi^{(1)} + \chi^{(3)}I}. \tag{1.11}$$

A taylor expansion of χ leads to

$$n = \sqrt{1 + \chi^{(1)}} + \frac{\chi^{(3)}I}{2\sqrt{1 + \chi^{(1)}}} + \dots \tag{1.12}$$

and using $n_0 = \sqrt{1 + \chi^{(1)}}$, n can be expressed as

$$n = n_0 + \frac{\chi^{(3)}I}{2n_0}. \tag{1.13}$$

In literature this is commonly simplified as

$$n = n_0 + n_2 I. \tag{1.14}$$

This is a simplified picture, omitting four-wave mixing, which generally should be considered (see appendix A.1.3).

The effect of this nonlinear refractive index can be easily understood in time domain, if we take a look at its influence on the phase of a harmonic wave with frequency ω_0 and wave number k.

$$E(z,t) = E(0,t)\exp(i\Phi) = E(0,t)\exp(i(\omega_0 t - kz)) \tag{1.15}$$

$$= E(0,t)\exp(i(\omega_0 t - \frac{n(z,t)\omega_0}{c}z)) \tag{1.16}$$

$$= E(0,t)\exp(i\omega_0(t - \frac{n(z,t)}{c}z)) \tag{1.17}$$

Looking at equation 1.15 it is apparent, that the frequency is the time derivative of the phase,

$$\omega = \frac{\mathrm{d}}{\mathrm{d}t}\Phi = \omega_0 - \frac{\partial}{\partial t}\frac{\omega_0 n(z,t)}{c}z. \tag{1.18}$$

Therefore we see a dynamic shift in frequency $\Delta\omega$,

$$\omega = \omega_0 + \Delta\omega. \tag{1.19}$$

with $\Delta\omega \propto \frac{\partial}{\partial t}Iz$. This effect is called self-phase modulation (SPM), since the light changes the refractive index and therefore its own phase. Energy is shifted from the center frequency towards the edges.
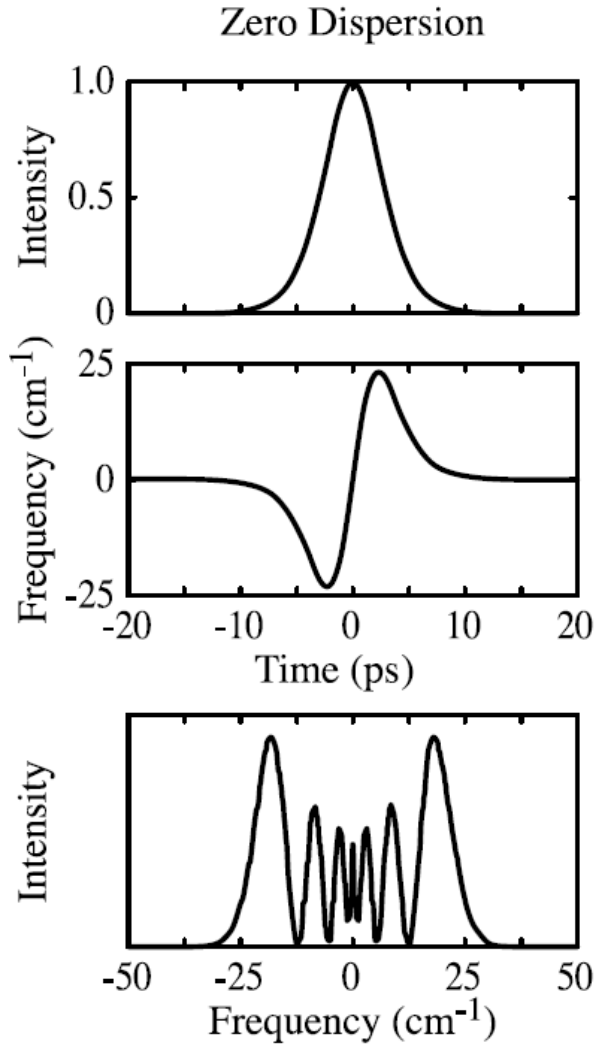
Figure 1.2: SPM effect on a Gauss pulse. Dispersion and self-steepening effects are neglected [3]

To get a qualitative understanding of this phenomenon, we take a look at figure 1.2. The short-high intensity Gauss-pulse in time domain, shifts energy from the center wavelength to higher and lower frequencies. Note that in the middle panel of figure 1.2 the leading edge results in a shift to lower frequencies (red-shift), while the trailing edge leads to a shift to higher frequencies (blue-shift). The center frequency remains unchanged. Regarding phase matching, in this simple approximation, the different frequency components are always phase matched since the product of the E-field with the complex conjugate is always phase matched.

A $\chi^{(3)}$ effect is not only apparent in frequency domain, but also in space, where it results in self-focusing, an effect that is shown in figure 1.4. The refractive index of the medium increases the further the high intensity Gauss-pulse (in space) travels in it. This is the same effect an optical lens exhibits. As the beam travels through a $\chi^{(3)}$ active medium it gets focused. If the pulse intensity is too high, thermal energy deposition on the medium will eventually lead to its destruction. The intensity dependent change of refractive index is apparent in time-domain asw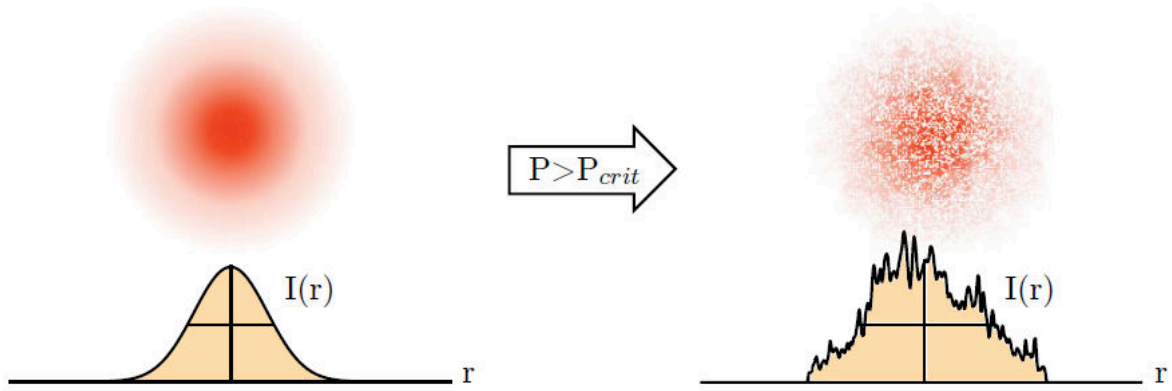ell. The high intensity peak (see figure 1.5) travels slower than the leading edge, therefore the pulse shape changes and the trailing edge is steeper than the leading. Looking at equation 1.19 we see that therefore the frequency shift is more pronounced in the blue. The white light continuum spectrum therefore is asymmetric as can be seen in figure 1.10.

Additionally at high intensities generation of free electrons arises, due to multi photon ionisation. This effect called self-trapping cancels self-focusing (refractive index < 1) and increases the beam diameter [4]. The refractive index changes by,

$$\Delta n = \frac{2\pi e^2 N_e}{n_0 m_e \omega_0^2} \tag{1.20}$$

with N_e being the electron density, m_e the electron mass and ω_0 the laser frequency [4]. This

Figure 1.3: Filamentation of a Gauss pulse with power P, original pulse intensity profile on the left and filamented intensity profile of pulse with power higher than critical power P_{crit} on the right. Adapted from reference [7] by reference [8]

is a simplification of the model introduced by reference [5]. Furthermore, there is a continuous wave ciritical power limit P_{crit}, that has to be provided for supercontinuum generation [6],

$$P_{\mathrm{crit}} = \frac{3.77\lambda_0^2}{8\pi n_0 n_2}, \tag{1.21}$$

with λ_0 being the laser wavelength and n_2 the second-order nonlinear refractive index, from equation 1.14. If the power used is a lot higher than the critical power, different parts of the pulse are self-focused and self-trapped individually and the resulting effect is called filamentation. Multiple white light continua are the result as can be seen in figure 1.3 and the output spectrum is a fluctuating mix of different components. This will eventually damage the crystal.

Until now, no dispersion effects have been regarded. Using the empirical Sellmeier equation, one can derive the Taylor expansion of the refractive index and therefore its effect on the pulse.
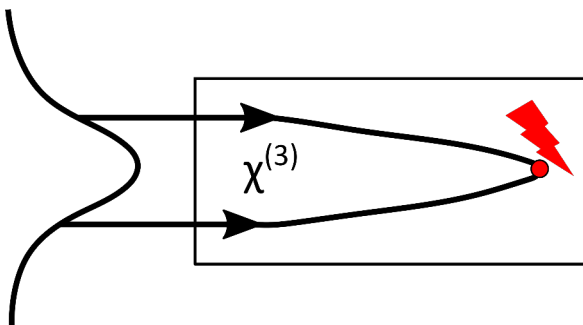

Figure 1.4: Schematic of self-focusing. The lines indicate the position of half intensity maximum.
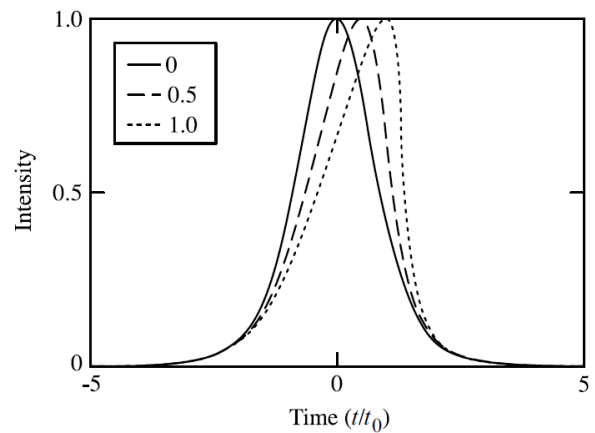

Figure 1.5: Effect of self steepening on a $\mathrm{sech}(\frac{t}{t_0})$ pulse for different self-steepening parameters $\propto z$ [3].

1.3.1 Chirp Effects

The empiric Sellmeier equation for the refractive index can be found in reference [9]. For instance, the equation for the refractive index of ethanol (λ in µm) is [10],

$$n^2(\lambda) = 1.34959 + \frac{4.0147128 \cdot 10^{-3}}{\lambda^2} - \frac{5.9411155 \cdot 10^5}{\lambda^4} + \frac{3.04975 \cdot 10^6}{\lambda^6}. \tag{1.22}$$

Since $k = \frac{\omega}{c} n$, the Taylor expansion of the additional phase in frequency domain is,

$$\phi(\omega) = k(\omega_0) + \frac{\partial k}{\partial \omega}(\omega - \omega_0) + \frac{1}{2}\frac{\partial^2 k}{\partial \omega^2}(\omega - \omega_0)^2 - \frac{1}{6}\frac{\partial^3 k}{\partial \omega^3}(\omega - \omega_0)^3 + \dots . \tag{1.23}$$

Neglecting the constant phase and the first derivative, which describes a pulse delay, the second order term,

$$\text{GVD} = \frac{\partial^2 k}{\partial \omega^2} = \frac{-\lambda^3}{\pi c^2}\frac{\mathrm{d}^2 n}{\mathrm{d}\lambda^2}, \tag{1.24}$$

with GVD the group velocity dispersion and third order term,

$$-\frac{\partial^3 k}{\partial \omega^3} = \frac{\lambda^4}{4\pi^2 c^3}(3\frac{\mathrm{d}^2 n}{\mathrm{d}\lambda^2} + \lambda\frac{\mathrm{d}^3 n}{\mathrm{d}^3\lambda^3}), \tag{1.25}$$

can be derived. For a detailed derivation see reference [3]. GVD and third order dispersion of BK7 glass is shown in figure 1.7.

The resulting electric field is

$$E(z,\omega) = E(0,\omega)\exp(i(\omega t + \phi(\omega)z)). \tag{1.26}$$

The result of these dispersion effects can best be understood by Fourier transforming equation 1.26 into time domain. Here an analytic solution for the effect of GVD can be found. The pulse duration Δt_{out} after traveling through a medium with thickness d is

$$\Delta t_{\text{out}} = \frac{\sqrt{\Delta t_0^4 + 16(\ln(2))^2(\text{GVD} \cdot d)^2}}{\Delta t_0}, \tag{1.27}$$

wirh Δt_0 the initial pulse duration. Different pulse wavelengths experience different refractive indices, thus travel at different speed. This is shown in figure 1.6. An upchip arises, meaning high frequencies occur later than low frequencies. The resulting phase and pulse broadening are presented in figure 1.8a. For third-order dispersion, a numerical Fourier transform leads to a phase and pulse shown in figure 1.8b. Third order effects are a lot weaker than second order effects, but in the resulting phase and pulse shape, we see a change due to third order dispersion. Combining second and third order effects in figure 1.9, the change of pulse width in time due to third-order dispersion is negligible but as can be seen in figure 1.9b the trailing edge gets steeper than the leading. Despite this effect, to my knowledge chirp of wlc is not corrected in transient absorption spectroscopy experiments. Using bandpass filters, only part of the white light can
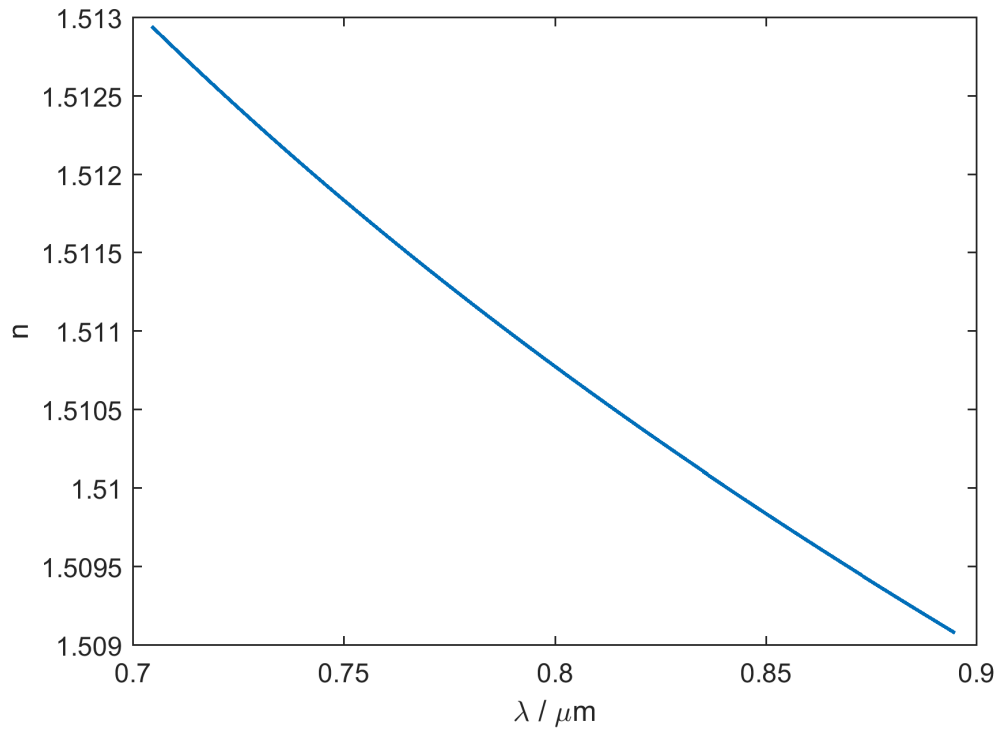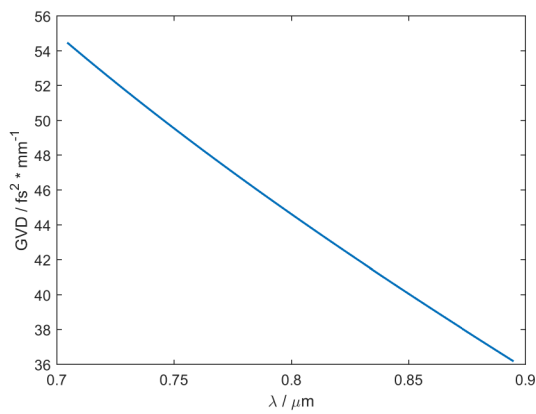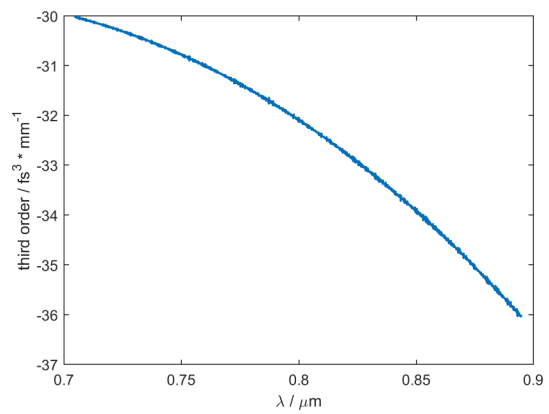
Figure 1.6: Wavelength dependent refractive index n of BK7 glass, calculated with the Sellmeier equation [11].

be used and since the probe pulse is only weakly perturbating, effects of earlier frequencies on the sample can be neglected.

(a) GVD (equation 1.24)

(b) Third order dispersion (equation 1.25)

Figure 1.7: Wavelength dependent GVD and third-order dispersion for BK7 glass, calculated from the Sellmeier equation.

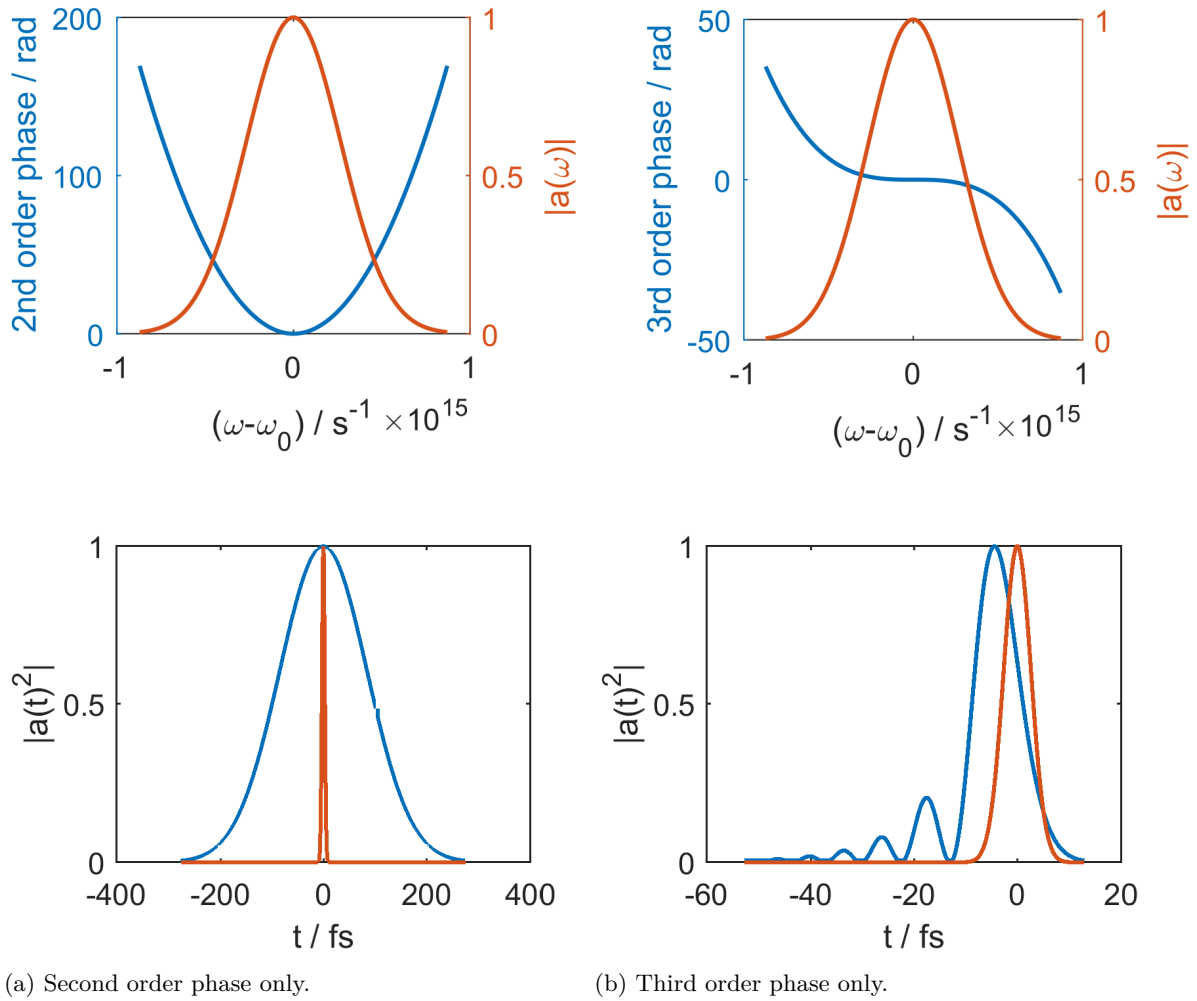(a) Second order phase only.

(b) Third order phase only.

Figure 1.8: Different dispersion effects of 10 mm BK7 glass on a Gauss pulse centered at 800 nm with a full width half maximum of 150 nm (Normalised). Initial pulse in time domain in red, resulting pulse in blue.
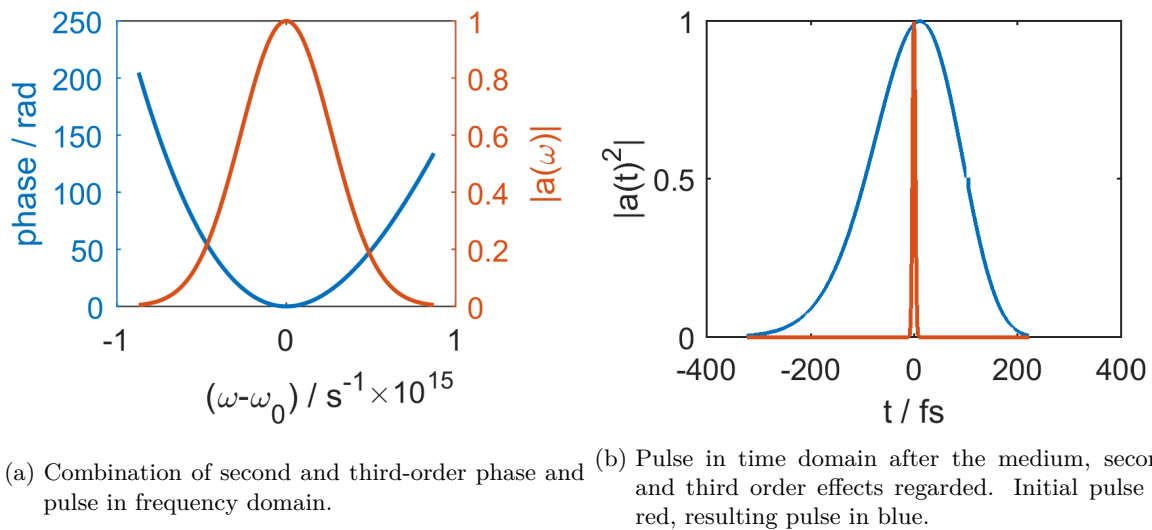

(a) Combination of second and third-order phase and pulse in frequency domain.

(b) Pulse in time domain after the medium, second and third order effects regarded. Initial pulse in red, resulting pulse in blue.

Figure 1.9: Dispersion effects of 10 mm BK7 glass on a Gaussian pulse centered at 800 nm with a full width half maximum of 150 nm (Normalised).

1.3.2 Materials for White Light Continuum Generation

A vast amount of materials generate a wlc, if they are seeded by a pulse with peak power in the order of megawatt [4]. A few examples can be found in table 1.1.

Table 1.1: Different materials for white light continuum generation, with their respective short wavelength limit, for a pump pulse centered at 800 nm.

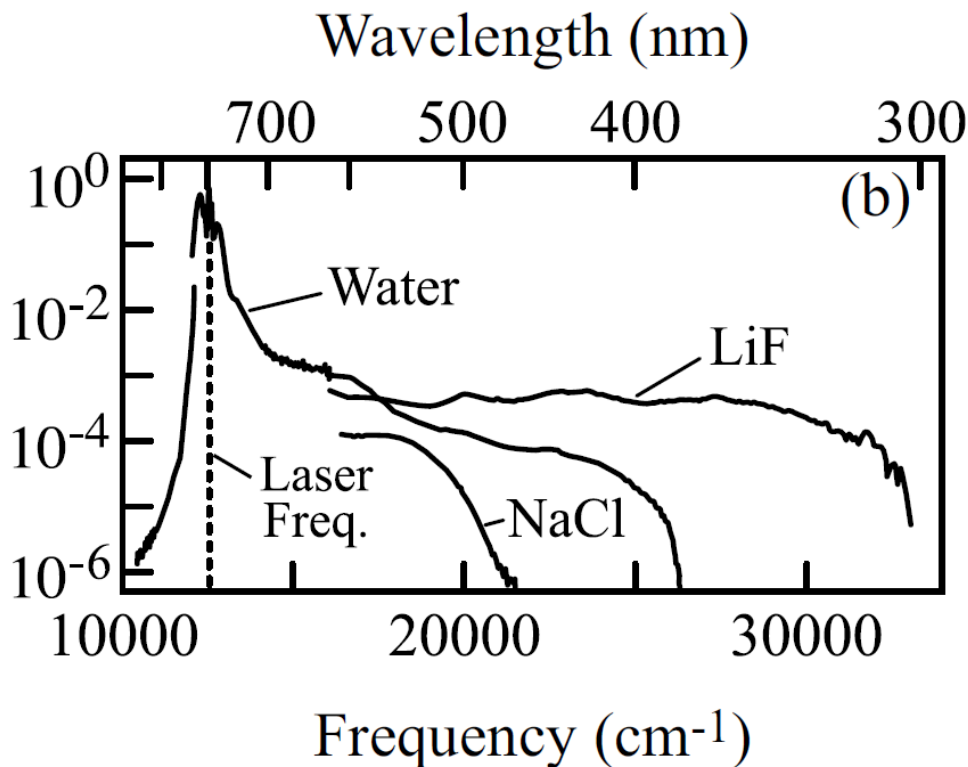| Material	Short wavelength limit / nm
Sapphire	440[12]
Water	400[4]
Fused silica	400[4]
LiF	300[4]
CaF_2	<350[2]

Figure 1.10: White light spectra of different materials. Dashed line symbolizes seed center wavelength [3].

Due to the necessity of self-focusing, the power threshold for self-focusing and wlc generation are approximately the same. Additionally to all effects discussed above, thermal energy is deposited in the medium. Therefore a material has to be either constantly moved or unaffected by the energy deposition. Sapphire for instance which is frequently used in optical parametric amplifier systems withstands the thermal energy deposition unmoved. Unfortunately, the continuum
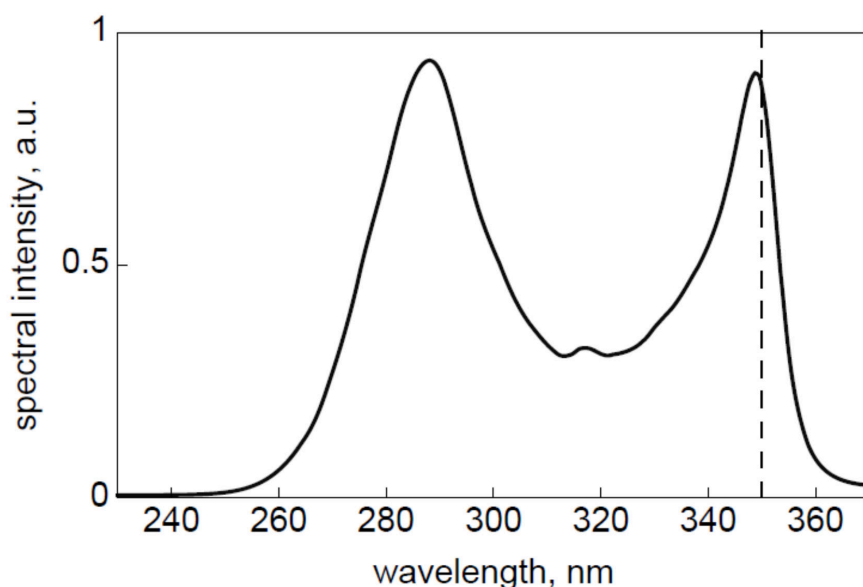
Figure 1.11: White light continuum, generated by a second harmonic ~400 nm seed in a CaF_2 window. Dashed line indicates the transmission line (350 nm of a short pass filter to remove the seed [13].

stretches only down to around 440 nm. The wider the continuum spectrum spreads into the UV, the higher the usability for the investigation of molecules with transitions in this range becomes. CaF_2 and LiF wlc spread further into the UV. Unfortunately CaF_2 has to be constantly moved and LiF is not commercially available. If a narrow continuum is sufficient for the system of interest, H_2O is a safe choice, since no crystal axis orientation has to be regarded and thermal degradation is easily avoidable. If a wlc spreading far into the UV is necessary, using the second harmonic (SH) of the initial pulse as seed is an easy approach. A spectrum of a wlc generated by a SH seed can be found in figure 1.11, the absorption limit of the medium has to be kept in mind.

1.4 Magic Angle

As introduced in equation 1.6, a certain time passes after the sample is pumped. During this time before probing, the transient dipole moment of the sample might change due to a rotation of the molecule or anisotropic effects. This may lead to an altered signal of the probe pulse. A detailed discussion can be found in reference [14], here a short explanation will be given. As indicated in figure 1.12 pump and probe are polarised by an angle χ with respect to an arbitrary axis. Further due to the non-collinear setup they also intersect at an angle β at the sample. We are interested in the probability, that the system is pumped from the ground state into an excited state (probabilty p_{pu}) and further probed from this state to a higher excited state (probability p_{pr}). The total probability will be the product of both. After pumping, the transient dipole moment may

Figure 1.12: Pump probe geometry setup [14].

change its direction by an angle α due to anisotropic effects. Therefore the dipole moment interacting with the probe pulse ($\boldsymbol{\mu}_{pr}$) is not representing the dipole moment initially induced by the pump pulse ($\boldsymbol{\mu}_{pu}$). The transient dipole moment of pump and probe now enclose the angle α.
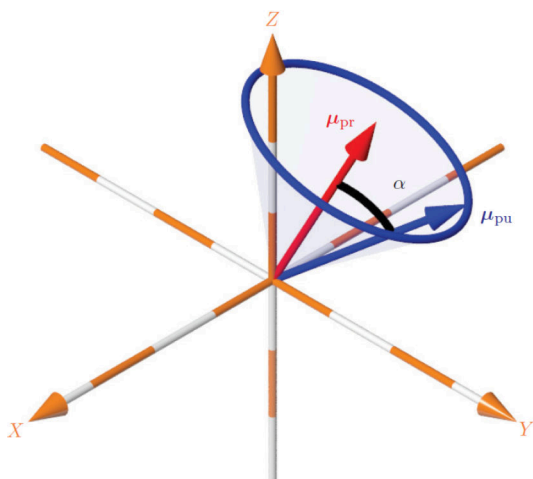

Figure 1.13: Transient dipole moments $\boldsymbol{\mu}_{pr}$ and $\boldsymbol{\mu}_{pu}$, that enclose an angle α due to anisotropic effects. All projections of $\boldsymbol{\mu}_{pu}$ on $\boldsymbol{\mu}_{pr}$ lie on the blue circle [14].
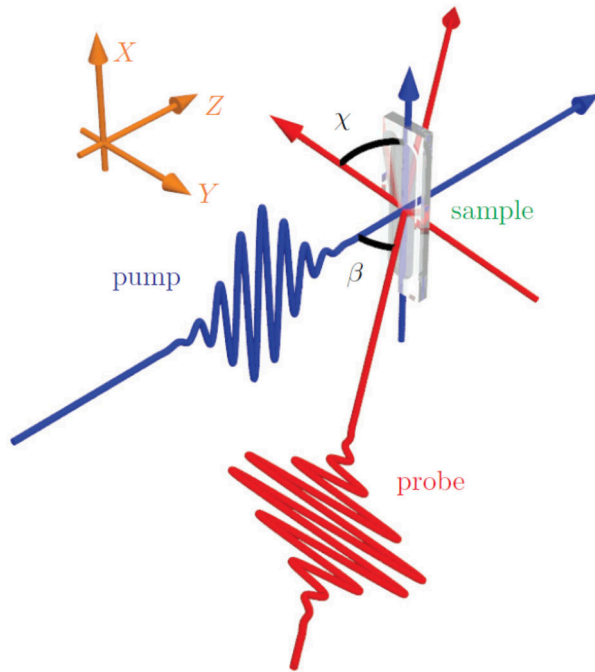
As can be seen in figure 1.13, the projection of the pump dipole moment on the probe dipole moment is the same for all pump dipole moments on the circle indicated in blue. Looking at figure 1.14, we see that for $\alpha = 0°$ the resulting transient dipole moment exhibits the well known form, whereas in the case of $\alpha = 90°$, the dipole moment is the unperturbed one tilted by 90° around the Z-axis and rotated around the X-axis. Solving for the total probability, one can find a solution, that is independent of anisotropic effects, if the angle χ between pump and probe is $\sim 54.7°$, as can be seen in figure 1.15. This angle is called the magic angle.
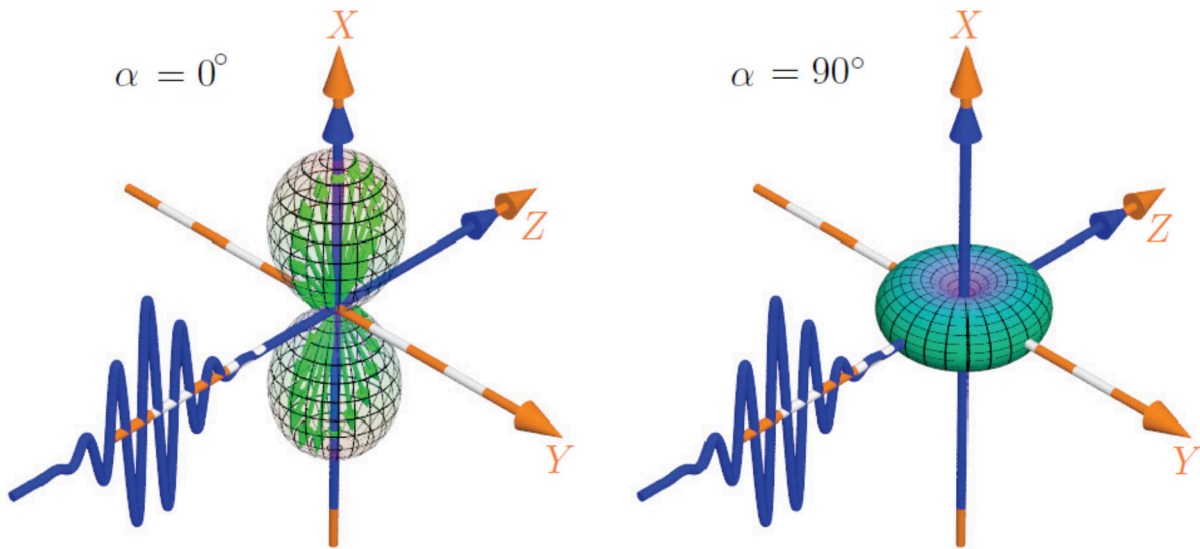
Figure 1.14: Pump probability (green vectors) of a linearly polarised pump, for different α. The probability spans a 3-D surface [14].
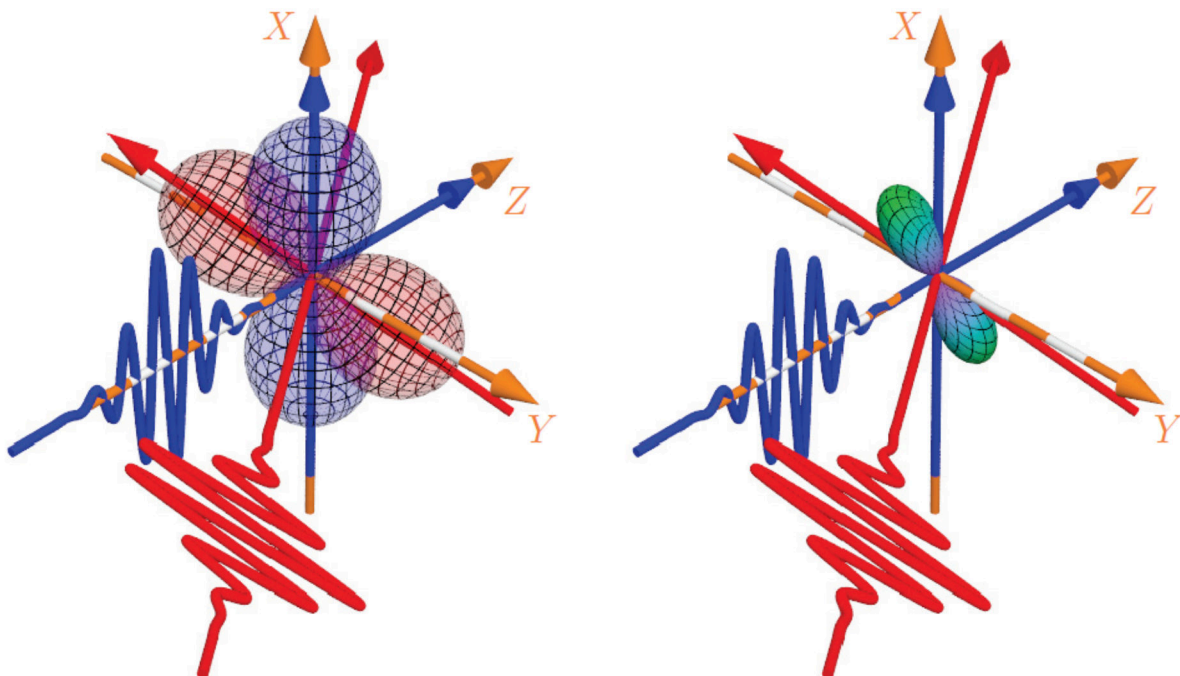

Figure 1.15: Distribution of pump (blue) and probe (red) probability on the left at the magic angle. Total probability as product of both on the right [14].
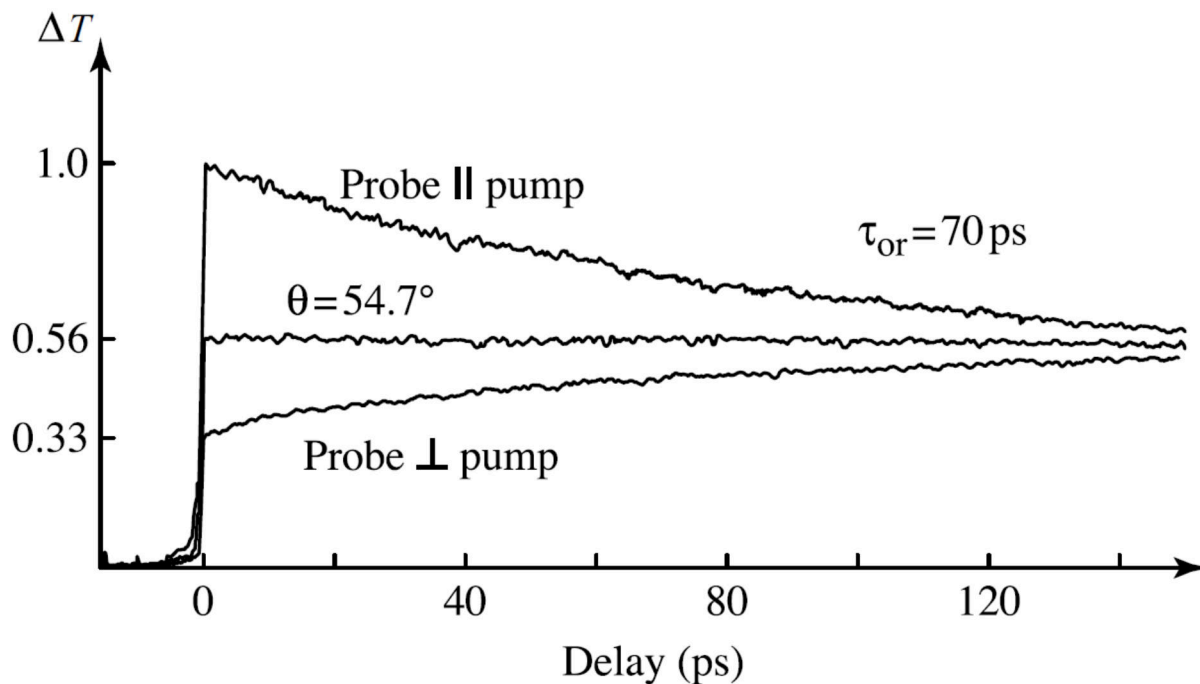
Figure 1.16: Orientation dependency of pump-probe signal ΔT for Nile blue dye [3].

The importance of a magic angle configuration can be understood by looking at figure 1.16. The pump pulse pushes population out of a certain state, the probe pulse interacts with the pumped sample and its absorption decreases (positive change of transmission ΔT). Looking at figure 1.15 it is also clear, that for a parallel polarisation of pump and probe, the pump-probe signal at time zero is the highest and decreases afterwards, since the overlap of their dipole moments is the highest and decreases due to a loss of dipole moment overlap. For the very same reason, the probe-perpendicular-to-pump signal is the lowest at the overlap, since the least amount of dipole moment overlap is present. Afterwards the signal increases since the dipole moment overlap increases. The effect of the magic angle may vary dependent on the investigated molecule but is best not ignored, since otherwise quantitative conclusions about molecular dynamics can hardly be made.

1.5 Excitation Probability for Solutions and Thin Films

Before starting a transient absorption experiment, it is adviceable to calculate the expected excitation probability p_{exc},

$$p_{\text{exc}} = n_{\text{ph}}\sigma, \tag{1.28}$$

with n_{ph} the photon density per area and σ the effective cross-section. Since σ is generally not available in literature, the molar molar extinction coefficient ϵ is used. From equation 1.2 and

equation 1.3 we can express

$$\ln(\frac{I_0}{I}) = \epsilon c d \ln(10) = \sigma n_{\text{molecules}} d, \tag{1.29}$$

with particle density $n_{\text{molecules}}$. This can be rewritten as,

$$\sigma = \frac{\epsilon c \ln(10)}{n_{\text{molecules}}}. \tag{1.30}$$

With $n_{\text{molecules}} = c \frac{N_A}{10^3}$ in cm^{-3} we get,

$$\sigma = \frac{\epsilon \ln(10) 10^3}{N_A} \quad \text{in cm}^2. \tag{1.31}$$

The photon density is dependent on the focus geometry,

$$n_{\text{ph}} = \frac{E_{\text{pump}}}{h\nu (\frac{D_0}{2})^2 \pi}, \tag{1.32}$$

with E_{pump} the pump pulse energy, h the Planck constant and D_0, the beam diameter in focus. Without derivation, D_0 of a Gauss pulse in space can be expressed as [15],

$$D_0 = \frac{4\lambda f}{\pi D_f} \tag{1.33}$$

with f, the focal length of the lens, λ the wavelength of the light and D_f the diameter of the light on the lens. This is presented in figure 1.17. In practice, the sample is frequently moved out of focus, to easily increase the beam radius. Another important variable is the wavelength λ dependent Rayleigh length z_R. z_R is the distance after which, the beam area has doubled,

$$z_R = \frac{\pi (D_0/2)^2}{\lambda}. \tag{1.34}$$

Now the total probability can be written as,

$$p_{\text{exc}} = \frac{E_{\text{pump}}}{h\nu (\frac{D_0}{2})^2 \pi} \frac{\epsilon \ln(10) 10^3}{N_A}, \tag{1.35}$$

if ϵ is given in SI units, the factor 10^3 is omitted. To give a qualitative insight on this matter we calculate the absorption probabiliy of light at 320 nm passing through a sample of azobenzene ($\epsilon = 22000 \frac{L}{\text{mol cm}}$ at 320 nm light [16]). The focus diameter is arbitrarily set to 500 µm and the pulse energy to 1 µJ. An excitation probability of $\sim$7 % is calculated. According to reference [2] the absorption probability of the pump pulse should not exceed 10 % to assure a linear signal to pump energy dependency. ϵ can be found in various papers, but often units are not declared or the solvent is not stated. Therefore the values highly differ and an independent calibration measurement might be useful.
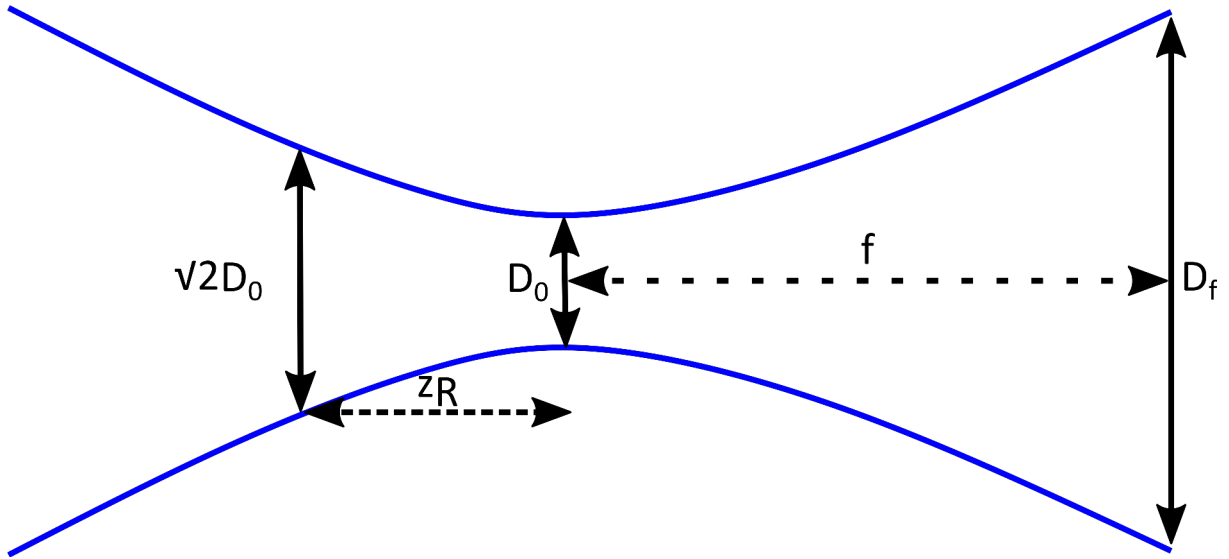
Figure 1.17: Focus geometry with beam diameter at lens D_f, focal length f, focus diameter D_0, Rayleigh length z_R.

1.6 Artifacts in Transient Absorption

Whenever one talks about ultrafast pump probe experiments, it has to be mentioned, that due to the high peak power of the pulses, always an induced response of the sample the solvent and/or the substrate must be expected. Further, the pulse duration is a key feature and most times, the bottleneck of pump-probe experiments. In the following sections a short summary of all artifacts will be given, how to avoid and what to learn from them. An overview can be found in reference [17], detailed discussions will be referenced in the corresponding subsections. In general all of the effects below increase with intensity. Further the reduction of temporal chirp of the probe will reduce cross-phase modulation effects and improve the temporal resolution. In some cases only a reference measurement of the substrate/solvent can achieve a subtraction of the artifacts. This however demands high stability of the whole setup, especially of the spatial overlap and is hard to realize.

1.6.1 Two Photon Absorption (TPA)

Once pump and probe pulse overlap in time their combined energy might meet the absorption conditions for higher states, leading to a transient absorption signal. Since the probe pulse is generally highly chirped (due to the generation process and material in its path), this signal provides direct information on the chirp and duration of the probe pulse. The cross-correlation of pump and probe $G_{\mathrm{GVD}}(t)$ can be derived as [18],

$$G_{\mathrm{GVD}}(t) = G_0 \, \exp\Big(- \frac{2.3 \ \mathrm{OD}}{\tau_{\mathrm{GVD}}} \, t \Big) \Big[\mathrm{erf}(\frac{t}{\tau} - \frac{2.3 \ \mathrm{OD} \ \tau}{2 \ \tau_{\mathrm{GVD}}}) - \mathrm{erf}(\frac{t}{\tau} - \frac{2.3 \ \mathrm{OD} \ \tau}{2 \ \tau_{\mathrm{GVD}}} - \frac{\tau_{\mathrm{GVD}}}{\tau}) \Big] \quad (1.36)$$

with τ the time of the unperturbed cross correlation, τ_{GVD} the pass time difference of pump

and probe through the medium, due to group velocity dispersion (GVD). Further the optical density (OD) of the sample, that leads to absorption of pump photons. The GVD leading to a hat like shape and the OD to a reduction of TPA. A simulation of TPA can be seen in figure 1.18.
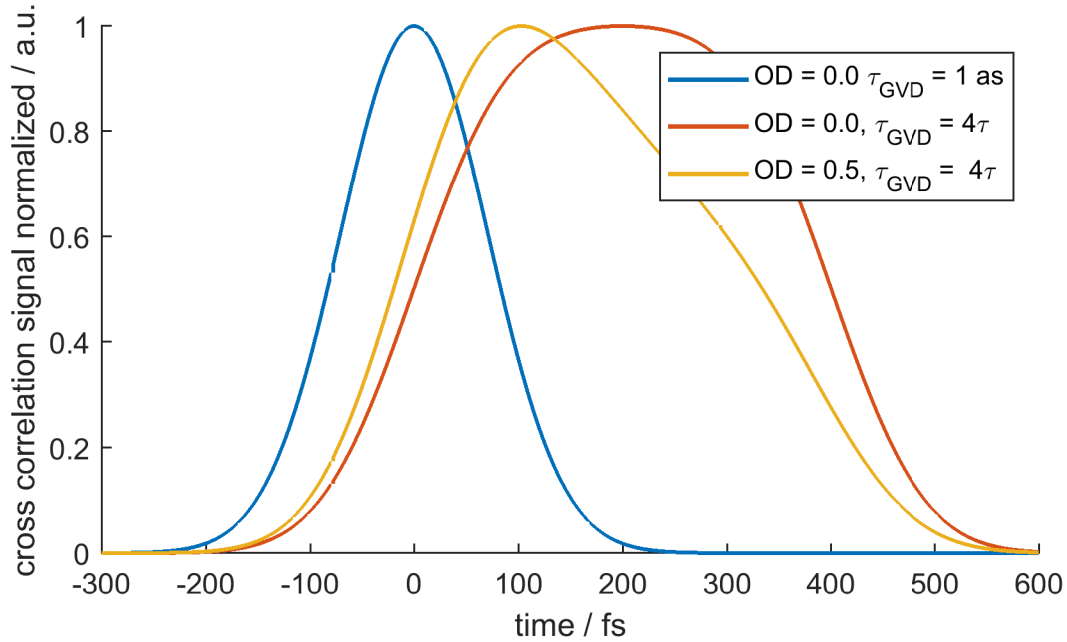

Figure 1.18: Simulation of two photon absorption with $\tau = 100\,\text{fs}$ initial correlation time.
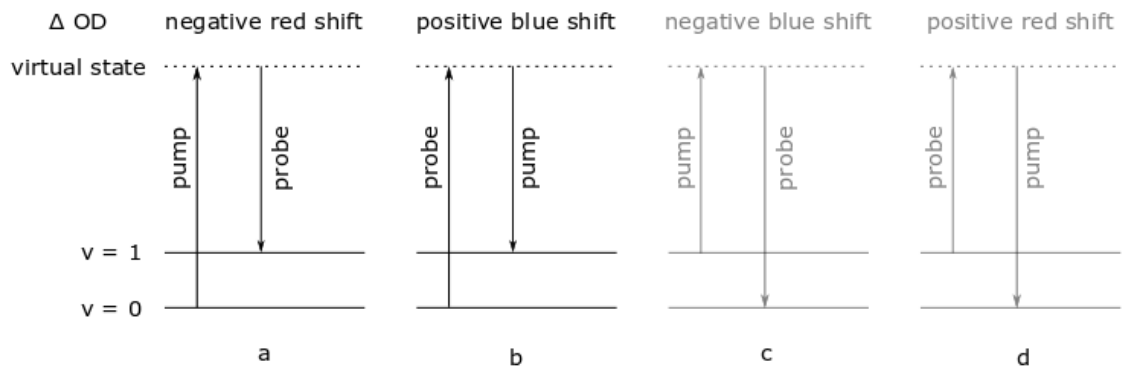
1.6.2 Stimulated Raman Amplification

Figure 1.19: Possible stimulated Raman amplification effects on the transient absorption signal. ΔOD in respect to the pump wavelength. Cases c and d are unlikely and therefore shown faded.

When pump and probe overlap in time, they might induce stimulated Raman amplification (SRA). In order to do so, their energy (wavelength) difference has to match a vibrational mode

of the medium. In general four cases are possible, that are shown in figure 1.19. If the probe pulse stimulates the transition from the virtual state to the v=1 state (case a in figure 1.19) , a pump photon is absorbed and an additional probe photon emitted, which translates to a negative ΔOD signal in the spectrum, it is called the Stokes SRA since it is shifted to the red with respect to the pump wavelength . If the pump photon carries less energy than the probe and their energy difference matches again the vibrational transition, a probe photon is absorbed and a pump photon emitted. This leads to a positive blueshifted ΔOD, called anti-Stokes SRA since it is shifted to the blue with respect to the pump wavelength (case b in figure 1.19). For the other cases, the vibrational state already has to be excited, which is highly unlikely and therefore only plotted for completeness. Although SRA occurs at the overlap and therefore requires a reference measurement and further analysis, still a lot can be learned from this signal. It gives direct information on the cross-correlation time (since it is a two photon effect). But one may take it a step further and assuming a highly chirped and compared to the pump pulse very long probe pulse, the pump pulse interacts only with a small frequency component of the probe at one time. If the pump pulse is chirped, the red part needs low energy probe photons to match the SRA condition and therefore will show negative ΔOD signal earlier than the blue part of the pump pulse, whitch is delayed in the case of an up-chirp. Now let's take a look at figure 3.6 on page 42, we do see the Stokes and anti-Stokes signal (blue circles) and that the Stokes SRA is delayed in time, due to probe chirp. Even though the SHG crystal used is 5 mm thick, the chirp is not adjusted and a lot of additional material is in the optical path, the resulting SRA signal is narrow and no time-wavelength dependency is apparent. This is not expected, since the pump is certainly highly chirped. The reason is, that due to the thick crystal, the pump spectrum is very narrow, so that the spectrometer cannot resolve the chirp. A detailed treatment of SRA can be found in reference [19], but since time resolution is not the essential feature of this first measurements, treatment of SRA has been postponed until a better time resolution is necessary. Further SRA might not be as dominant in solid samples.

1.6.3 Cross-Phase Modulation

Cross-phase modulation (XPM) is a $\chi^{(3)}$ effect very much like self-phase modulation (SPM), whose source lies in the optical Kerr effect. Now the electric field is a superposition of two waves, that influence the medium they travel through and therefore the effect of the medium on the other wave [3]. Since usually, the pump pulse has higher intensity, than the probe, it will dominate this effect. Assuming a field envelope $a(z,t) = a_1(z,t) + a_2(z,t)$ with two different frequencies ω_1, ω_2 and omitting chirp effects leads to the respective phase modulation terms for a_1 and a_2:

$$\frac{\partial a_1}{\partial z} = -i\gamma\big(|a_1|^2 + 2|a_2|^2\big)a_1 \tag{1.37}$$

$$\frac{\partial a_2}{\partial z} = -i\gamma\big(2|a_1|^2 + |a_2|^2\big)a_2 \tag{1.38}$$

with $\gamma \propto \chi^{(3)}$. Additional four-wave mixing terms $(2\omega_1 - \omega_2)$ and $(2\omega_2 - \omega_1)$ have been neglected

(for further treatment see reference [3]). The pump pulse changes the refractive index of the medium, leading to a phase modulation of the probe. The probe pulse energy therefore is redistributed between it's contained frequencies. Chirp effects have not been mentioned so far, but also play a role for a thorough understanding. A detailed treatment can be found in reference [17]. XPM pushes central frequencies of the probe towards the edges of the pulse. Thus the TA signal at the overlap shows absorption (positive signal) at the center frequencies and emission (negative signal) at the edges.

CHAPTER 2

Experimental
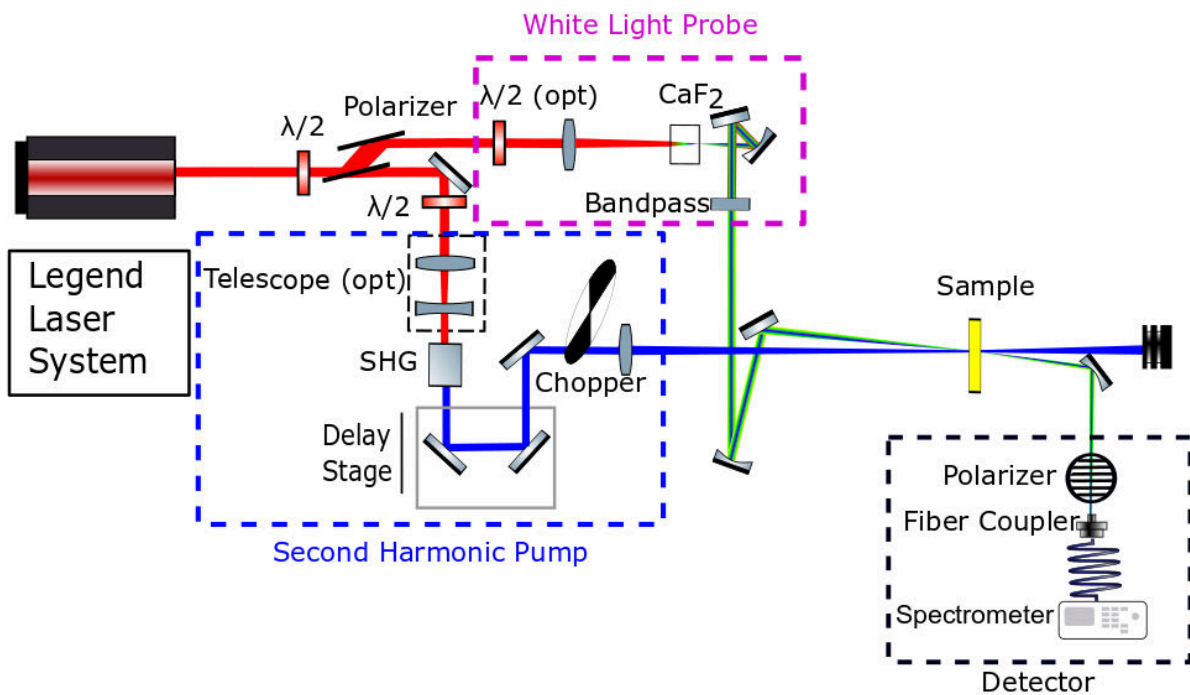
Figure 2.1: Optical setup for transient absorption measurement.

The optical setup is shown in figure 2.1, here a short overview is given. A more detailed discussion of the individual parts is carried out below, a picture of the actual setup on the optical table is shown in figure A.1. A commercial femtosecond laser system, consisting of a Ti:sapphire oscillator (Coherent Vitara) and amplifier (Coherent Legend Elite Duo) produces ∼25 fs, 4.3 µJ pulses with a repetition rate of 3 kHz. The center wavelength is 800 nm. Characterisation of

the laser pulses has already been treated in previous theses [20, 21] and will not be discussed here. Since transient absorption spectroscopy does not need high pulse energy only a small part of the systems output is used. As is indicated in reference [22] only ∼140 µJ of the pulse energy enter the setup. The beam is split at a Brewster window-polariser. The low energy part is used to generate a spectrally broad probe pulse wlc (see section 2.1), while the high energy part is magnified with a Galilean telescope and frequency doubled in a 5 mm LBO crystal. The frequency doubled second harmonic (SH) pulse is alternatingly blocked in and out using a mechanical chopper. Both beams are focused into the sample and only the spectrally broad probe is detected with a spectrometer. According to equation 1.6 the unpumped probe spectrum is compared to the pumped one and the time delay is adjusted using a translation stage.

2.1 Stable White Light Continuum Generation

Table 2.1: Parts for white light continuum generation.

Label	Company	Part-No.
F 200 mm focus lens		
CaF2 5 mm [001] cut	Newlight Photonics	CAF1050-C
(335 to 610) nm bandpass	Thorlabs	FGB37
HR800 dichroic mirror	Laser Components	45 PW1045UV
Al 75 mm concave mirror	Thorlabs	CM254-075-F01
Al 100 mm concave mirror	Thorlabs	CM254-100-F01
Fiber collimator	OZ Optics	HPUCO-2,A3-180/700-M-5BQ
FCPC to SMA fiber	Thorlabs	M91L01
Spectrometer	Ocean Optics	FLAME-S-7809422
5 axis mount	Thorlabs	K5X1

The main optical parts to generate white light continuum (wlc) can be found in table 2.1. To generate a stable white light continuum, the setup presented in reference [2] is reproduced using a 5 mm window of CaF_2. It is important to mention, that since the underlying effects are $\chi^{(3)}$ dependent, the white light efficiency is angle dependent and a rotation of the window will lead to white light fluctuations both in efficiency and polarisation [13]. Nevertheless, to prevent damage to the crystal, a motion has to be performed. Due to its simplicity a circular translation with a period of ∼3 s is used. The setup of this motion on the optical table is shown in figure 2.2. Of course any other rotation-free motion is also applicable. In the first experiments a brushed DC electric motor was used, but caused noise in the adjacent photoelectron/photoion time-of-flight setup. Therefore, an AC synchronous motor is used.

The seed energy for wlc can be precisely adjusted using a half-wave plate and two windows at Brewsters angle, which have been installed by Paul Maierhofer [20]. A focusing lens is mounted

on a translation stage and the focus is set by adjusting a micrometer screw. Once white light is generated the pulse power is decreased and the focus adjusted, this procedure is iteratively repeated. Using a 75 mm, 100 mm, 200 mm, 300 mm and 500 mm lens, it is quite impressive that with the 200 mm lens the least amount of energy ($\sim$550 nJ) is necessary to generate white light. Even though the peak intensity should be higher with a 100 mm or 75 mm lens, as can be understood by looking at equation 1.33. This might be due to differing lens qualities. To suppress white light fluctuations due to a tilt of the window during motion, an aperture is placed in front of the focusing lens, thus increasing the Rayleigh length, see equation 1.34. As trade-off the pulse energy has to be increased by about a third to get above the critical power for white light generation. The beam is recollimated using a concave mirror. To attenuate the fundamental, a HR800 dichroic mirror or a (335 to 610) nm bandpass are used, see figure 2.3. The bandpass filter performs better, especially in the UV and is therefore used for further experiments. After generation the continuum is recollimated and focused using concave mirrors (a Keplerian telescope setup). It is highly recommended to use mirrors instead of lenses to suppress chromatic aberration. To couple the beam (after it has traveled through the sample) into the fiber, a fiber collimator is used. A schematic of the fiber collimators nomenclature can be found in figure A.2. In figure 2.3 qualitative influences of the bandpass and dichroic mirror can be seen as well as the unfiltered white light.
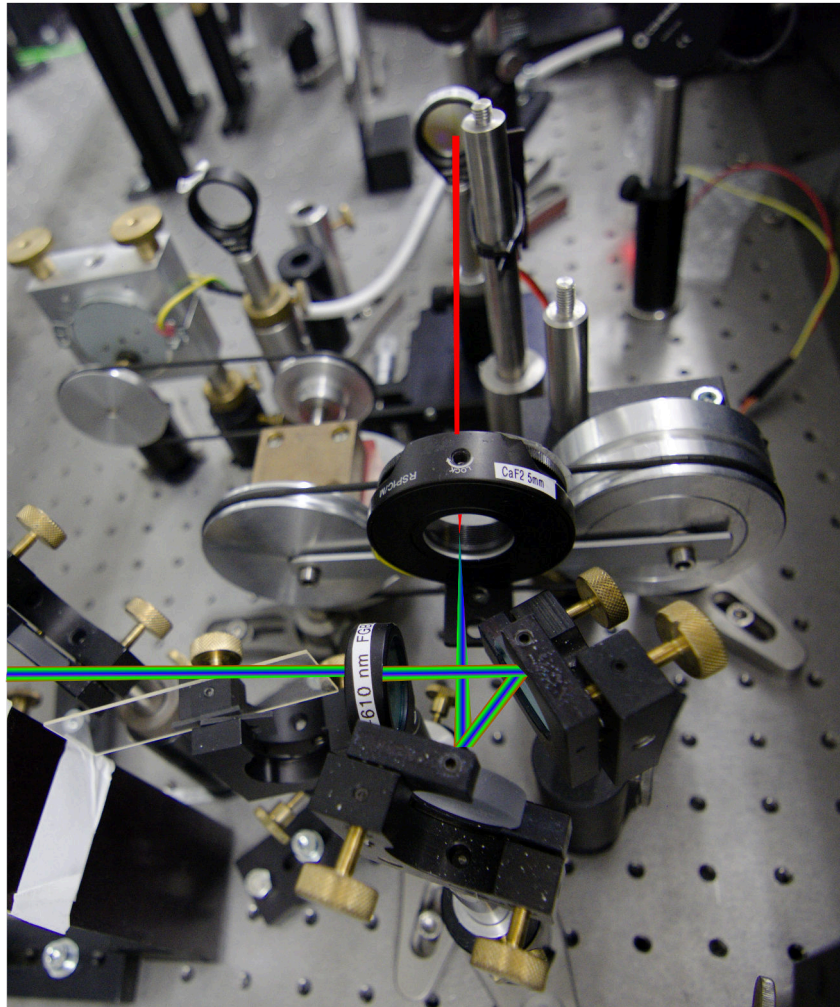
Figure 2.2: Translation setup of the CaF$_2$ window. The crystal is connected to two synchronous wheels via a rod and thus a rotation free motion is guaranteed. Sketched in red, the initial laser pulse and in rainbow colors, the generated white light continuum, that emerges the crystal.
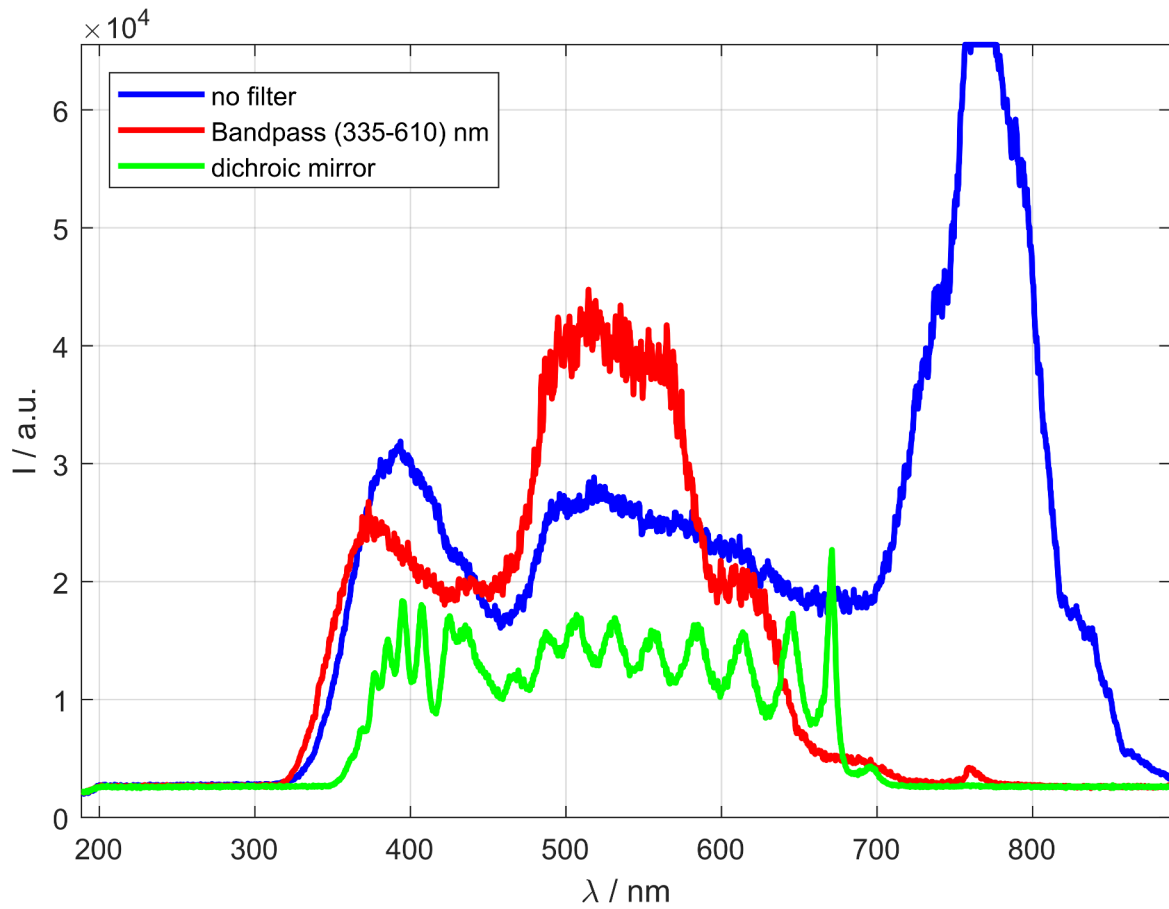
Figure 2.3: White light continuum generated in 5 mm CaF_2. Filtered and unfiltered. 200 mm focusing lens, $\sim$1 µJ seed pulse energy
unfiltered-Spectrum No: 62, dichroic mirror-Spectrum No: 42, Bandpass-Spectrum No: 40

2.2 Chopper Setup

A home-built chopper/delay-line setup including a photodiode, mounted on the chopper, is used. The chopper motor frequency can be continuously adjusted $\sim$(3 to 50) Hz and increased, depending on the number of blade-windows.

Table 2.2: Parts for chopper setup.

Label	Company	Part-No.
Photodiode	Thorlabs	DET10A/M
Chopper	Home-Built	
Delay line	Home-Built	
Arduino	Arduin0	
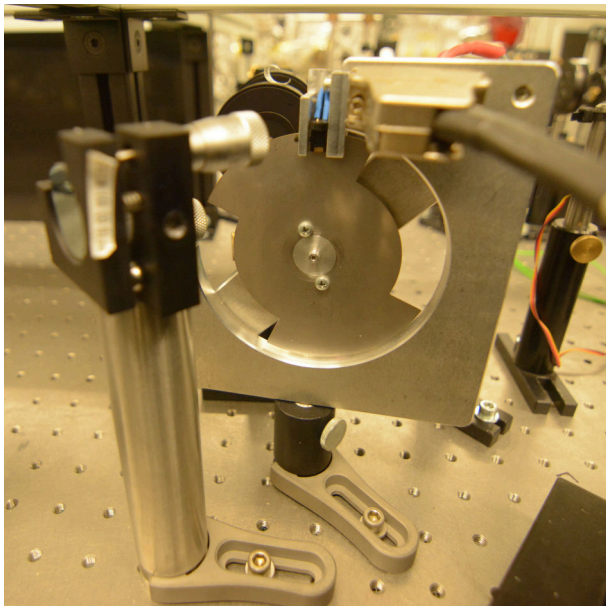
Figure 2.4: mechanical chopper with photodiode on top

To adjust the delay, the chopped SHG signal is measured by the photodiode, compared to the delayed chopper-photodiode signal and the phase delay is adjusted. Since the delay line can only adjust the absolute delay, if the chopper speed is changed, the delay time also has to be adjusted. During all measurements no influence of the choppers brushed DC motor on the adjacent photoelectron/photoion time-of-flight setup has been detected. This might be due to its low frequency. The delay-line signal is fed into an Arduino, that acts as A/D converter to send the chopper state to the PC via USB. The open/closed time of the chopper windows is set to 80 ms. Since spectra acquired when the pulse is partly blocked by the chopper have to be omitted and the laser power drifts in time (see figure 3.18 on page 55), this value is a trade-off between noise and measurement time, a more detailed discussion about the noise level can be found in section 3.3.2 on page 53. In figure 2.4 the setup of the chopper on the optical table is presented, a picture of the chopper control and delay line can be found in figure A.3 on page 68.
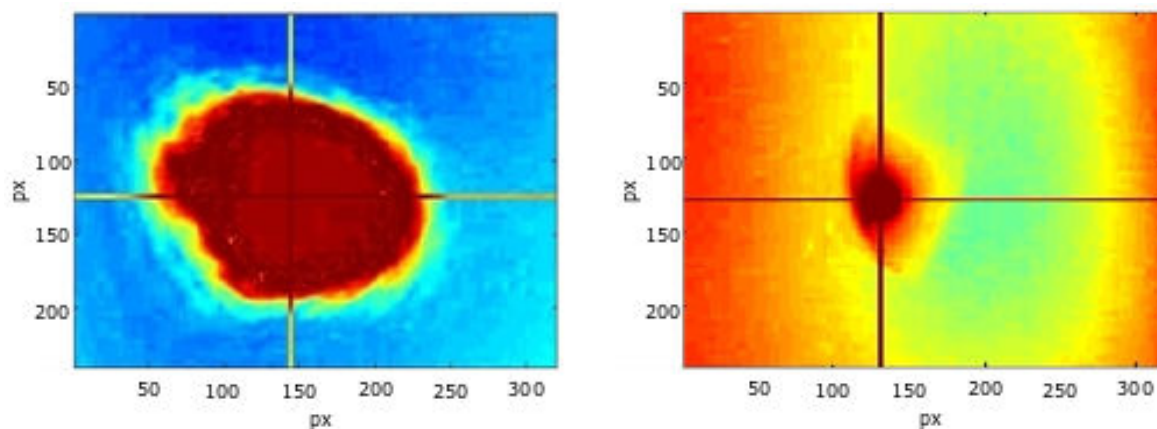
2.3 Transient Absorption in Solution

2.3.1 Setup of Flow Pump and Cuvette

Table 2.3: Parts for solution measurement.

Label	Company	Part-No.
Flow cell	Hellma Analytics	137-1-40
Dye pump		
Pump controller	Lambda Physik	FL 300 2
Power Supply	MW	MW2P300

To avoid thermal damage to the sample or pumping it into a triplet or isomerised state, the pump volume has to be constantly replaced by, either a flow pump or translation of the sample. Since motion at the repetition rate of the laser is difficult to realise, a dye pump is used with a reservoir volume of 80 mL. Regarding the cuvette, essentially a high flow and thin windows (to reduce chirp and nonlinear effects) are favorable. A cost efficient cuvette with a window thickness of 1.25 mm, 1 mm optical path length is used. Further a cell volume of 260 µl assures, that if expensive samples are of interest, a big and thus expensive reservoir can be avoided (here a sample-translation is inevitable). The dye laser pump is carefully cleaned and then rinsed with ethanol for several hours to get rid of residual dye. The flow cuvette is connected to the pump using flexible PVC tubes and PTFE seal tape. Due to their chemical stability PTFE tubes were first used, but their stiffness lead to leaks and fissures of the cuvettes glass connectors. The dye pump can be driven at two different gears and a rough estimate for the flow is $\sim 10 \frac{\text{mL}}{\text{s}}$ in the high gear.

2.3.2 Finding Overlap

As beam profiler the CCD chip of a webcam is used. This chip is placed in the focal plane of pump and probe. The foci are aligned and it is ensured, that the pump focus is bigger than that of the probe, as can be seen in figure 2.5. This ensures that the area of interest is homogeneously pumped. Now the cuvette/sample is mounted onto a stage and moved into focus, a transient absorption spectrum is acquired and the position iteratively adjusted, to get the maximum signal. Two important questions arose now. First, does convection of the solvent take place on a measureable level that a flow pump is unneccessary? Therefore a measurement at the spatial overlap is compared with a slightly misaligned one. The flow pump is switched off in both cases. The result is presented in figure 2.7, the second harmonic pump at ~ 400 nm depopulates the ground state of the aminoazobenzene solution at around 400 nm. If the overlap is poorly positioned, no effect of the pump is apparent. This is clear evidence, that no convection effects take place on a measureable level. Second, does the flow pump deliver fresh samples fast enough, that no molecule experiences multiple laser pulses? Therefore a transient absorption mesaurement with

(a) SHG, FWHM $= 125\,\text{px} \times 174\,\text{px}$.

(b) White light, FWHM $= 129\,\text{px} \times 81\,\text{px}$.

Figure 2.5: Pulses on CCD beam profiler, $1\,\text{px} \approx 5.5\,\mu\text{m}$.

the flow pump switched on is compared with a transient absorption measurement with the static liquid (see figure 2.6). Here the absorption of aminoazobenzene in solution has changed due to the presence of the pump at $\sim$400 nm. Less absorption from a state around 400 nm indicates that population has been excited to higher states. Additional to this bleached state, also more absorption takes place at other wavelengths. This is explicit prove, that an interaction with the pump has taken place. A detailed treatment of the investigated molecule aminoazobenzene can be found in chapter 3. Since the signal difference is not dependent on the stage position the stage is well aligned. By using this measurement technique a misalignment of the stage position can easily be identified.

Once the spatial overlap and the delay-stage are aligned, the flow pump is switched on and a low time resolution timescan started as can be seen in figure 2.8. Since the pump beam ($\lambda \sim 400\,\text{nm}$) is scattered at the sample/cuvette, there is always stray light detected in the spectrometer. This might conceal underlying transient signal and is therefore cut out. A simple yet effective way to reduce pump stray is to put a polariser in front of the spectrometer and change the pump polarisation 90° to the probe. It is only fair to mention, that this violates the magic angle setup, as is discussed in section 1.4. In figure 2.8 around 400 nm negative signal indicates bleaching of the ground state after overlap and at around 450 nm a narrow line points out a so called stimulated Raman amplification. Both effects will be thoroughly discussed in section 3.2 on page 42.
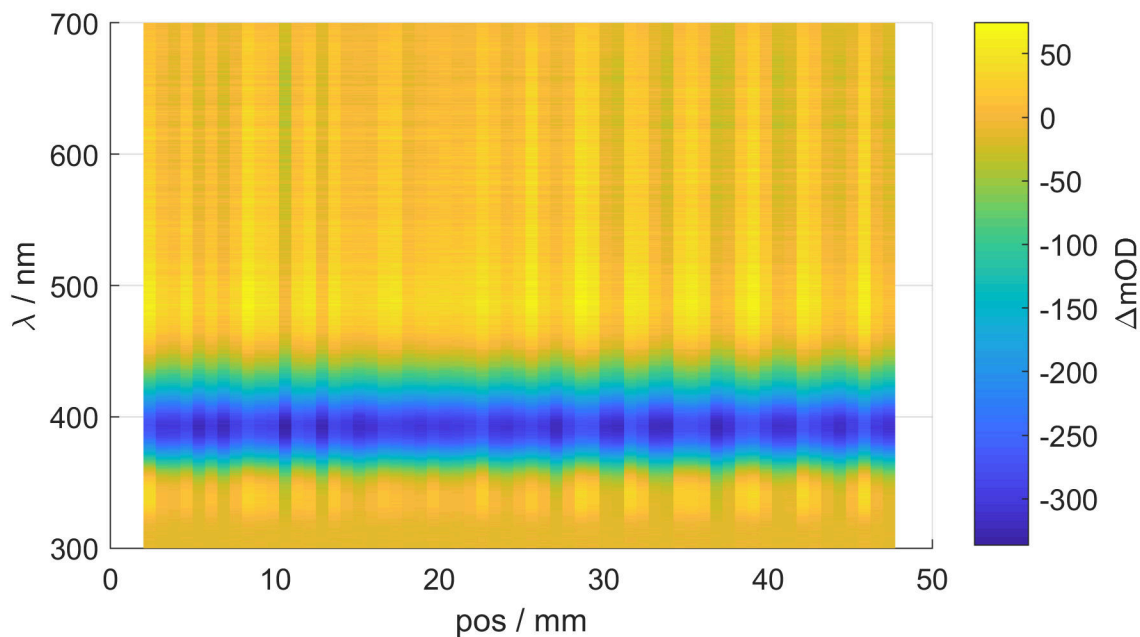
Figure 2.6: Stage scan flow dependency of aminoazobenzene solution absorption. ΔOD of unflowed solution compared to flowed solution signal. SHG pump energy 3.5 μJ, ∼990 nJ white light seed.
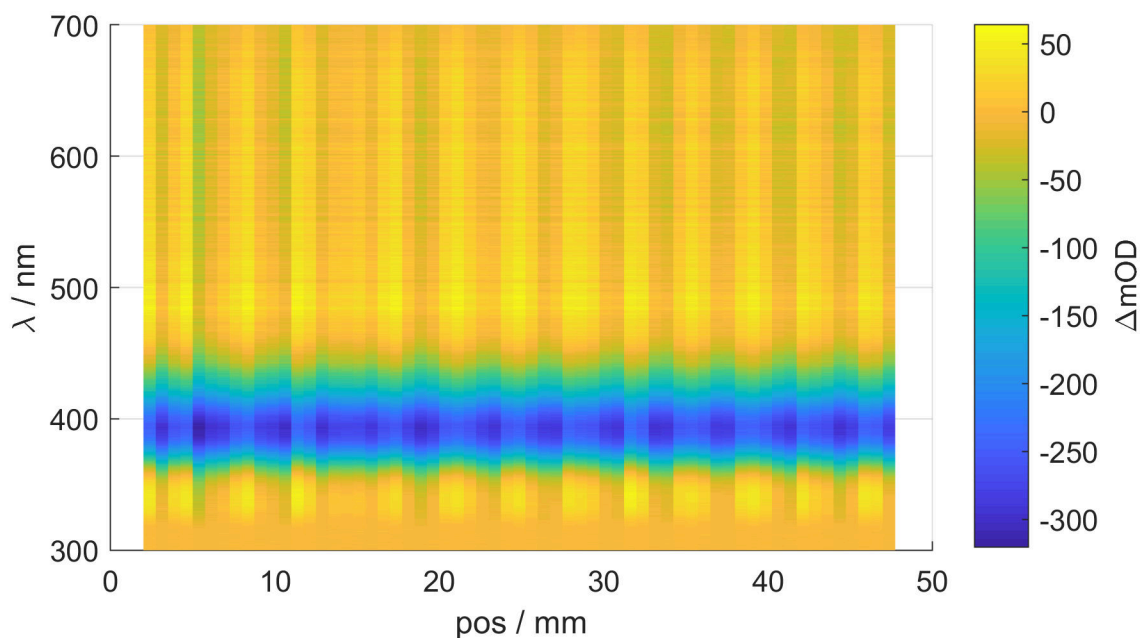flow data: TA_Timescan0041, unflowed signal: TA_Timescan0042

Figure 2.7: Stage scan spatial overlap dependency of aminoazobenzene solution absorption. Δ OD of overlap signal compared to slightly misaligned overlap signal. SHG pump energy 3.5 μJ, ∼990 nJ white light seed.
overlap data: TA_Timescan0042, misaligned data: TA_Timescan0043
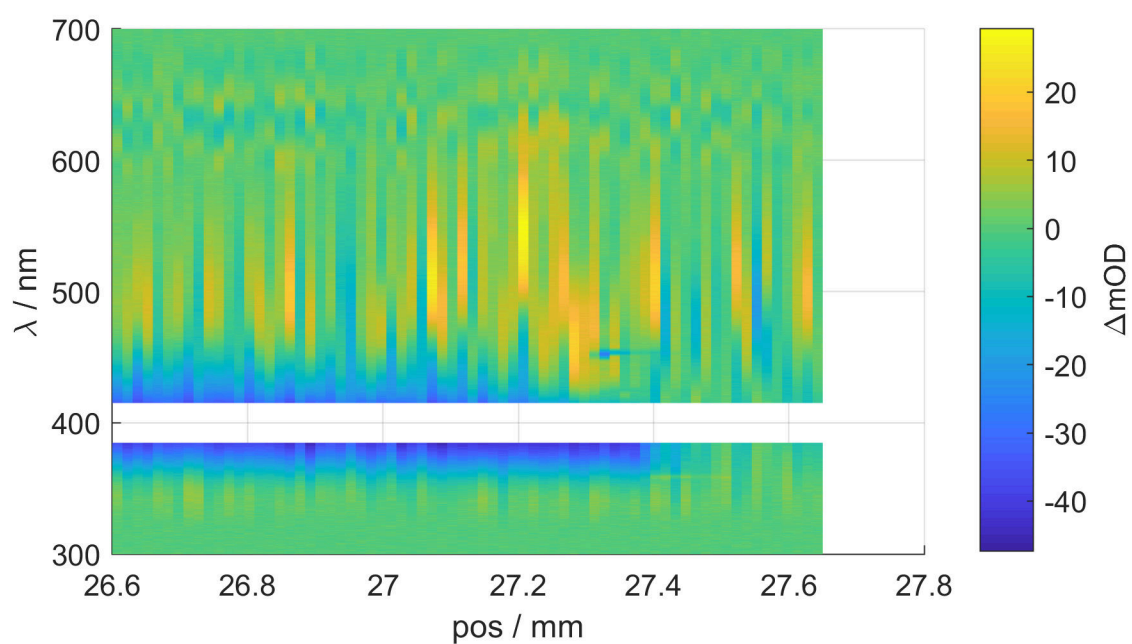
Figure 2.8: Low time resolution transient absorption scan of aminoazobenzene solution. ∼900 nJ white light seed, 6.4 µJ SH pump. Step size of 0.1 mm, accumulation time per stage position ∼ 10 s
data: TA_Timescan0062

2.4 Measurements on Thin Films

Experimentally, measurements of solutions differ from thin films regarding two properties. First the optical density can be arbitrarily chosen in solution, but is constant for thin films. This is unfortunate but inevitable. Second, in soulution a vast reservoir ensures, that no molecule is excited multiple times. Thin films lack this feature and one has to find a way to avoid multiexcitation, that would lead to a ground state bleach or even worse, thermal damage or degradation of the sample.
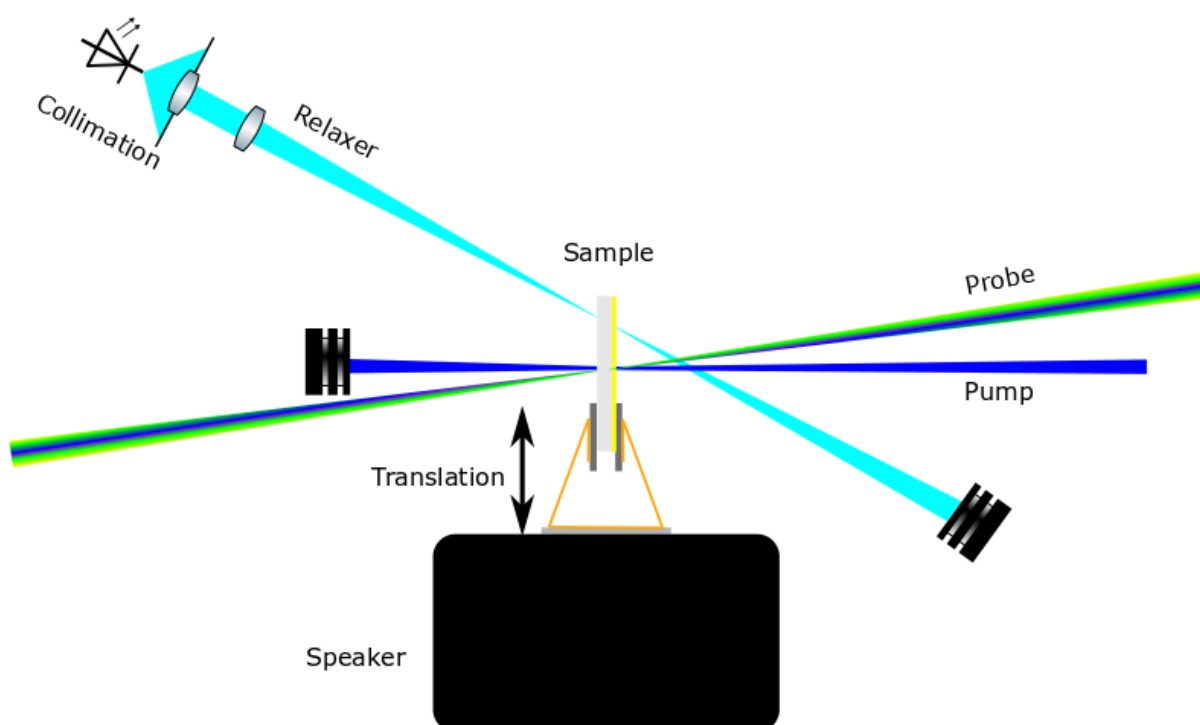
Figure 2.9: Pump-Probe setup with LED and translation of sample.

In order to prevent a bleaching or thermal damage of the sample, the sample is constantly moved. Rotation would request rotational frequencies of at least ~40 Hz to ensure, that consecutive pulses do not irradiate the same region of the sample. Since construction takes some time, for the first tests a speaker was dissembled and the sample holder (a clamp) glued to the coil. To prevent the sample from getting out of place, two viton pads are placed at the sites. The speaker is operated at 50 Hz and vibrationally decoupled from the optical table using foamed plastic. Since it is possible to bring certain molecules, back into the trans ground state, by illumination with a distinctive wavelength, a light emitting diode (LED) is installed to "refresh" the sample (see figure 2.9). This effect has already been successfully used for the used aminoazobenzene thin films in static absorption measurements [23]. Cis aminoazobenzene relaxes back into its trans ground state afer ($n\pi^*$) excitation (~500 nm) to the cis S_1 state. A thorough treatment of the molecule is carried out in chapter 3 on page 37. The setup is realised by placing a convex

lens with a very short focal length in front of the LED to collimate the light. In the next step another convex lens focuses the ray on an unpumped part of the sample. Two things have to be mentioned here: As indicated in figure 2.9 most high power LEDs have a wide angle of radiation, thus even a collimation lens featuring a short focal length will gather only part of the light. Second, since one can only get an image of the source and an LED is not a point source, the image on the sample will be bigger than necessary. Due to these two criteria a small but efficient LED with a small angle of radiation might perform better, than a wide angle of radiation LED with a big source area.
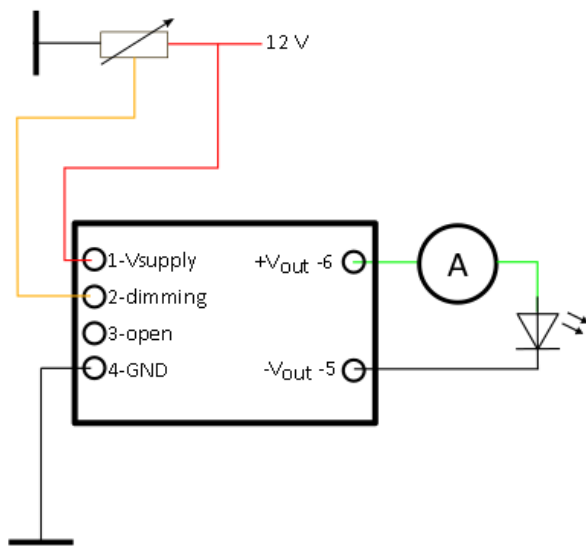
Figure 2.10: Schematic of the LED driver (RCD-24) circuit.

Therefore different LEDs have been acquired and operated using an LED-driver (RCD-24) circuit (see figure 2.10). An LED driver basically controls the LED current by setting a reference voltage. Using a bleeder and changing the resistivity of the potentiometer this voltage and therefore the LED current can be freely adjusted, in our case up to $700\,\mathrm{mA}$. An amperemeter measures the LED current to assure reproducibility and prevent damage. Further one has to be aware, that especially all dimming pins must not get disconnected, because zero voltage at pin 2 of the LED driver leads to maximum LED current and might be over the damage threshold of the LED.

Table 2.4: Different LEDs acquired.

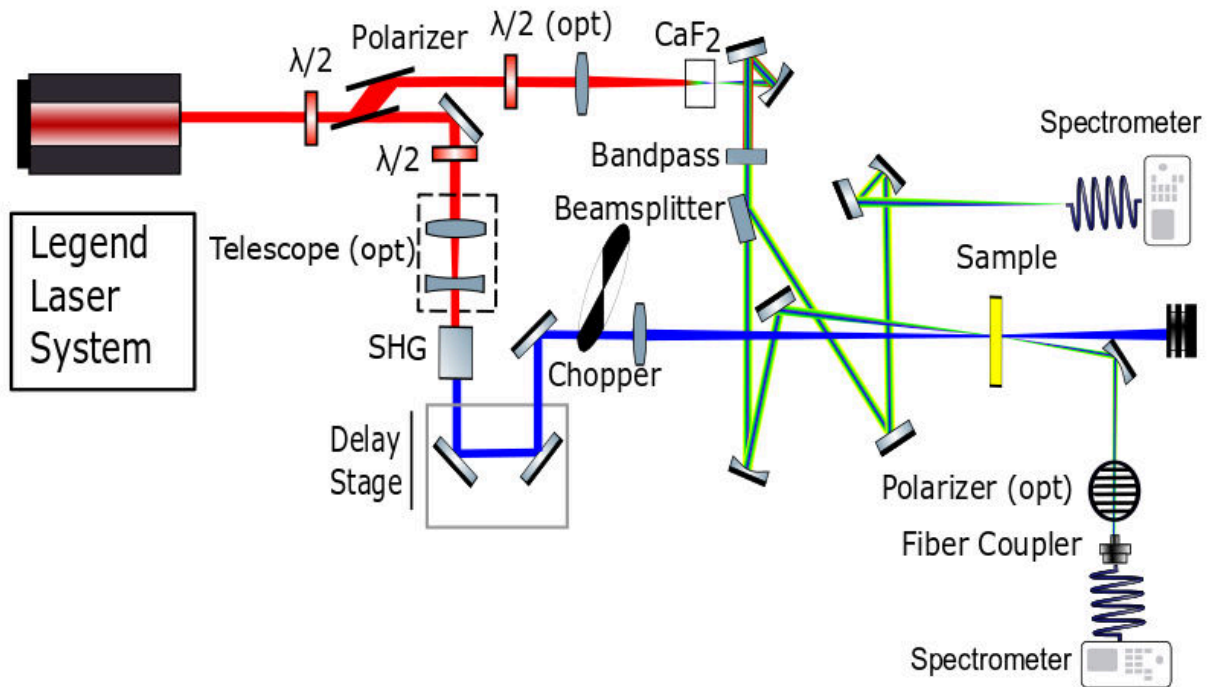| Label	Wavelength / nm	Maximum current / mA	Angle of radiation / °	Company	Part-No.
CREE	520	20	15	CREE	T-1 3/4 THT 4 V
Broadcom	505	30	30	Broadcom	HLMP-CE34-Y1CDD
Lumileds	490-510	1050	170	Lumileds	L1C1-CYN1000000000
ProLight Opto	515	700	130	ProLight Opto	PM2B-3LCE-SD
Thorlabs	505	1000	80	Thorlabs	M505D2

2.5 Reference Beam Setup

Figure 2.11: Pump-Probe setup with reference beam

In order to suppress white light fluctuations due to the sample motion, or a spectrometer/laser drift, a reference beam path is introduced. Therefore a fused silica microscope slide is placed behind the bandpass (see figure 2.11). Since chirp effects are negligible for first tests, the reflected beam is used as reference and the transmitted as probe beam. The reference beam is focused into a fiber and detected using another spectrometer (Ocean Optics USB4000). Unfortunately, the pulse fluctuations of reference and probe beam do not match. This is mainly due to the fact, that only part of the light that is focused into the fiber is coupled in. Since this part is highly angle and position dependent, different parts of the original beam are coupled into the two spectrometer. In figure 2.12 this uncorrelated signal change over time is clearly visible. Therefore the reference beam is not used for the presented experiments but might be valuable for the future, in particular with the following improvements. To ensure equal spatial distribution of probe and reference beam on the detector a possible next step could be to put a cosine corrector (or simply a thin PTFE-tape) in front of the fiber to get equally random distributed light in both fibers. Another more promising, but cost intensive enhancement is to focus reference and probe vertically separated on the same entrance slit of a spectrometer and align the beams on one CCD vertically separated.
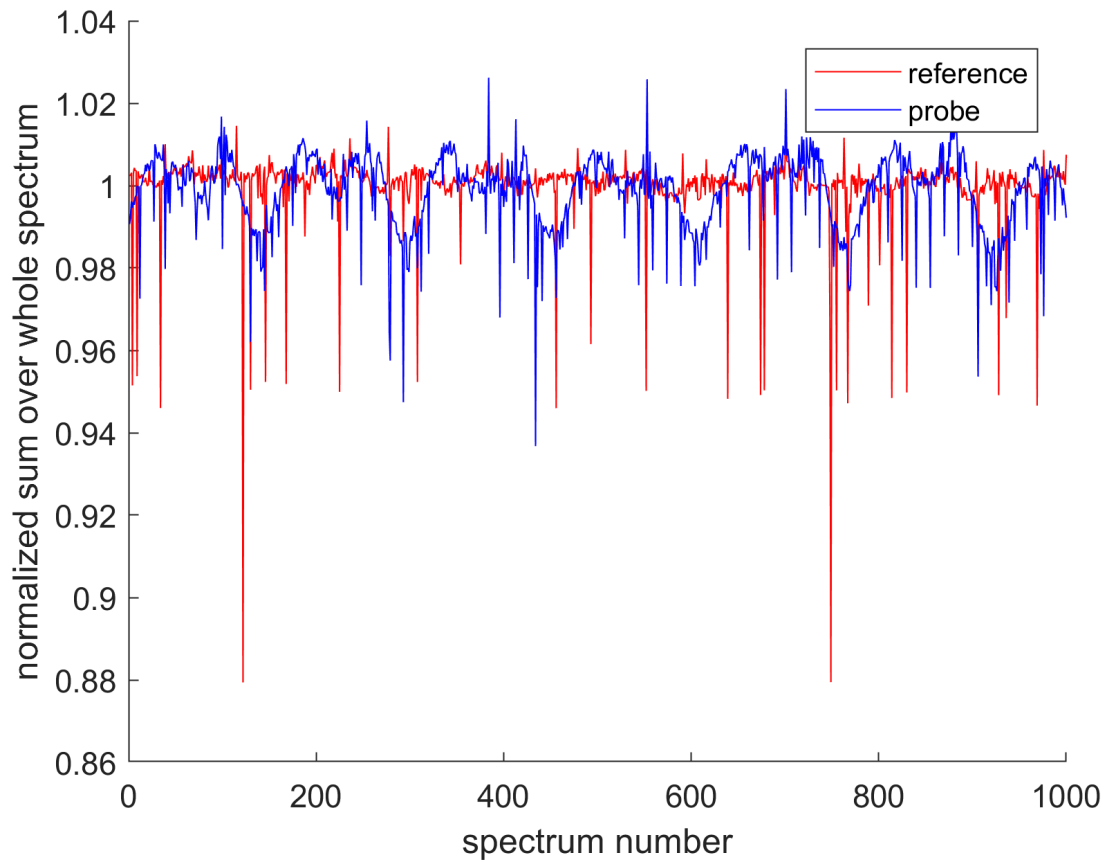
Figure 2.12: Normalized sum of probe and reference beam over all wavelengths.

2.6 Acquisition and Processing Software

The spectrometer comes with a cross-platform driver, the OmniDriver [24]. Using a wrapper, routines can be executed by a variety of programming languages including C/C++, Java and Matlab. Since the maximum trigger frequency of the spectrometer is 344 Hz a high level software acquisition getting the chopper state of the Arduino in real time is sufficient. For faster acquisition times a low level solution using a hardware trigger is favourable. To put it in a nutshell, a matlab script executes a java function, that waits for the chopper trigger and then acquires a certain amount of spectra. The spectra and chopper state are then used to calculate transient absorption in matlab. For the presented results, 20 spectra are acquired within a chopper on/off window. 10000 spectra are acquired per stage position.

2.6.1 Transient Absorption Timescan

This file executes a standard transient absorption timescan and is the last in a series of scripts and benefits from the work of Pascal Heim and Bernhard Thaler. Here a compact overview of: timescan_TA_java_real_Time_with_arduino___speaker_shutter_set_in.m

- **the shutter to generate white light is opened**

- **frequency and amplitude of the speaker are set**

- **save path and filename are defined**

- **wavelength data of the spectrometer are read out**

- **the stage is initialised**

- **the java class is opened**

- **the timescan is started for all stage positions**
    - **the spekaer starts to move**
    - **the stage moves to the desired position**
    - **spectra are acquired using the java function**
    - **the speaker stops moving**
    - **jittered spectra are removed**
    - **spectra are assigned to their chopper state**
    - **calculation of local transients**
    - **final transients are calculated**
    - **the transient data is saved**
    - **if the white light is unstable, the shutter is closed**

2.6.2 Synchronous Acquisition

The script synchron_acquisition_func.m measures the probe light and its reference. Therefore two spectrometer (Ocean Optics Flame-S and Ocean Optics USB4000) are used, that are read out in real time using threads in java. Again this script highly profits from files already written by Bernhard Thaler. A brief overview of synchron_acquisition_func.m:

- **the java class is opened and the function executed**

- **both spectrometer are initialised and the integration time set**

- **the chopper triggers two threads that acquire spectra with the respective spectrometer**

- **the signals are binned, that both spectra possess the same wavelength vector**

- **the data is evaluated and saved**

CHAPTER 3

Results on Aminoazobenzene

The different properties of azobenzene and its derivates presented in this chapter have been investigated before and an excellent overview can be found in reference [16]. A more application-oriented insight can be gained in reference [25].

4-aminoazobenzene is an organic molecule ($C_{12}H_{11}N_3$), that is widely used as dye. Another prominent feature lies in the azobenzene part of the molecule. Azobenzene and its derivates are promising photoactive "switches", that once electronically excited from the trans-ground state, may choose to relax into its cis-isomer (see figure 3.1).
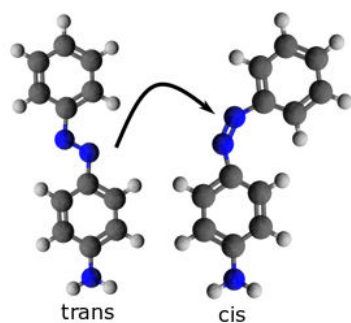
Figure 3.1: Isomerisation

The reorientation along the N=N bond is still topic of present research [26, 27, 28, 29] and a phenomenon, that needs ultra-fast spectroscopy to give insight into its underlying mechanisms. Different paths of relaxation, presented in figure 3.2 have been proposed and will be discussed briefly. Since the lowest excitation nπ* (S_1) of trans-aminoazobenzene is dipole forbidden, it is excited to the next higher $\pi\pi$* (S_2) state, witch lies about $3.2\,eV$ above the ground state and is therefore accessible using a $400\,nm$ light beam. Once in the $\pi\pi$* state the molecule will undergo internal conversion (IC) into the nπ* (S_1) state and finally into the trans or cis ground state (S_0). Following Kasha's rule one would expect, that the molecule relaxes back into the lowest vibrational S_1 state and then further down, blue path in figure 3.2 ("cold channel"). Azobenzene and its derivates exhibit a different behaviour, since at high vibrational S_1 states a conical intersection (CI) to high S_0 states forms a so called "hot channel" into the trans state, thus reducing the quantum yield for cis isomerisation [27]. If by chance the molecule isomerises into the cis state, a new absorption band at $\approx$(470 to 530) nm appears, the cis S_1 transition. This excitation exhibits a high quantum yield for relaxation back into the trans state and may be driven using
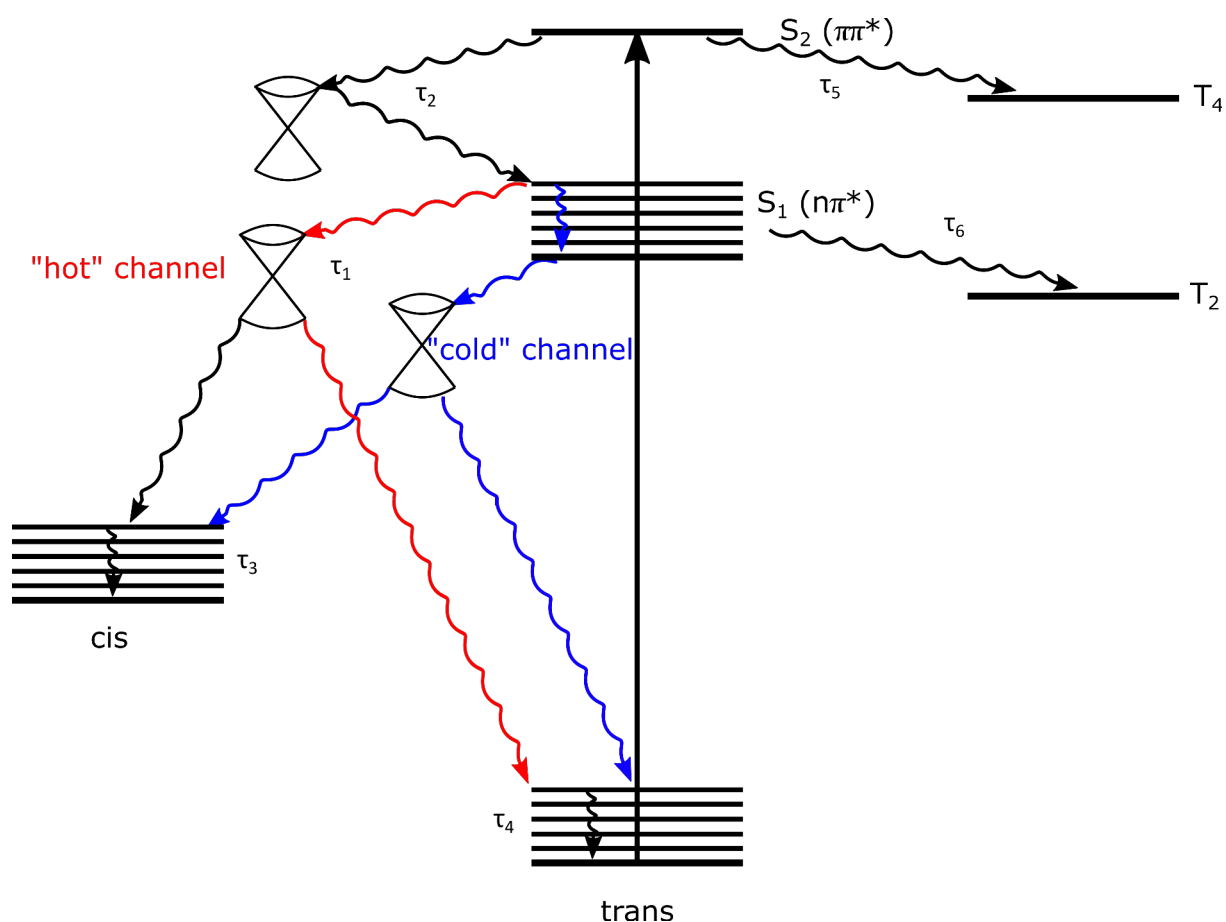
Figure 3.2: Different relaxation paths of aminoazobenzene, "hot" channel in red (violating Kasha's rule), generally expected relaxation path ("cold" channel) in blue. Adaptation of propositions made by reference [27, 12].

the LED relaxer introduced in section 2.4. In figure 3.3b the initial absorption spectrum and the change of absorption after isomerisation is shown. This allows comparison with following results in section 3.2. Further transitions from S_2 and S_1 into triplet states have been proposed [12]. The main goal for this setup will be to compare relaxation paths that an excited molecule in solution takes compared with the ones rooted on a thin film. In figure 3.4 an overview of all proposed isomerisation paths is displayed, the pathway highly depends on the excited state and should change drastically if certain degrees of freedom are restricted [16].

(a) Normalised trans absorption.

(b) Change of absorption after isomerisation into the cis state.
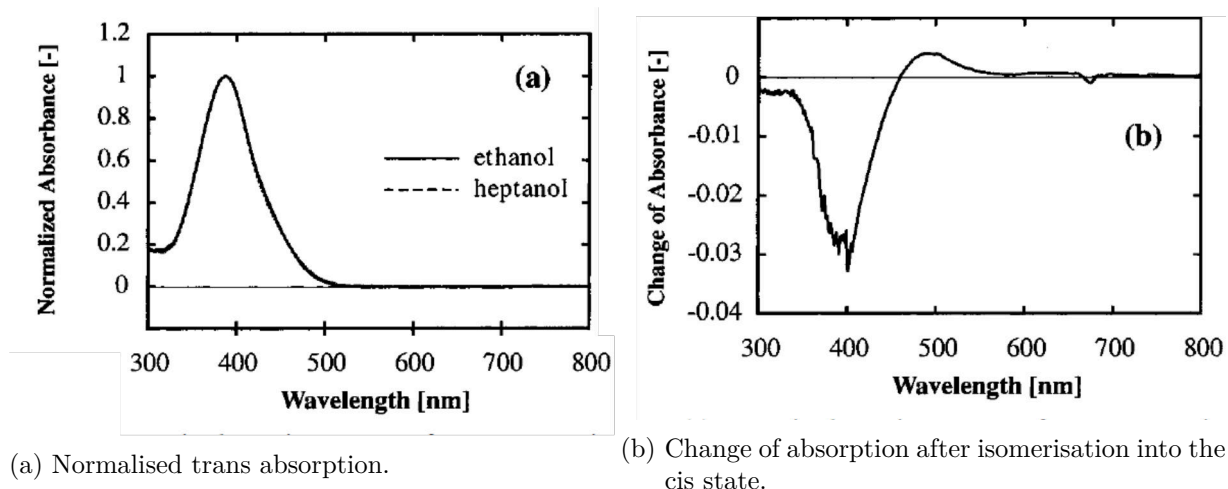
Figure 3.3: Expected absorption spectra of aminoazobenzene in solution. Adapted from reference [30].
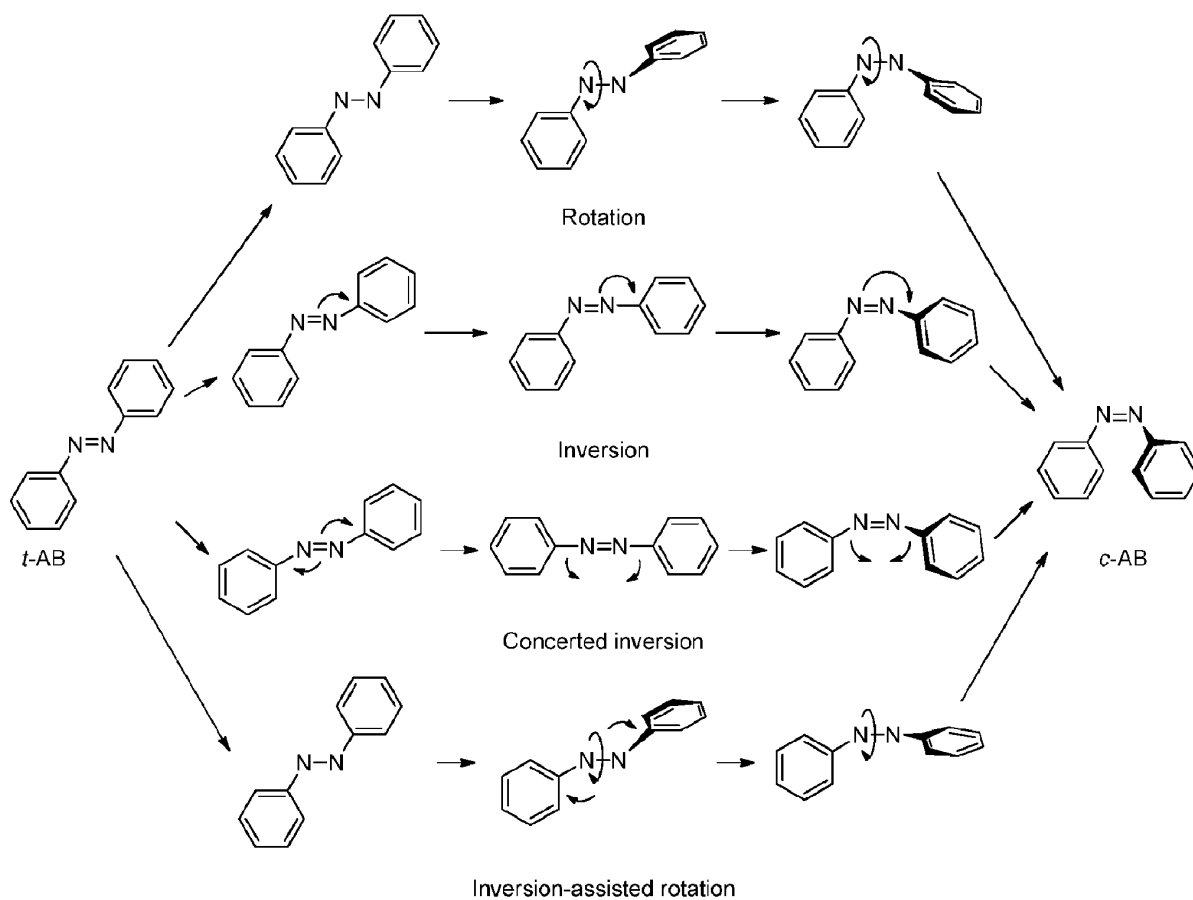
Figure 3.4: Proposed isomerisation pathways of azobenzene [16].

3.1 Quantum Chemical Simulations

Using the Gaussian09 program package [31] geometry optimization and time dependent density functional theory (TD-DFT) calculations for trans/cis aminoazobenzene are performed. The basis set 6-311++G(d,p) and hybrid functional B3LYP are used. For trans aminoazobenzene, the excitation wavelength of transition to trans S_2 and S_1 are in the range of the experimental values (see table 3.1). In figure 3.5 the participating orbitals of trans aminoazobenzene are displayed. Excitation wavelengths of cis aminoazobenzene are in agreement with experimental values, but multiple orbitals are supposed to participate in the excitation, therefore no molecular orbitals are displayed. In table 3.1 the calculated values can be found. Looking at figure 3.5a we see the nonbinding character of the second highest occupied molecular orbital (HOMO-1). Further it is interesting, that the energetically lowest transition is not from the highest occupied molecular orbital (HOMO) to the lowest unoccupied molecular orbital (LUMO) but from HOMO-1 to LUMO. In figure 3.5b the bonding character (π^*) of the HOMO orbital at the N double bound is apparent. Finally in figure 3.5c the anti bonding contribution of the LUMO orbital at the N double bond is clearly visible. In conclusion these simulations are helpful to get an idea of possible properties of aminoazobenzene but do not provide any exact information. To get further insight an extended quantum chemical treatment has to be performed, which is not within the scope of this thesis.

Table 3.1: Calculated transition values of aminoazobenzene [31]
S_x ... Singulet transition to state No. x
T_x ... Triplet transition to state No. x
λ / nm ... Excitation wavelength
f ... Oscillator strength of transition

	trans aminoazobenzene		cis aminoazobenzene	
state	λ_{exc} / nm	f	λ_{exc} / nm	f
S_1	472.07	0.0000	488.87	0.0586
S_2	372.74	0.8498	330.82	0.2267
S_3	299.17	0.0077	308.40	0.0192
T_1	654.64	0.0000	784.36	0.0000
T_2	618.87	0.0000	455.87	0.0000
T_3	373.74	0.0000	370.36	0.0000
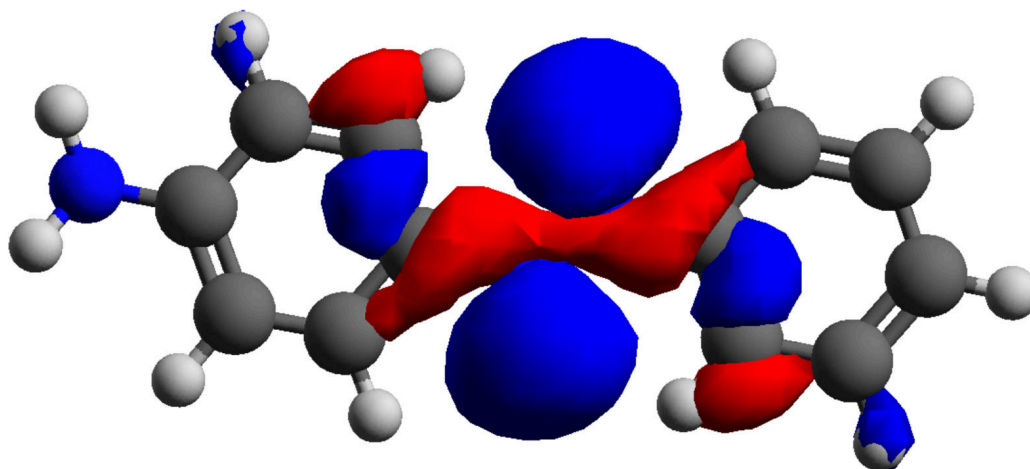
(a) Second highest occupied molecular orbital (HOMO-1). Initial orbital of the transition to S_1.
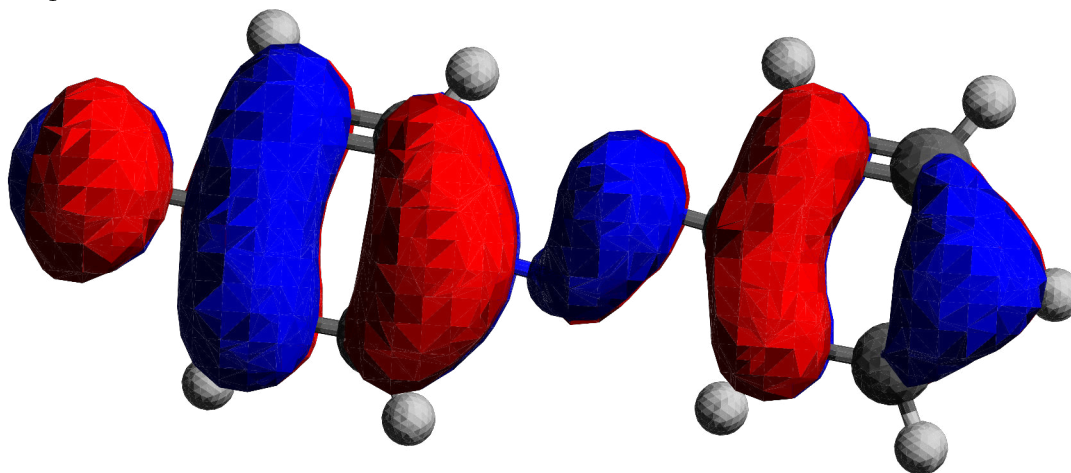
(b) Highest occupied molecular orbital (HOMO). Initial orbital of the transition to S_2.
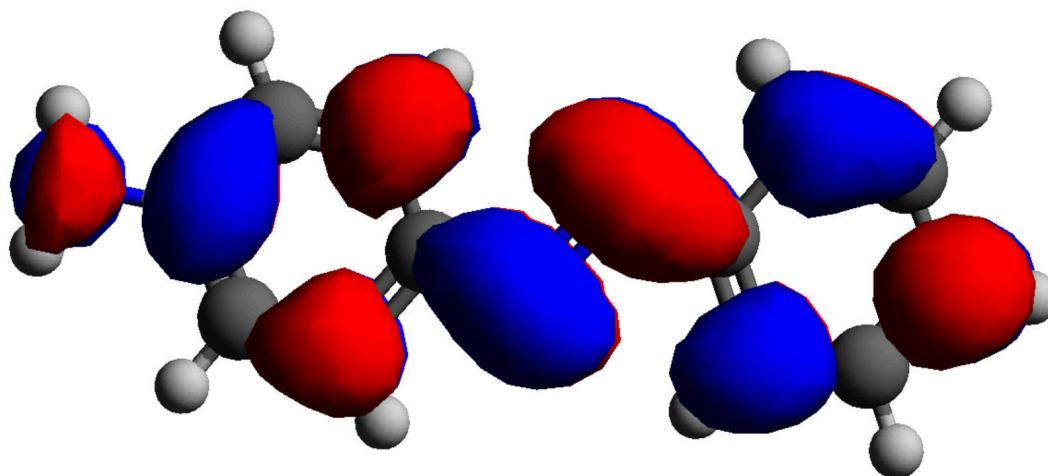
(c) Lowest unoccupied molecular orbital (LUMO). Final orbital of the transition to S_1 and S_2.

Figure 3.5: Different orbitals of trans aminoazobenzene calculated with Gaussian09. Basis set 6-311++G(d,p) and hybrid functional B3LYP [31].
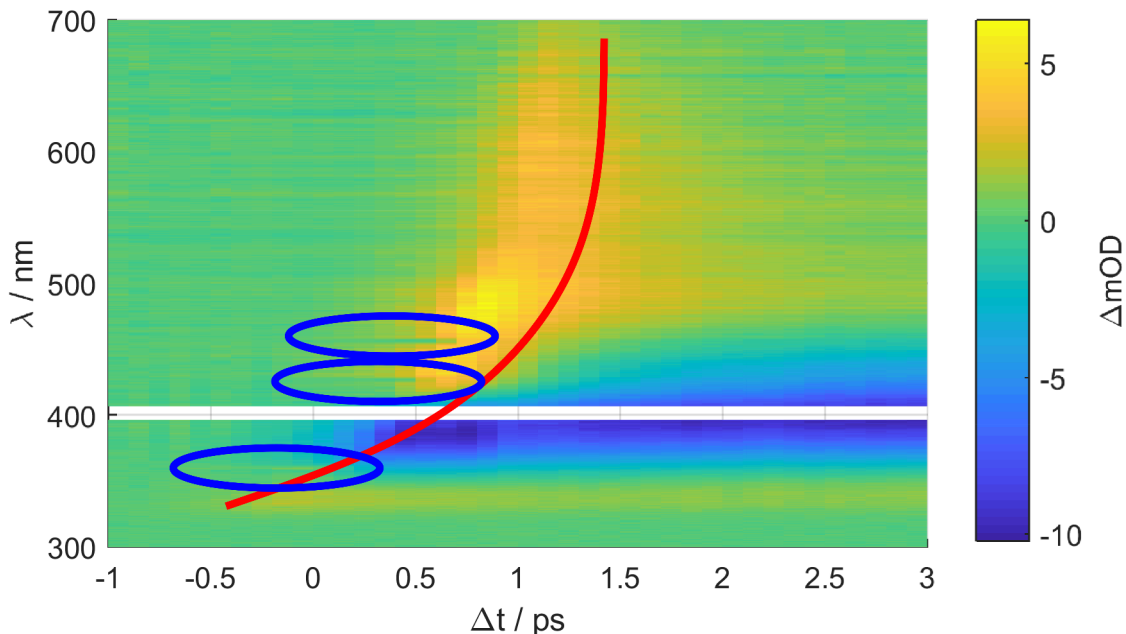
3.2 Transient Absorption in Solution

Figure 3.6: Artifacts of transient absorption probe-chirp dependency in red and Stimulated Raman amplification in blue. Signal before overlap subtracted. Cross phase modulation and two photon absorption cannot be disentangled from other artifacts without reference measurement. $\lambda_{pump} = 402\,nm$, $FHWM_{pump} = 2\,nm$, $E_{pump} = 10\,\mu J$, $700\,nJ$ white light seed
data: TA_Timescan_java0114.

As solvent ethanol is chosen, due to its negligible wavelength-shift of the absorption maximum [32]. Further at least for azobenzene, ethanol gives the second highest probability of trans to cis isomerisation [16]. The transient absorption timescan has been prepared and measured as discussed in section 2.3 and is shown in figure 3.7. The stray pump is cut out and the data subtracted by the pre overlap signal. At the overlap, see figure 3.6, the discussed artifacts can be observed. Two Stokes-shifted stimulated Raman amlification (SRA) peaks can be observed. One of them at $(456.5 \pm 0.4)\,nm$ beeing the CH-stretching of the solvent ethanol $E_{C\text{-}H} = 364\,meV$ [17]. $\lambda_{pump} = (402.3 \pm 0.4)\,nm$, E_{pump} - $E_{probe} = (365 \pm 6)\,meV$. The anti-Stokes shifted signal is centered at around $360\,nm$ and confirms the calculated vibrational energy. The other Stokes-shifted SRA line with an vibrational energy of $\sim 175\,meV$ at $\lambda_{probe} = (426.7 \pm 0.4)\,nm$ is one or a mix of multiple other vibrational modes, that lie in this energy range [33]. Due to the fact that the SHG-beam intensity is many times higher than the white light, signal of Stokes SRA is more pronounced than the anti-Stokes. The anti-Stokes signal at $\sim 380\,nm$ is hardly visible and therefore not marked in figure 3.6.

Up-chirp of the probe pulse is clearly visible, not only from the shift in overlap signal but also in the time difference between Stokes and anti-Stokes SRA signal (red line in figure 3.6). Two

photon absorption (TPA) cannot be disentangled from absorptions from S_2 and no effects of cross phase modulation (XPM) are observed, mostly due to a lack of pump intensity but also here absorption of the S_2 state that might hide the effect.
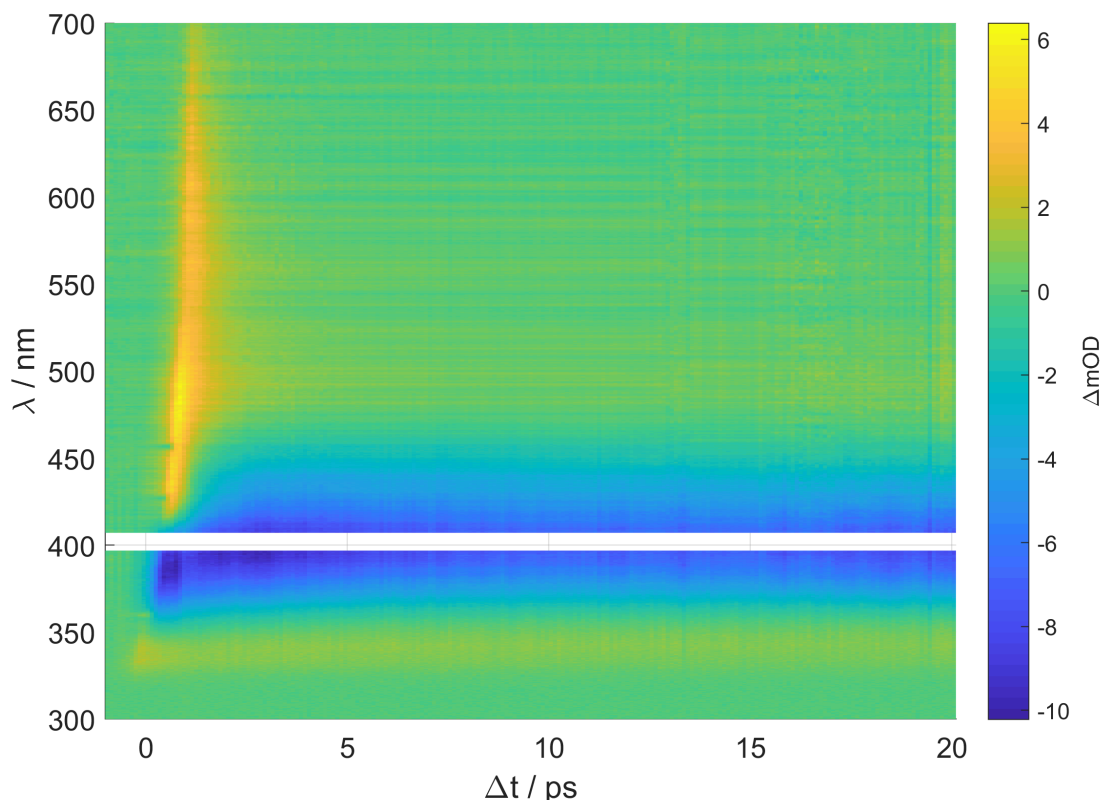

Figure 3.7: Transient Absorption spectrum of aminoazobenzene in ethanol solution. Signal before overlap subtracted. $\lambda_{\text{pump}} = 402\,\text{nm}$, $\text{FHWM}_{\text{pump}} = 2\,\text{nm}$, $\text{E}_{\text{pump}} = 10\,\mu\text{J}$, 700 nJ white light seed
data: TA_Timescan_java0114.

If we look at a slice of the transient absorption measurement (figure 3.7) at 10 ps, prestented in figure 3.8, dynamics have mostly ended and we can see the expected change of absorption due to isomerisation plotted in figure 3.3b. Looking at the suggested relaxation pathways from figure 3.7 we can or cannot distinguish the following time constants, as it is done in reference [12]. First after excitation, we encounter relaxation from S_2 to S_1 with τ_2 and an suggested intersystem crossing to the triplet state T_4 with τ_5. From the S_1 state the system relaxes with τ_1 either into to the trans or cis ground state following vibrational relaxation (cis τ_3, trans τ_4). Additionally an intersystem crossing from S_1 to the triplet state T_2 has been proposed (τ_6) [12]. To fit the signal decay a convolution of the instrument response function with a product of exponential decay and a step funtction is used, shown in equation 3.2. First a normalised approach as it is described by reference [34] was tried, but failed to correctly weigh the individual exponential decays. Therefore an extra fit parameter a to weigh the individual decays is introduced as it is
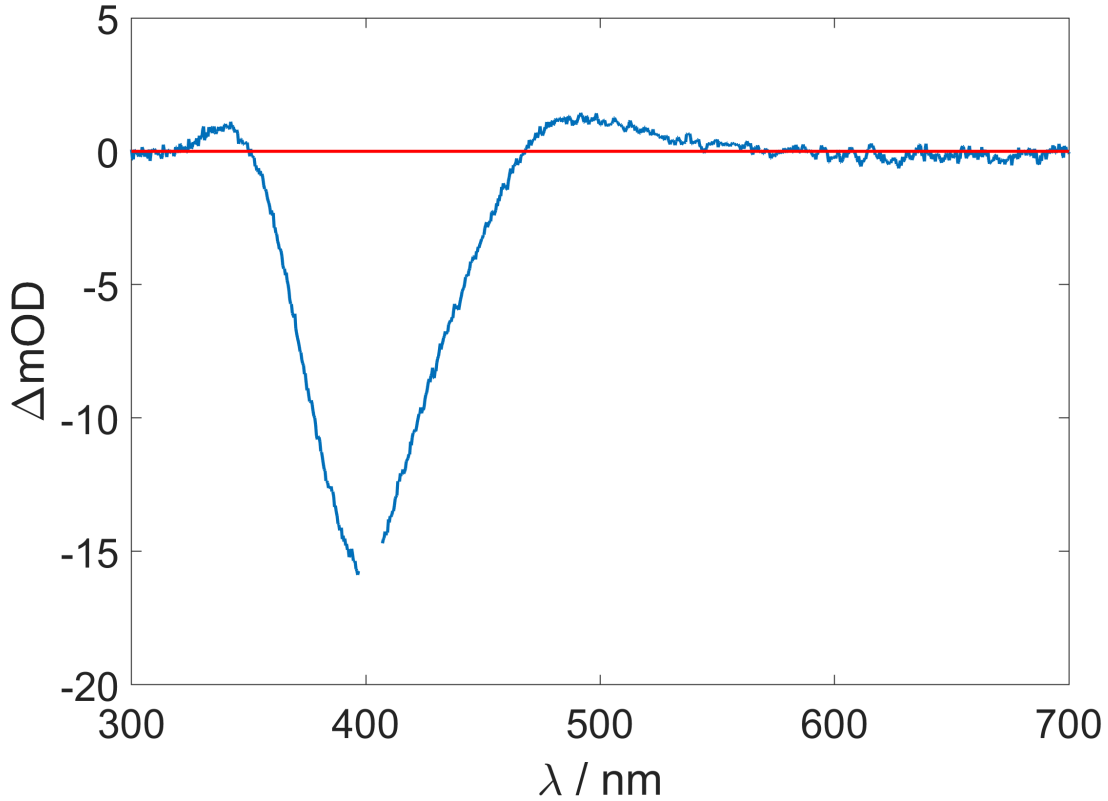
Figure 3.8: Transient absorption of aminoazobenzene in ethanol solution $\sim 10\,\mathrm{ps}$ after overlap. Signal before overlap subtracted. $\lambda_{\mathrm{pump}} = 402\,\mathrm{nm}$, $\mathrm{FHWM}_{\mathrm{pump}} = 2\,\mathrm{nm}$, $\mathrm{E}_{\mathrm{pump}} = 10\,\mathrm{\mu J}$, $700\,\mathrm{nJ}$ white light seed
data: TA_Timescan_java0114.

recommended by reference [2] and also used by reference [12]. The physical background to do so, lies in different absorption probabilities for a starting population that trickles down in the individual states.

$$N(t; t_0, \tau, \sigma, a) = a\, \exp(\frac{\sigma^2}{2\tau^2})\Big(2 - \operatorname{erfc}\Big(\frac{(t - t_0) - \frac{\sigma^2}{\tau}}{\sqrt{2}\sigma}\Big)\Big) exp(\frac{-(t - t_0)}{\tau}). \tag{3.1}$$

$$N = \sum_{i=1}^{k} N(t; t_0, \tau_i, \sigma, a_i). \tag{3.2}$$

With t_0, the time of overlap, τ the decay time, σ the standard deviation of the Gauss laser pulse.

In figure 3.7 we can distinguish five regions.

(620-680) nm Starting from the long wavelength limit of the spectrum at $(600$ to $700)\,\mathrm{nm}$ signal arises due to absorption from S_2 and S_1 to higher states with decay times of τ_2 and τ_1, respectively. Unlike reference [12] no inter-system crossing to a triplet state (τ_5) is detected, see

figure 3.2 for sketch. Fit parameters can be found in table 3.2 and a representative fit including a sketch of relaxation paths can be found in figure 3.9. Values found in reference [12] are presented in table 3.3 and are in agreement for S_1 and S_2 decay times. The neccessity of τ_5 is disputable. A probe chirp dependency of the overlap time t_0 is correctly stated by the fit.

Table 3.2: Fit of aminoazobenzene dynamics in ethanol solution at (620 to 680) nm
    λ / nm ... Wavelength range $\Delta\lambda = 1$ nm
    σ / fs ... Standard deviation of the Gauss pulse that fills the state
    t_0 / fs ... Time zero, fit
    S_1 ... First excited state that is indirectly filled ($n\pi^*$)
    S_2 ... Second excited state, that is directly filled ($\pi\pi^*$)
    τ_x / fs ... Decay time constant of S_x
    a_x ... Preexponential factor, to weigh the decays
    Δx ... Standard deviation of the respective fit value

					S_1				S_2			
λ/ nm	σ/ fs	$\Delta\sigma$/ fs	t_0/ fs	Δt_0/ fs	τ_1/ fs	$\Delta\tau_1$/ fs	a_1	Δa_1	τ_2/ fs	$\Delta\tau_2$/ fs	a_2	Δa_2
670-680	317	4	1210	40	1300	300	0.4	0.1	50	1	9.0	0.8
660	157	6	1120	20	1100	100	0.74	0.08	27.7	0.8	8	1
640	228	9	1138	2	1400	100	0.55	0.05	38	1	9.9	0.6
620	229	5	1130	20	1300	100	0.67	0.07	39.5	0.3	9.1	0.7

Table 3.3: Literature values for dynamics at (620-680) nm from reference [12]
    labels as in table 3.2. a_5 and τ_5 indicate a possible transition to a triplet state.

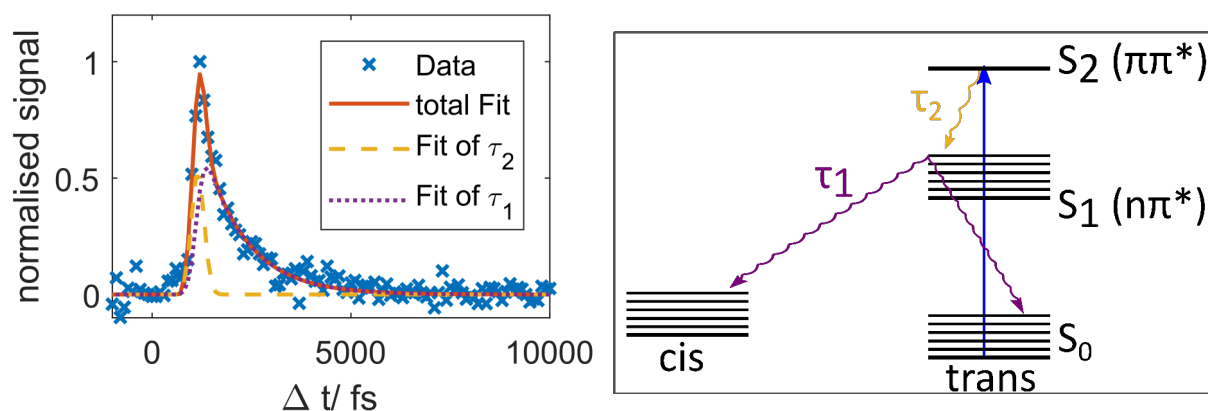| λ / nm	a_1	τ_1 / fs	a_2	τ_2 / fs	a_5	τ_5 / fs
680	0.19	800	0.75	66	0.06	442000
660	0.33	600	0.61	77	0.06	498000
620	0.57	600	0.37	61	0.06	442000

Figure 3.9: Fits of aminoazobenzene relaxation dynamics in ethanol solution at 660 nm. Sketch of the respective paths on the right.

(540-580) nm   Next at (540 to 580) nm again τ_1 relaxation is fitted and additionally a long time constant $\tau_?$. The only reasonable explanation is inter-system crossing to a triplet state (τ_6) indicated in figure 3.2. At (540 to 550) nm this time constant highly increases due to cis ground state absorption. In table 3.4 the fitted values can be observed and compared to literature values in table 3.5. A fit of the data and sketch of the respective relaxation paths can be found in figure 3.10. Averaging over a 10 nm range is neccessary to reduce noise in the fit and justified, since absorption bands are broad. The decay times of S_1 have decreased, this might be due to different vibrational states occupied in this wavelength range, further the time of overlap again shows the probe chirp. The huge discrepency of τ_6 with respect to reference values is hard to assign. Since the existence of this triplet transition is highly unlikely, the measurement was not conducted at the magic angle and there are quite a few fit parameters more measurements are neccessary to draw a conclusion.

Table 3.4: Fit of aminoazobenzene dynamics in ethanol solution at (540 to 580) nm
λ / nm . . . Wavelength range $\Delta\lambda = 1$ nm
σ / fs . . . Standard deviation of the Gauss pulse that fills the state
t_0 / fs . . . Time zero, fit
S_1 . . . First excited state that is indirectly filled (nπ*)
T_2 . . . Triplet state, that might be filled
τ_x / fs . . . Decay time constant of S_x/ T_x
a_x . . . Preexponential factor, to weigh the decays
Δx . . . Standard deviation of the respective fit value

					S_1				T_2			
λ/ nm	σ/ fs	$\Delta\sigma$/ fs	t_0/ fs	Δt_0/ fs	τ_1/ fs	$\Delta\tau_1$/ fs	a_1	Δa_1	τ_6/ fs	$\Delta\tau_6$/ fs	a_6	Δa_6
570-580	220	10	900	10	760	30	1.52	0.04	25000	8000	0.039	0.007
550-560	220	10	880	10	780	40	1.36	0.05	21000	2000	0.149	0.007
540-550	230	10	860	10	820	30	1.46	0.04	100000	30000	0.081	0.005

Table 3.5: Literature values for dynamics at (540-580) nm from reference [12]
labels as in table 3.4.

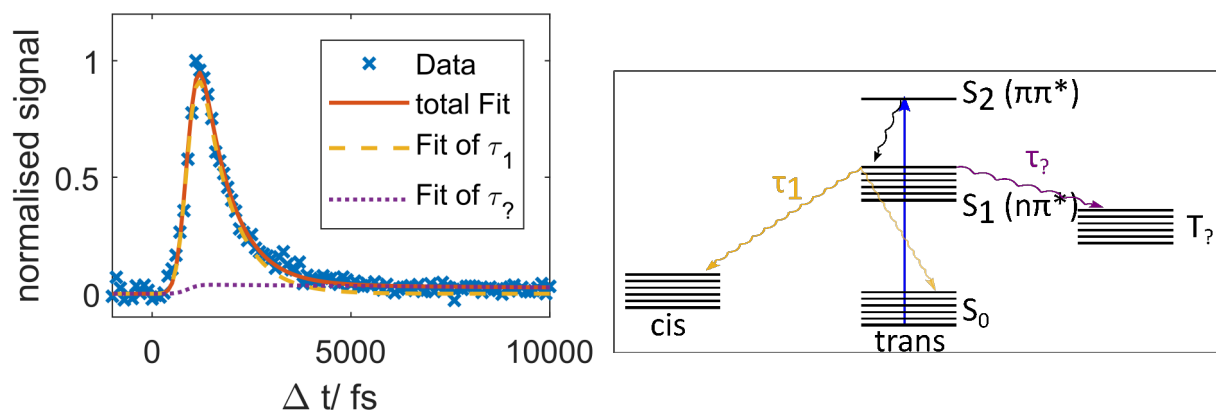| λ / nm	a_1	τ_1 / fs	a_6	τ_6 / fs
580	0.90	700	0.10	178000
560	0.92	700	0.08	174000
540	0.91	700	0.09	173000

Figure 3.10: Fits of aminoazobenzene relaxation dynamics in ethanol solution at (570-580) nm. Sketch of the respective paths on the right.

(480-530) nm (470 to 530) nm exhibits again τ_1 and additionally signal of the cis-isomer. Vibrational relaxation of the ground state (τ_3) and triplet transition might still occur (see figure 3.11), but cannot be explicitly distinguished. In table 3.6 the corresponding fit values are presented and can be compared to literature values in table 3.7. While reference [12] fits a vibrational relaxation dynamic of the cis ground state tau_3, this signal is not present or cannot be resolved in this measurement. Since the decay time of the cis state is within minutes, it is not explicitly mentioned in table 3.6 and table 3.7. Again an average over 10 nm improved the signal-to-noise ratio. Values of τ_1 differ with regards to literature values, this is mainly due to the difference of the fit model (3 vs. 2 decay times).

Table 3.6: Fit of the aminoazobenzene dynamics at (480 to 520) nm τ_{cis} is not displayed since decay time is in minutes to hours

λ / nm ... Wavelength range $\Delta\lambda = 1$ nm

σ / fs ... Standard deviation of the Gauss pulse that fills the state

t_0 / fs ... Time zero, fit

S_1 ... First excited state that is indirectly filled ($n\pi^*$)

cis formation ... Signal of the cis isomer, mixed with vibrational relaxation of the ground state

τ_x / fs ... Decay time constant of the respective state

a_x ... Preexponential factor, to weigh the decays

Δx ... Standard deviation of the respective fit value

λ/ nm	σ/ fs	$\Delta\sigma$/ fs	t_0/ fs	Δt_0/ fs	τ_1/ fs	$\Delta\tau_1$/ fs	a_1	Δa_1	a_{cis}	Δa_{cis}
					S$_1$				cis formation	
520-530	205	10	798	8	950	30	1.27	0.03	0.100	0.001
500-510	177	8	739	7	880	30	1.24	0.03	0.104	0.001
480-490	170	8	666	7	780	20	1.23	0.03	0.0799	0.002

Table 3.7: Literature values for dynamics at (490-530) nm from reference [12] labels as in table 3.6, without a_{cis} but with τ_3 as vibrational relaxation of the cis ground state.

| λ / nm	a_1	τ_1 / fs	a_3	τ_3 / fs
530	0.78	700	0.17	4200
500	0.81	700	0.06	4100
490	0.83	700	0.04	3700
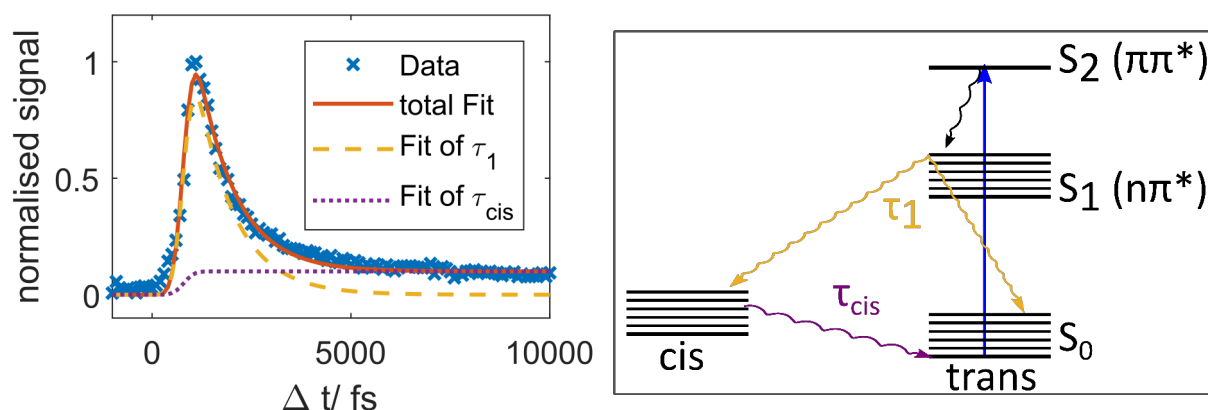
Figure 3.11: Fits of aminoazobenzene relaxation dynamics in ethanol solution at (520-530) nm. Sketch of the respective paths on the right.

(430-445) nm In the (430 to 445) nm range definitely trans bleaching accompanied by vibrational relaxation of the trans ground state (τ_4) can be distinguished. Values for τ_1 (shown in table 3.8 match literature values in table 3.9, while trans vibratonal decay times τ_4 do not match and vary strongly. This is again mainly due to the fit model, that features 8 parameters. Once again it has to be emphasized, that the experiment was not conducted at the magic angle. The bleaching and the signal recovery due to relaxation can be seen in figure 3.12.

Table 3.8: Fit of aminoazobenzene dynamics in ethanol solution at (430 to 445) nm, τ_{cis} is not displayed since decay time is in minutes to hours

λ / nm ... Wavelength range $\Delta\lambda = 1$ nm

σ / fs ... Standard deviation of the Gauss pulse that fills the state

t_0 / fs ... Time zero, fit

S_1 ... First excited state that is indirectly filled (nπ*)

trans vibrational relaxation ... vibrational relaxation of the ground state trans

cis formation ... Bleaching, due to formation of the cis isomer

τ_x / fs ... Decay time constant of the respective state

a_x ... Preexponential factor, to weigh the decays

Δx ... Standard deviation of the respective fit value

					S₁				trans vibrational relaxation				cis formation	
λ / nm	σ/ fs	$\Delta\sigma$/ fs	t_0/ fs	Δt_0/ fs	τ_1/ fs	$\Delta\tau_1$/ fs	a_1	Δa_1	τ_4/ fs	$\Delta\tau_4$/ fs	a_4	Δa_4	a_{cis}	Δa_{cis}
440-445	141	7	566	6	650	20	2.43	0.04	10000	1000	0.36	0.01	0.41	0.01
430-440	162	9	530	7	663	25	2.77	0.04	6000	700	0.38	0.03	0.615	0.007

Table 3.9: Literature values for dynamics at (445) nm from reference [12]

Labels as in table 3.8, without a_{cis}.

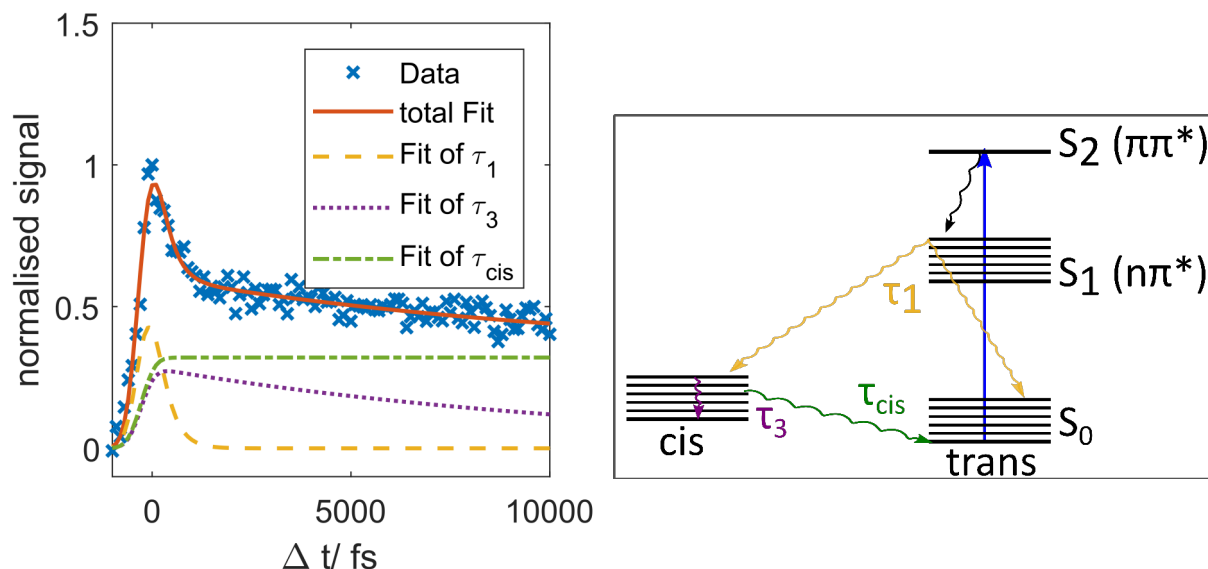| λ / nm	a_1	τ_1 / fs	a_4	τ_4 / fs
445	0.81	600	0.19	13000
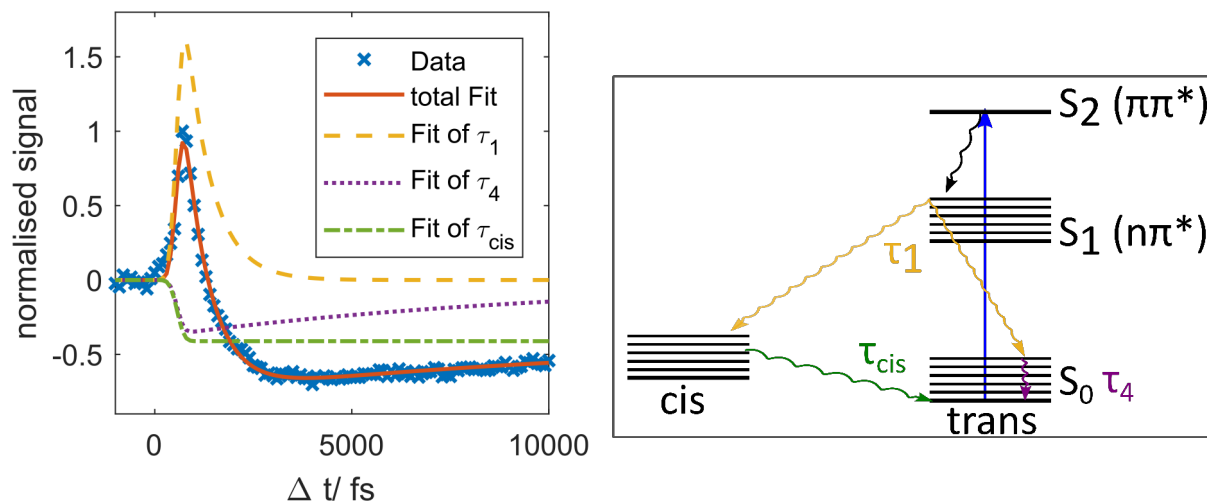
Figure 3.12: Fits of aminoazobenzene relaxation dynamics in ethanol solution at (440-445) nm. Sketch of the respective paths on the right.

(320-350) nm Finally the cis transition at (320 to 350) nm definitely exhibits signal of vibrational relaxation in the cis ground state (τ_3) and additionally again τ_1 and τ_{cis} signal, see figure 3.13. To my knowledge this state has not been measured so far. Since the time constants of vibrational relaxation can be distinguished a lot easier than at the (470 to 530) nm absorption

Table 3.10: Fit of aminoazobenzene dynamics in ethanol solution at (320 to 340) nm, τ_{cis} is not displayed since decay time
is in minutes to hours
λ / nm ... Wavelength range $\Delta\lambda = 1$ nm
σ / fs ... Standard deviation of the Gauss pulse that fills the state
t_0 / fs ... Time zero, fit
S_1 ... First excited state that is indirectly filled ($n\pi^*$)
cis vibrational relaxation ... vibrational relaxation of the ground state cis
cis formation ... Formation of the cis isomer
τ_x / fs ... Decay time constant of the respective state
a_x ... Preexponential factor, to weigh the decays
Δx ... Standard deviation of the respective fit value

S_1				cis vibrational relaxation				cis formation	
τ_1/ fs	$\Delta\tau_1$/ fs	a_1	Δa_1	τ_3/ fs	$\Delta\tau_3$/ fs	a_3	Δa_3	a_3	Δa_3
310	80	1.3	0.4	12000	2000	0.29	0.01	0.32	0.01
900	200	0.80	0.09	11000	3000	0.27	0.02	0.22	0.02

band this backs the decision to use a supercontinuum source, that stretches into the UV. Data and fits are shown in table 3.10). Further by looking at time zero t_0 and comparing it with table 3.2 the probe chirp is apparent.

Figure 3.13: Fits of aminoazobenzene relaxation dynamics in ethanol solution at (330-340) nm. Sketch of the respective paths on the right.

Conclusion of solution measuremens   Once again it has to be emphasized, that since no reference trace has been acquired there are at least six fit parameters and the stated uncertainty is just the standard deviation of the fit error. Especially the initial guess of the time of overlap (t_0) highly influences the fit. Nevertheless decay times of S_2 and S_1 and the vibrational relaxations show the same dependency as in reference [12]. Even though t_0 is a very flexible fit parameter, it shows the right wavelength dependency due to probe chirp.

3.3 Thin Films

3.3.1 Sample Preparation and Characterisation

The first samples were prepared by Katrin Unger and the process is documented in reference [23]. Due to degradation effects the absorption peak of trans amino-azobenzene shifted further to the blue. Thus a new series of samples was necessary, in order to efficiently pump the absorption band with the second harmonic. Together with Ass. Prof. Anna Maria Coclite a new series of samples was produced. To measure the absorbance a commercial UV-VIS spectrometer (Shimadzu UV-1800) with a reference path is used. Figure 3.14a shows static absorption spectra of the degraded old samples whereas 3.14b shows absorption of the new ones. The absorption differs highly due to the fact, that the aminoazobenzene film is not evenly spread on the substrate and. In figure 3.15 the bleaching of the ground state due to isomerisation after irradiation of the sample with an UV-Lamp for 1 minute can be seen. A longer exposure does not lead to an increase of bleaching. Sample 5 is chosen since the signal difference after UV irradiation is the most distinct among all samples. In figure 3.15 even the cis absorption band at $\sim$500 nm is visible and the cis ($\pi\pi^*$) absorption at $\sim$330 nm can be perceived.

(a) old thin films.
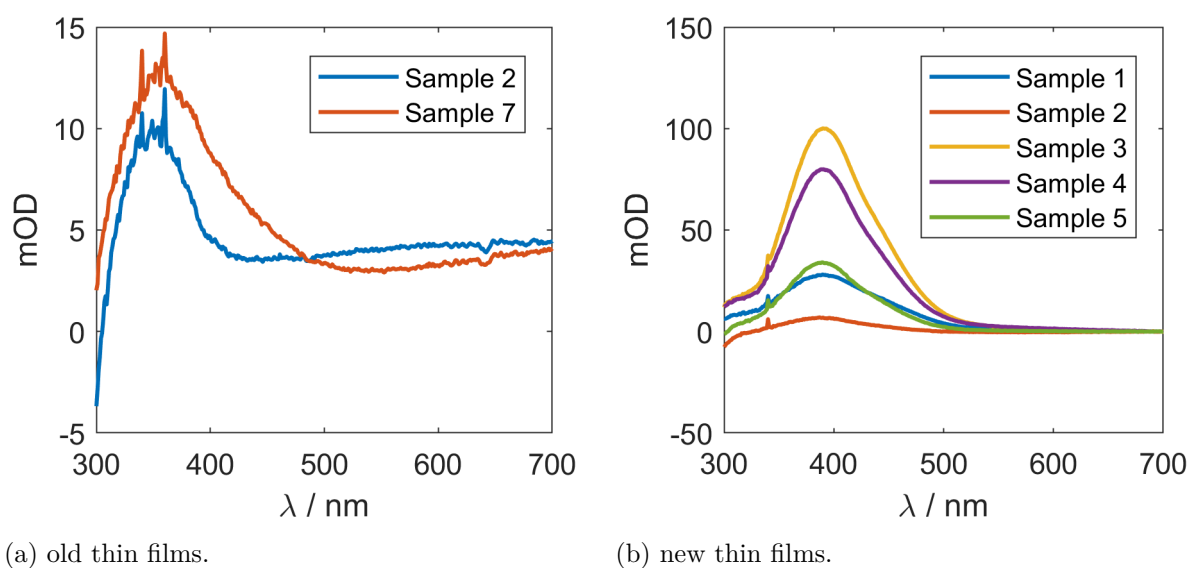
(b) new thin films.

Figure 3.14: UV-VIS spectrometer absorption spectra of thin films
new samples data: Azobenzene_sample*_longer_bath,
old samples data: Azobenzene_Sample*_old.
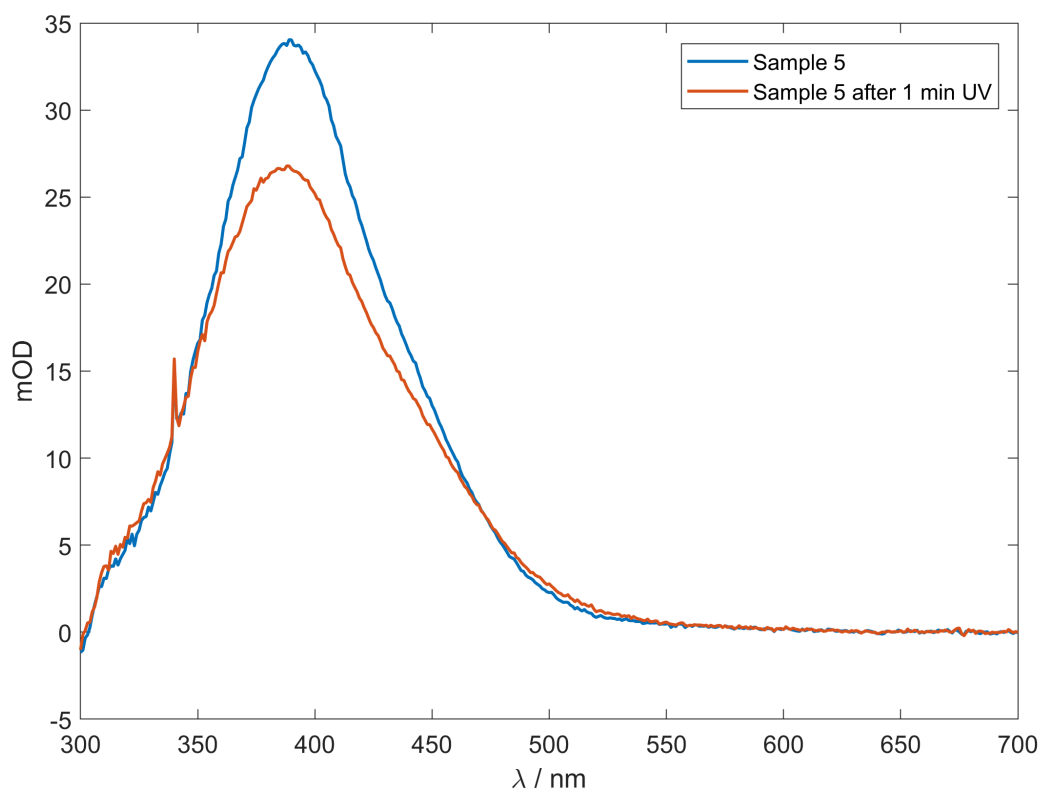
Figure 3.15: UV-VIS spectrometer absorption spectra of new aminoazobenzene thin film number 5, before and after 1 min of UV irradiation
before illumination data: Azobenzene_Sample5_longer_bath,
after UV illumination data: Azobenzene_sample5_longer_bath_after_1min_UV.

3.3.2 Reproduction and Power Drift

To reproduce the static absorption measurements of the commercial spectrometer, shown in figure 3.14, the samples are inserted in the setup presented in section 2.4. The speaker translates the sample while 50000 spectra with white light only are acquired. Next 50000 reference spectra of the substrate are acquired and the static absorption is calculated. In figure 3.16 the static absorption measurement is shown. Comparing it to figure 3.15, agreement is found in absorption of the trans ground state. Since the sample is constantly moved and the sample is not homogeneously coated with aminoazobenzene, it is reasonable that the absorption values differ a little. The spike at around 770 nm can be understood by looking at figure 2.3 on page 25, here an artifact of the bandpass filter occurs. Although the filter cuts the spectrum at 610 nm a little signal around 770 nm remains that is highly fluctuating.

The next step is to see if bleaching of the ground state can be observed, as in figure 3.15. Therefore the sample is mounted on the speaker and two series of spectra are recorded. First a series of white light only spectra are acquired, then the second harmonic is focused onto the sample for 10 min. Afterwards again a series of white light spectra is acquired and compared to the initial one. One would expect negative optical density around 400 nm due to isomerisation to cis aminoazobenzene. In figure 3.17 we can see that the change of optical density is below the noise level. Even applying a moving mean on the data does not lead to a definite conclusion.

The next step was to clarify if averaging over a longer period could improve the measurement. White light spectra were acquired for about one hour and their fluctuations are shown in figure 3.18. The white light changes in intensity due to a power drift of the laser system. To verify, that this is not an artifact of the detector, 10000 spectra were recorded over ~7.5 min using a cooled CCD camera attached to a monochromator (Andor DU401_DD), illustrated in figure 3.19. The result is the same. Therefore averaging the signal over a long time will not improve the result, but smear it out. On the other hand due to fluctuations within ~3.8 ms (spectrometer minimum acquisition time), that arise from the white light motion, the spectrometer or the laser (as can be seen in figure 3.20), the average signal difference within 3.8 ms is ~2 mOD. Either a reference path has to be introduced or shot to shot detection established as is discussed in chapter 4.
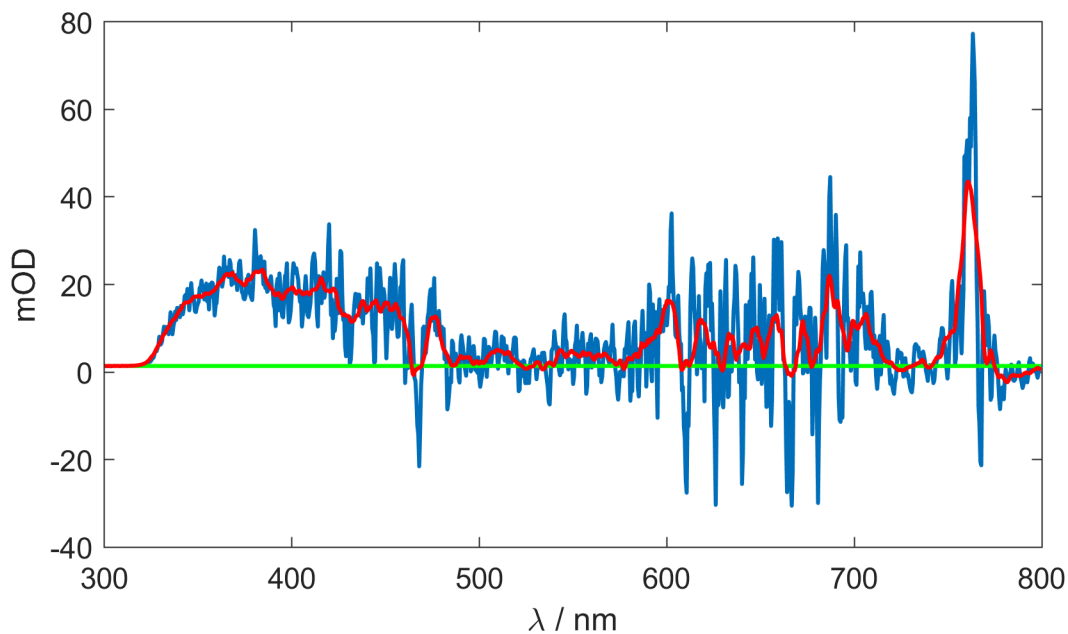
Figure 3.16: Optical density of aminoazobenzene thin film measured by comparing the mean of 50000 spectra at 3 ms integration time, of substrate only and sample 5. Blue: spectrum with 0.5 nm bin size, red: moving mean with 5 nm window size. Green: zero line.
substrate file: spectrum_jitter0353
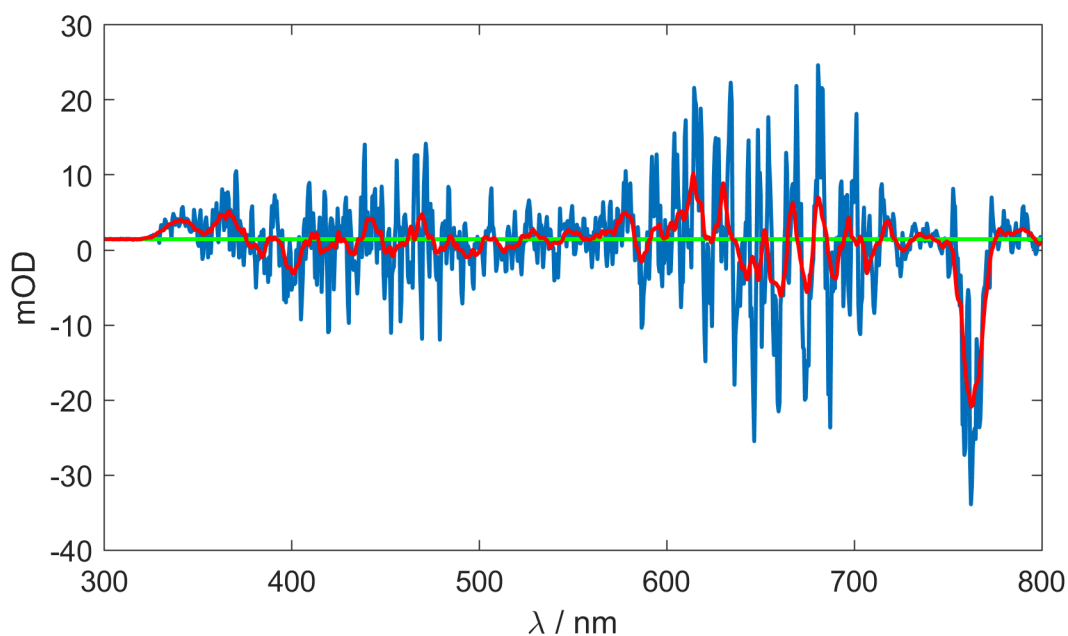sample file: spectrum_jitter0354

Figure 3.17: Change of optical density after 10 min of irradiation with 7 µJ of second harmonic pulses. Calculated by comparing the mean of 50000 spectra before and after irradiation. Blue: spectrum with 0.5 nm bin size, red: moving mean with 5 nm window size. Green: zero line.
Before second harmonic file: spectrum_jitter0355
After second harmonic file: spectrum_jitter0357
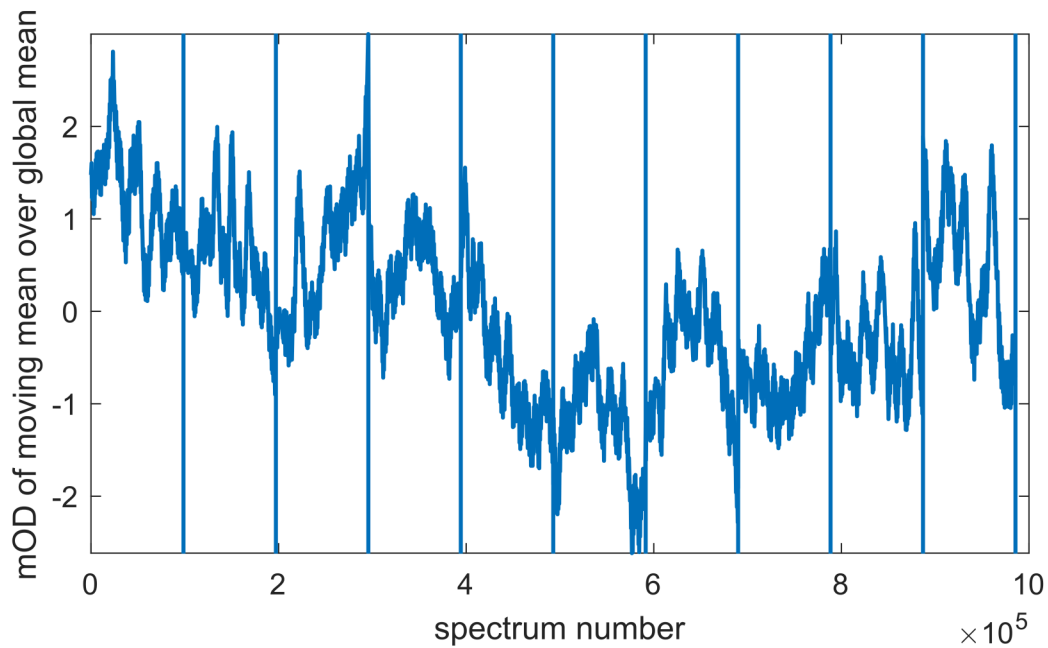
Figure 3.18: Long time drift of white light, 10 times 10^5 3 ms spectra over a time of $\sim$1 h. Mean of data at (300 to 700) nm. Lines indicate a new measurement, moving mean window size: 5000 spectra
data: spectrum_jitter0398-spectrum_jitter0407
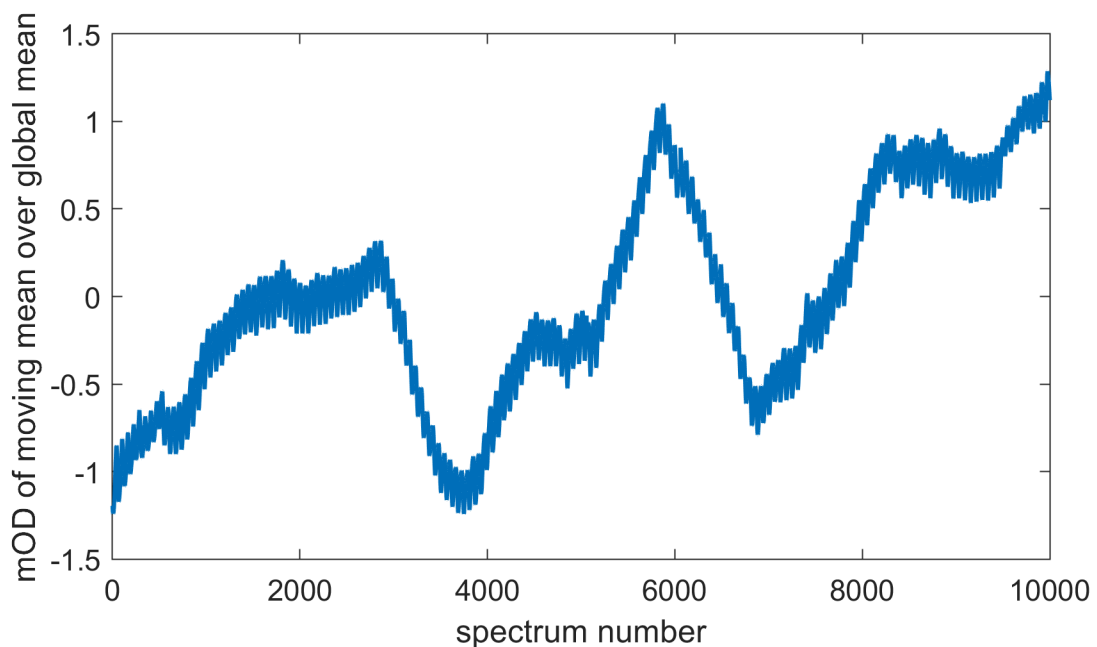
Figure 3.19: Drift of white light recorded with Andor camera, 10000 spectra at around 522 nm over a time of $\sim$ 7.5 min, Sensor temperature $-50\,°C$, moving mean window size: 1000 spectra
data: 522nm_1129u_10000_spectra_minus50_light_on_30_ms.sif
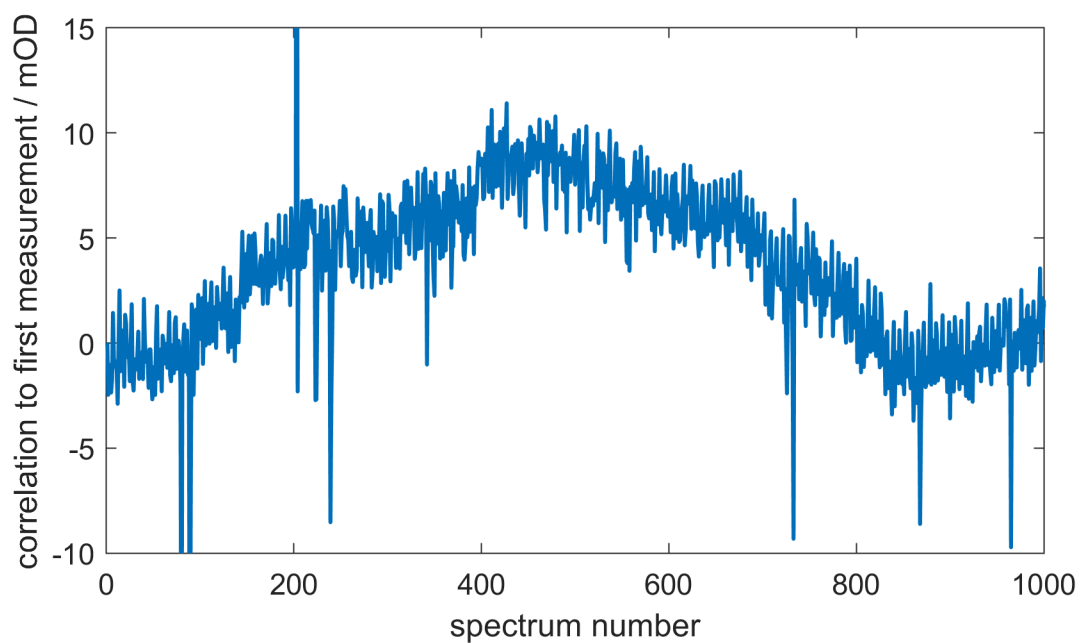
Figure 3.20: Signal change with respect to an arbitrarily chosen intial spectrum. Average signal change of two consecutive spectra: $\sim 2\,\mathrm{mOD}$.
Data: spectrum_jitter0398-spectrum_jitter0407

CHAPTER 4

Outlook

4.1 Fast Acquisition

Since averaging over many pulses leads to noise due to a laser drift (see section 3.3.2) and even within the 3.8 ms acquisition time of the spectrometer ($\sim$12 pulses) a signal drift of around 2 mOD is apparent, detection of single pulses might improve the setup. Therefore a photo-multipler / photodiode-monochromator setup is a good candidate, as it can be read out at a pulse-to-pulse basis. The probe pulse is filtered using the monochromator and detected by the photomultiplier/photodiode. Now the problem remains, how to chop the pump pulse at 3 kHz frequency. A mechanical chopper, even if it is well manufactured, will probably block parts of the beam. A more accurate and standard solution in optics is to use a Pockels cell. Once high voltage is applied, it acts as a wave plate. Using it as a half-wave plate, the polarisation of the pump beam can be changed from s to p or vice versa. Adding a Brewster window or a polariser in front of the sample achieves a chopper that can switch with up to nanosecond precision.

4.2 Rotation of the Sample

In order to guarantee, that the sample is not pumped into triplet states or thermally damaged, due to high pump intensity it is necessary to move the sample without tilting or shaking it out of spatial overlap. A linear actuator has exactly this downside and additionally the acceleration has to be very high. Therefore rotation of the sample is the easiest solution. In order to ensure, that no focus area is pumped twice a rotational frequency of at least 40 Hz, realistically 100 Hz is necessary. A belt-drive including pulleys can work at these speed, but bearings with suitable dimensions are not easily available, so that this task is postponed until a sufficient signal to noise ratio of the white light spectrum can be guaranteed.

4.3 Reference Path

If a faster acquisition leads to a better accuracy, the next step for higher accuracy is to get a reference beam. As treated in section 2.5, both probe and reference have to be coupled in equally good into their respective detector. An array detector, where probe and reference beam are positioned vertically separate on the same horizontal position ensures, that no individual detector noise affects the measurement. No matter if two or one detectors are used, the fine adjustment of the beams is a task hard to fulfill with a rotating/tilting white light source and probably better suited, if sapphire or another source, that does not need translation is used.

Appendix

A.1 Laplace model for non linear optics

This derivation was performed by Pascal Heim and has been modified and adapted for better readability by the author. Looking at an electron in a potential U, it experiences the restoring force $-\nabla U$, that can be expressed as expansion:

$$\nabla U = \sum_{n \geq 1} U^{(n)} x^n$$

The equation of motion for this charge can be expressed in the well known form, now including a weak external force F.

$$\ddot{x} + 2\gamma \dot{x} = -\nabla U + F$$

with x, the displacement of the charge and γ the damping constant.

Assuming only a weak F, the higher order terms $U^{(n)} x^n$ are much smaller than $U^{(1)} x$ and therefore the use of perturbation theory is legitimate. Introducing the dummy parameter λ which we can continuously vary between 0 and 1, we can rewrite the equation of motion:

$$\ddot{x} + 2\gamma \dot{x} = -\nabla U + \lambda F$$

Expanding the solution in terms of λ:

$$x = \sum_{m \geq 1}^{M} \lambda^m x^{(m)}$$

we can use the multinomial theorem to calculate x^n:

$$x^n = (\lambda^1 x^{(1)} + \lambda^{(2)} x^2 + \cdots + \lambda^M x^{(M)})^n$$

$$= \sum_{k_1 + k_2 + \cdots + k_M = n} \binom{n}{k_1, k_2, \ldots, k_M} \prod_{m=1}^{M} (\lambda^m x^{(m)})^{k_m}$$

$$= \sum_{\{k_m\}} \binom{n}{\{k_m\}} \prod_{m=1}^{M} \lambda^{m k_m} x^{(m)^{k_m}} = \sum_{\{k_m\}} \binom{n}{\{k_m\}} \lambda^{\sum_{m=1}^{M} m k_m} \prod_{m=1}^{M} x^{(m)^{k_m}}$$

with

$$\sum_{m=1}^{n} k_m = n,$$

the sum of exponents in the epansion have to match n. Remember: $(a+b)^n = \sum_{k=0}^{n} \binom{n}{k} a^k b^{n-k}$
Inserting into the equation of motion leads to:

$$\sum_{m \geq 1} \lambda^m \left(\ddot{x}^{(m)} + 2\gamma \dot{x}^{(m)} \right) + \sum_{n \geq 1} U^{(n)} \sum_{\{k_m\}} \binom{n}{\{k_m\}} \lambda^{\sum_{m=1}^{n} m k_m} \prod_{m=1}^{n} x^{(m)^{k_m}} = \lambda F$$

Because λ is arbitrary every pre factor in font of every power of λ must solve the equation separately. Sorting the equation by powers of λ leads to,

$$\sum_{m \geq 1} \lambda^m \left(\ddot{x}^{(m)} + 2\gamma \dot{x}^{(m)} + U^{(1)} x^{(m)} + \underbrace{\sum_{n=2}^{m} U^{(n)} \sum_{\{k_{m'}\}} \delta \left(\sum_{m'=1}^{n} m' k_{m'} - m \right) \binom{n}{\{k_{m'}\}} \prod_{m'=1}^{n} x^{(m')^{k_{m'}}}}_{F^{(m)}} \right) = \lambda F \tag{A.1}$$

Since we drew out the $x^{(m)}$ term we get another restriction $(m' < m)$ within the sum $\sum_{n=2}^{m} U^{(n)} \sum_{\{k_{m'}\}} \ldots$

A.1.1 First order $\left(\lambda^1\right)$

$$\ddot{x}^{(1)} + 2\gamma\dot{x}^{(1)} + U^{(1)}x^{(1)} = F$$

Looking at the solution for the harmonic oscillator we find that $U^{(1)} = \omega_0^2$. We are only interested in the steady state solution (inhomogeneous solution):

We use the Fourier transform to find a solution.

$$F(t) = \frac{1}{\sqrt{2\pi}} \int \tilde{F}(\omega)e^{-i\omega t}d\omega$$

$$x^{(1)}(t) = \frac{1}{\sqrt{2\pi}} \int \tilde{x}^{(1)}(\omega)e^{-i\omega t}d\omega$$

Note that $F(t)$ and $x(t)$ are real functions. This means the following must be true:

$$\tilde{F}(-\omega) = \tilde{F}^*(\omega)$$

Solving $x(\omega)$ we find:

$$\tilde{x}^{(1)}(\omega) = \frac{\tilde{F}(\omega)}{U^{(1)} - \omega^2 - 2i\gamma\omega} = \chi_x^{(1)}(\omega)\tilde{F}(\omega)$$

Here we see that $\chi^{(1)}(-\omega) = \chi^{{(1)}^*}(\omega)$. Note that if $\omega << U^{(1)}$ then $\chi^{(1)}$ gets independent of ω.

A.1.2 Higher order terms:

As derived before the solution for higher order terms can be expressed as:

$$\ddot{x}^{(m)} + 2\gamma\dot{x}^{(m)} + U^{(1)}x^{(m)} = -\sum_{n=2}^{m} U^{(n)} \sum_{\{k_{m'}\}} \delta\left(\sum_{m'=1}^{n} m'k_{m'} - m\right) \binom{n}{\{k_{m'}\}} \prod_{m'=1}^{M} x^{(m')k_{m'}} = F^{(m)}$$

Fourier transforming the left hand side of the equation leads to the expression already derived of the first order term. Since the Fourier transform of the product on the right hand side, by definition is a convolution:

$$\mathcal{F}\{f \circledast g\} = \mathcal{F}\{f\}\mathcal{F}\{g\} \tag{A.2}$$

we can rewrite the equation:

$$\tilde{x}^{(m)}(\omega) = -\chi_x^{(1)}(\omega) \sum_{n=2}^{m} U^{(n)} \sum_{\{k_{m'}\}} \delta\left(\sum_{m'=1}^{n} m'k_{m'} - m\right) \binom{n}{\{k_{m'}\}} \underset{m'=1}{\overset{M}{\circledast}} \tilde{x}^{(m')k_{m'}}$$

In order to calculate this convolution we define frequencies $\omega_{m'}$. The resulting frequency of the convolution may be any matching combination of different frequencies. Therefore the convolution can be rewritten as:

$$\overset{M}{\underset{m'=1}{\circledast}} \tilde{x}_{m'} = \int \delta \left(\sum_{m'=1}^{M} \omega_{m'} - \omega \right) \prod_{m'=1}^{M} \tilde{x}_{m'}(\omega_{m'}) d\omega_{m'}$$

Here we can see that every $\tilde{x}^{(m)}$ is proportional to $\prod_{m=1}^{M} \tilde{F}^{(m)}(\omega_m)$ and products of $\chi_x^{(1)}(\omega)$.

Second order (λ^2)

The equation of motion,

$$\ddot{x}^{(2)} + 2\gamma\dot{x}^{(2)} + U^{(1)}x^{(2)} + U^{(2)}x^{(1)^2} = 0$$

and after Fourier transformation gives:

$$\tilde{x}^{(2)}(\omega) = -U^{(2)}\chi_x^{(1)}(\omega) \left(\tilde{x}^{(1)} \circledast \tilde{x}^{(1)} \right)(\omega)$$

Remember, that $m' < m$ and the weighted sum of $x^{(m')}$ exponents have to match ($m = 2$). Again we introduce arbitrary frequencies ω_1 and ω_2 that match the desired frequency ω. Also inserting the definition of $\tilde{x}^{(1)}$ gets:

$$\tilde{x}^{(2)}(\omega) = \int \int \underbrace{-U^{(2)}\chi_x^{(1)}(\omega_1 + \omega_2)\chi_x^{(1)}(\omega_1)\chi_x^{(1)}(\omega_2)\delta(\omega - (\omega_1 + \omega_2))}_{\chi_x^{(2)}(\omega;\omega_1,\omega_2)} \tilde{F}(\omega_1)\tilde{F}(\omega_2)d\omega_1 d\omega_2$$

Solution for $F(t) = \tilde{F}(\omega_1)e^{-i\omega_1 t} + \tilde{F}(\omega_2)e^{-i\omega_2 t} + c.c.$ with $\omega_1 \neq \omega 2$ Note that the result is a convolution of the two frequency parts, with themself and the second frequency.

$$\tilde{x}^{(2)}(0) = \chi_x^{(2)}(0;\omega_1,-\omega_1)\tilde{F}(\omega_1)\tilde{F}(-\omega_1) + \chi_x^{(2)}(0;\omega_2,-\omega_2)\tilde{F}(\omega_2)\tilde{F}(-\omega_2)$$
$$\tilde{x}^{(2)}(2\omega_1) = \chi_x^{(2)}(2\omega_1;\omega_1,\omega_1)\tilde{F}(\omega_1)^2$$
$$\tilde{x}^{(2)}(2\omega_2) = \chi_x^{(2)}(2\omega_2;\omega_2,\omega_2)\tilde{F}(\omega_2)^2$$
$$\tilde{x}^{(2)}(\omega_1 + \omega_2) = \chi_x^{(2)}(\omega_1 + \omega_2;\omega_1,\omega_2)\tilde{F}(\omega_1)\tilde{F}(\omega_2)$$
$$\tilde{x}^{(2)}(\omega_1 - \omega_2) = \chi_x^{(2)}(\omega_1 - \omega_2;\omega_1,\omega_2)\tilde{F}(\omega_1)\tilde{F}(-\omega_2)$$

We see, that we achieve frequency doubling, sum frequency generation and difference frequency generation. Further an $\omega = 0$ term, that is called optical rectification is generated.

Third order (λ^3)

The equation of motion,

$$\ddot{x}^{(3)} + 2\gamma\dot{x}^{(3)} + U^{(1)}x^{(3)} + 2U^{(2)}x^{(1)}x^{(2)} + U^{(3)}x^{(1)^3} = 0$$

and in frequency domain:

$$\tilde{x}^{(3)}(\omega) = -\chi_x^{(1)}(\omega)\left(2U^{(2)}\left(\tilde{x}^{(1)} \circledast \tilde{x}^{(2)}\right)(\omega) + U^{(3)}\left(\tilde{x}^{(1)} \circledast \left(\tilde{x}^{(1)} \circledast \tilde{x}^{(1)}\right)\right)(\omega)\right)$$
$$= \int\int\int \chi_x^{(3)}(\omega;\omega_1,\omega_2,\omega_3)\tilde{F}(\omega_1)\tilde{F}(\omega_2)\tilde{F}(\omega_3)d\omega_1 d\omega_2 d\omega_3$$

Remember, that $m' < m$ and the sum of exponents have to match ($m = 3$). Again we introduce yet another frequency ω_3 that is arbitrarily set so that $\sum_{m'}\omega_{m'} = \omega$. It is quite surprising, that $\chi_x^{(3)}$ is also dependent on $U^{(2)}$ and therefore $\chi_x^{(2)}$ an effect, that is completely neglected in the simple Kerr-effect approximation.

$$\chi_x^{(3)}(\omega;\omega_1,\omega_2,\omega_3) = [2U^{(2)^2}\chi_x^{(1)}(\omega_1)\chi_x^{(1)}(\omega_2+\omega_3)\chi_x^{(1)}(\omega_2)\chi_x^{(1)}(\omega_3)$$
$$- U^{(3)}\chi_x^{(1)}(\omega_1)\chi_x^{(1)}(\omega_2)\chi_x^{(1)}(\omega_3)]\chi_x^{(1)}(\omega_1+\omega_2+\omega_3)\delta(\omega-(\omega_1+\omega_2+\omega_3))$$

Now a solution for $F(t) = \tilde{F}(\omega_1)e^{-i\omega_1 t} + \tilde{F}(\omega_2)e^{-i\omega_2 t} + \tilde{F}(\omega_3)e^{-i\omega_3 t} + c.c.$ we find 22 frequency components (44 if negative frequencies count as different)

$$\omega_1, \omega_2, \omega_3, 3\omega_1, 3\omega_2, 3\omega_3, (\pm\omega_1 \pm \omega_2 \pm \omega_3),$$
$$(2\omega_1 \pm \omega_2), (2\omega_1 \pm \omega_3), (2\omega_2 \pm \omega_3), (2\omega_2 \pm \omega_1),$$
$$(2\omega_3 \pm \omega_1), (2\omega_3 \pm \omega_2)$$

e.g.:

$$\tilde{x}^{(3)}(\omega_1) = \int\int\int \chi_x^{(3)}(\omega_1;\omega_1,\omega_2,-\omega_2)\tilde{F}(\omega_1)\tilde{F}(\omega_2)\tilde{F}(-\omega_2)d\omega_1 d\omega_2 d\omega_2$$
$$+ \int\int\int \chi_x^{(3)}(\omega_1;\omega_1,\omega_3,-\omega_3)\tilde{F}(\omega_1)\tilde{F}(\omega_3)\tilde{F}(-\omega_3)d\omega_1 d\omega_3 d\omega_3$$

A.1.3 Connection to non-linear polarization

$$P^{(n)}(\omega) = -Ne\tilde{x}^{(n)}(\omega)$$

$$P(\omega) = \sum_{n=1}^{\infty} P^{(n)}(\omega)$$

with electron density N and the fundamental charge e.

A.2 Expectation Value for Absorption

The derivation was initialy performed by Pascal Heim and has been adapted and extended by the author. In order to measure the absorption of a sample we are interested in a ratio $\frac{I_0}{I}$ or rewritten $\frac{x}{y}$. Now we assume that the values of x and y are Gaussian distributed ($g(x - \mu, \sigma_x)$, with mean value μ and standard deviation σ_x).

$$g(x - \mu, \sigma_x) = \frac{1}{\sqrt{2\pi\sigma_x^2}} e^{-\frac{(x-\mu_x)^2}{2\sigma_x^2}} \tag{A.3}$$

The Likelihood of this distribution is:

$$\mathcal{L} = \prod_{i=1}^{N} g(x_i - R\mu_y, \sigma_x) g(y_i - \mu_y, \sigma_y) \tag{A.4}$$

We know that $\mu_x = R\mu_y$, where R is the desired scaling factor that represents the signal difference due to absorption. Since we can only measure a sample of N_x/N_y x/y our Likelihood is:

$$\mathcal{L} = \frac{1}{\sqrt{2\pi\sigma_x^2}} e^{-\frac{\sum_{i=1}^{N_x}(x_i-\mu_x)^2}{2\sigma_x^2}} \frac{1}{\sqrt{2\pi\sigma_y^2}} e^{-\frac{\sum_{j=1}^{N_y}(y_j-\mu_y)^2}{2\sigma_y^2}}$$

$$= g\left(\sum_{i=1}^{N_x} x_i - N_x R\mu_y, \sigma_x\right) g\left(\sum_{j=1}^{N_y} y_j - N_y\mu_y, \sigma_y\right)$$

Now the maximum Likelihood for R is calculated,

$$\frac{\delta\mathcal{L}}{\delta R} = \frac{\sum_{i=1}^{N_x} x_i - N_x R\mu_y}{\sigma_x^2} N_x\mu_y\mathcal{L} = 0$$

$$R = \frac{\sum_{i=1}^{N_x} x_i}{N_x\mu_y} = \frac{\bar{x}}{\mu_y} \tag{A.5}$$

Now we are interested in the estimation for μ_y

$$\frac{\delta\mathcal{L}}{\delta\mu_y} = \left(\frac{\sum\limits_{i=1}^{N_x} x_i - N_x R\mu_y}{\sigma_x^2} RN_x + \frac{\sum\limits_{j=1}^{N_y} y_j - N_y\mu_y}{\sigma_y^2} N_y\right)\mathcal{L} = 0$$

Assume $\sigma_x = \sigma_y$, which is legitimate since the laser power deviates equally for x and y.

$$\underbrace{\sum_{i=1}^{N_x} x_i \sum_{i=1}^{N_x} x_i \frac{1}{\mu_y} - \sum_{i=1}^{N_x} x_i \sum_{i=1}^{N_x} x_i \frac{1}{\mu_y}}_{=0} + \sum_{j=1}^{N_y} y_j \cancel{N}_y - N_y^2 \mu_y = 0$$

$$\mu_y = \frac{\sum\limits_{j=1}^{N_y} y_j}{N_y} = \bar{y} \tag{A.6}$$

Insert A.6 into A.5:

$$R = \frac{\bar{x}}{\bar{y}}$$

A.3 Optical Setup and Devices
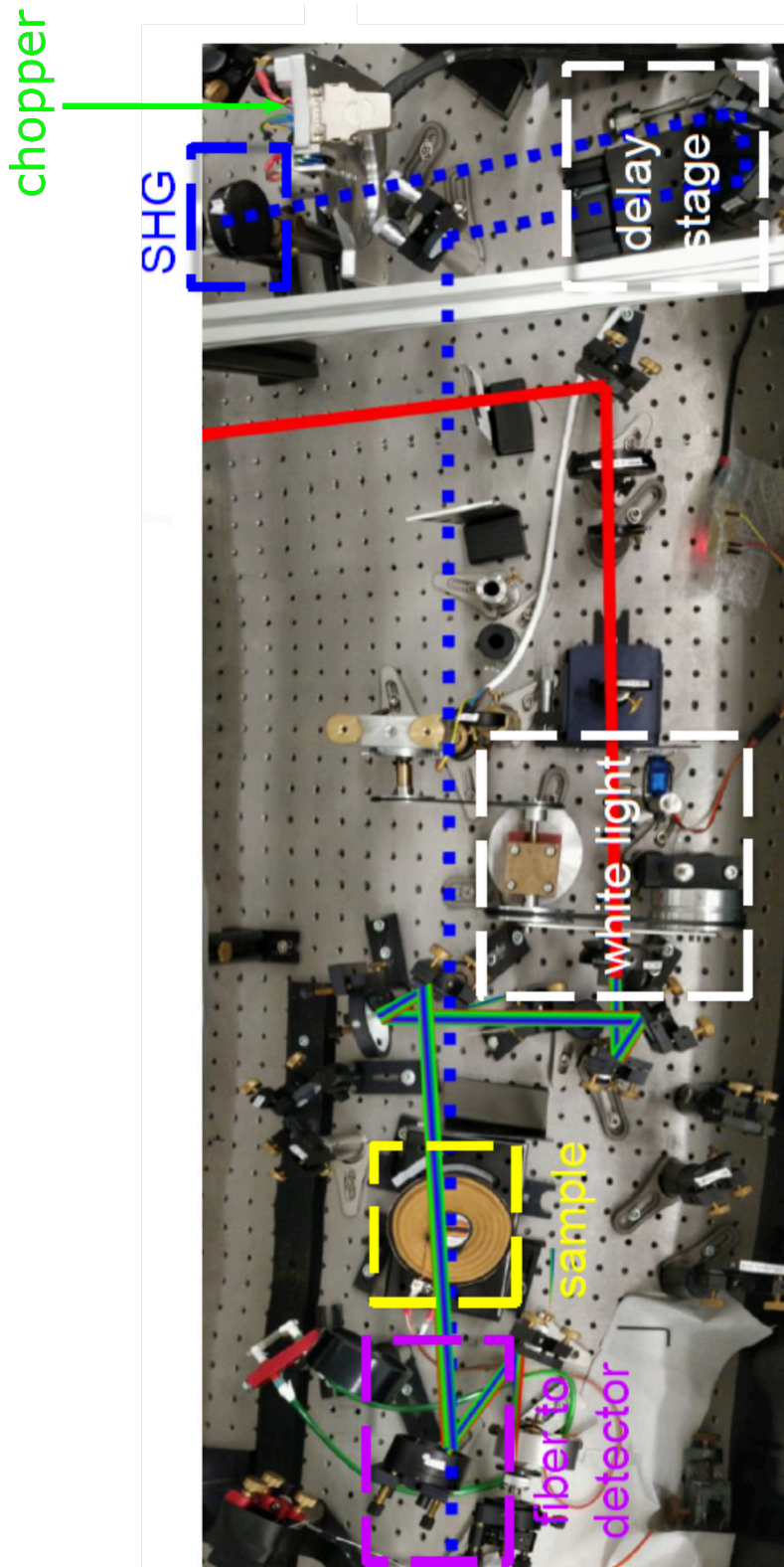
Figure A.1: Setup on the optical table.

HPUCO-2,A3-180/700-M-5BQ

HPUCO: Non-Contact Style
HUCO: Contact Style

Flange diameter:
2 = 1.3" OD flange
3 = 0.79" OD flange

wavelength range
(180-700) nm

focal length(5 mm)
and lens type

M = Multimode
S = Singlemode
P = Polarization maintaining

Receptacle Code:
3 = NTT-FC/PC
3S = Super NTT-FC/PC
3U = Ultra NTT-FC/PC
3A = Angled NTT-FC/PC
5 = SMA905 & 906
8 = AT&T-ST
SC = SC
SCA = Angled SC
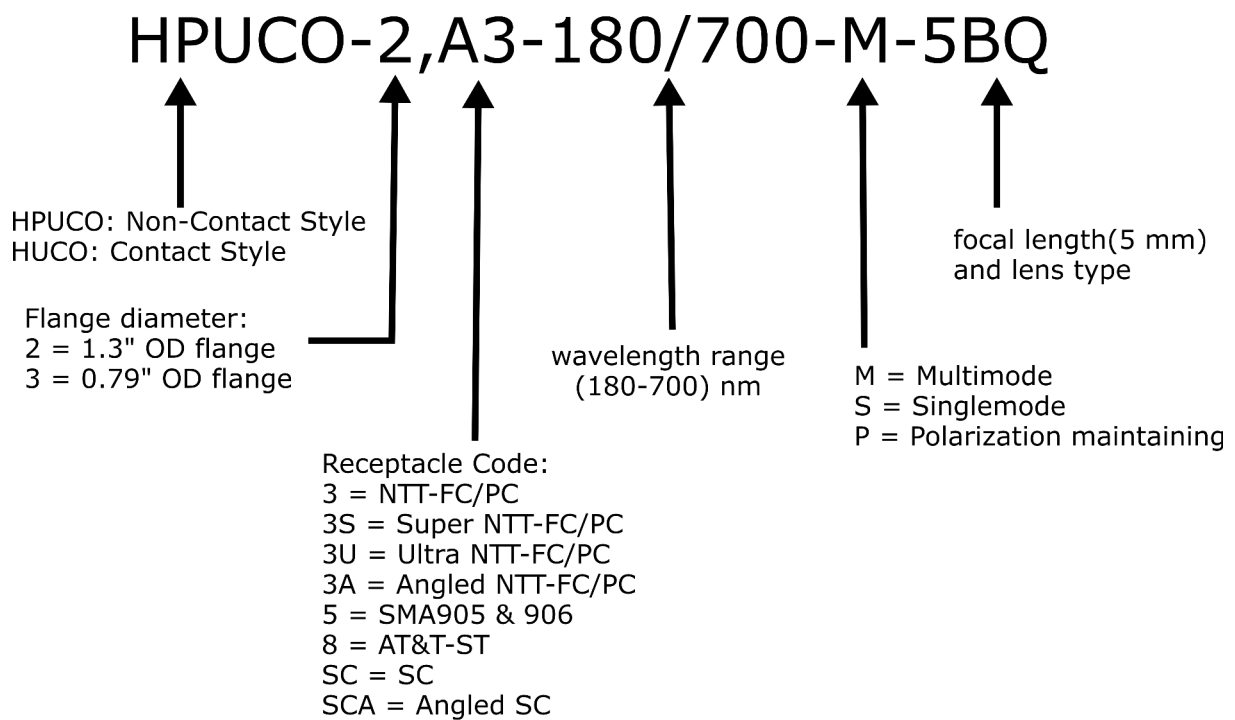
Figure A.2: Nomenclature of the fiber collimator, adapted from [35].
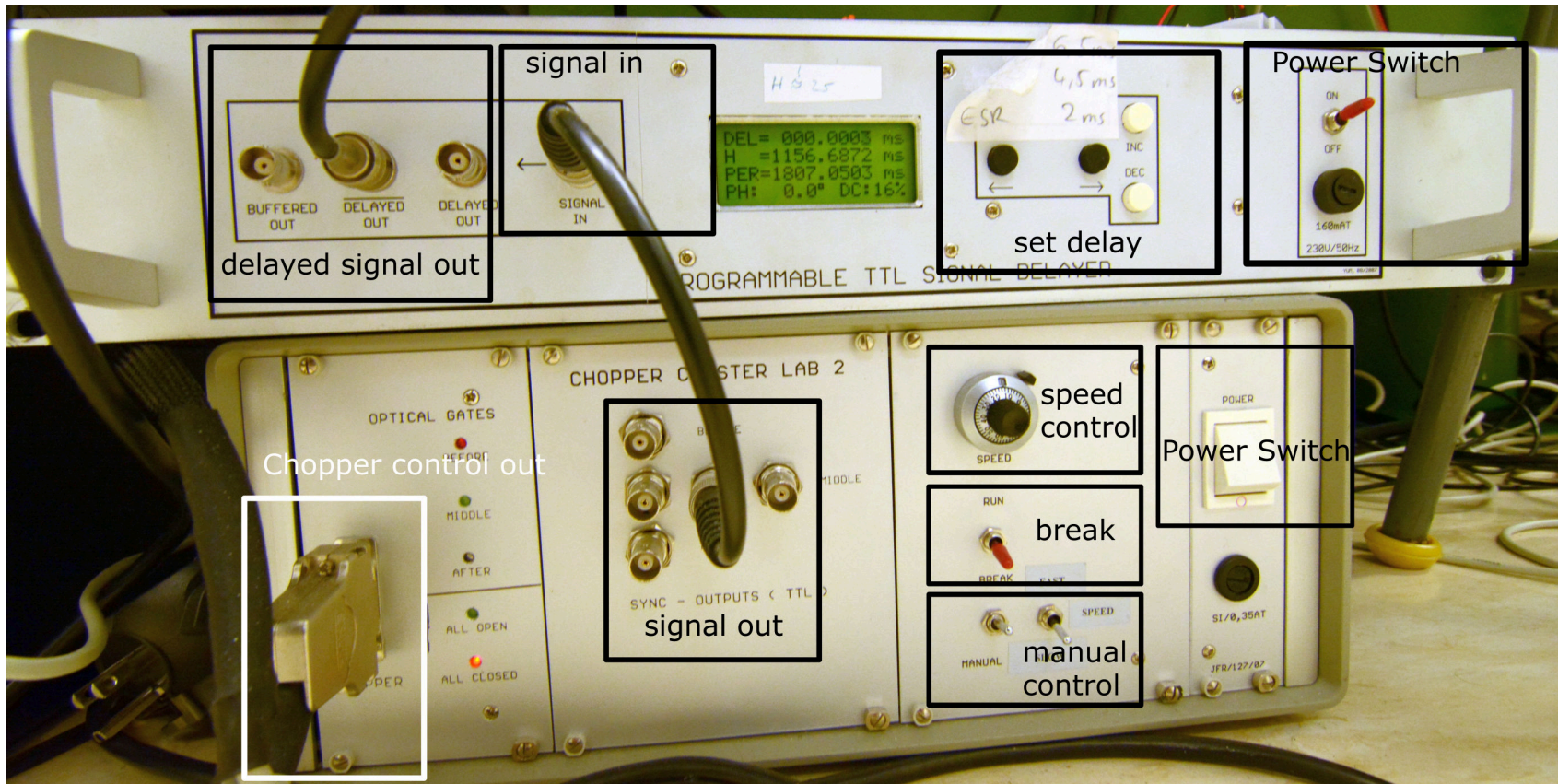
Figure A.3: Chopper control with TTL delay line on top. The green delay line display displays the delay time (DEL), time of signal high (H), period of the signal (PER) and phase delay (PH).
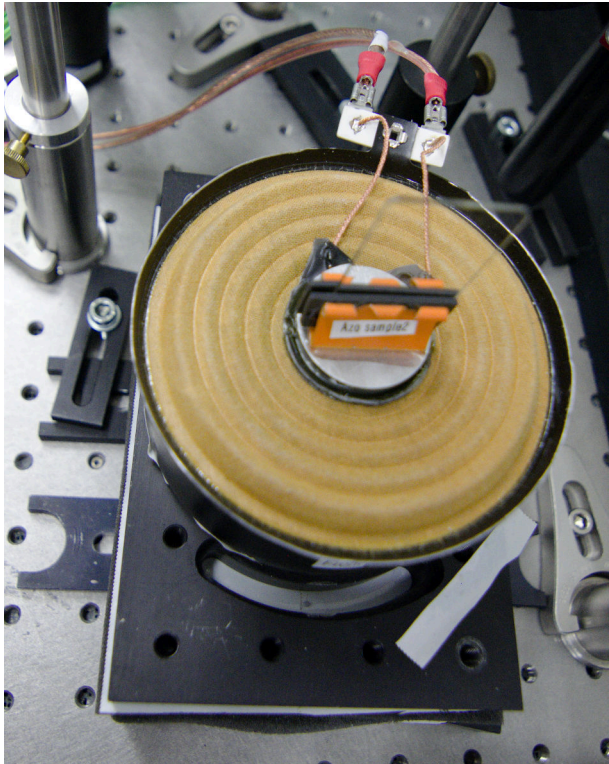
(a) Modified speaker to translate sample. Clamp with viton pads to fixate sample.

(b) The cuvette used [36]
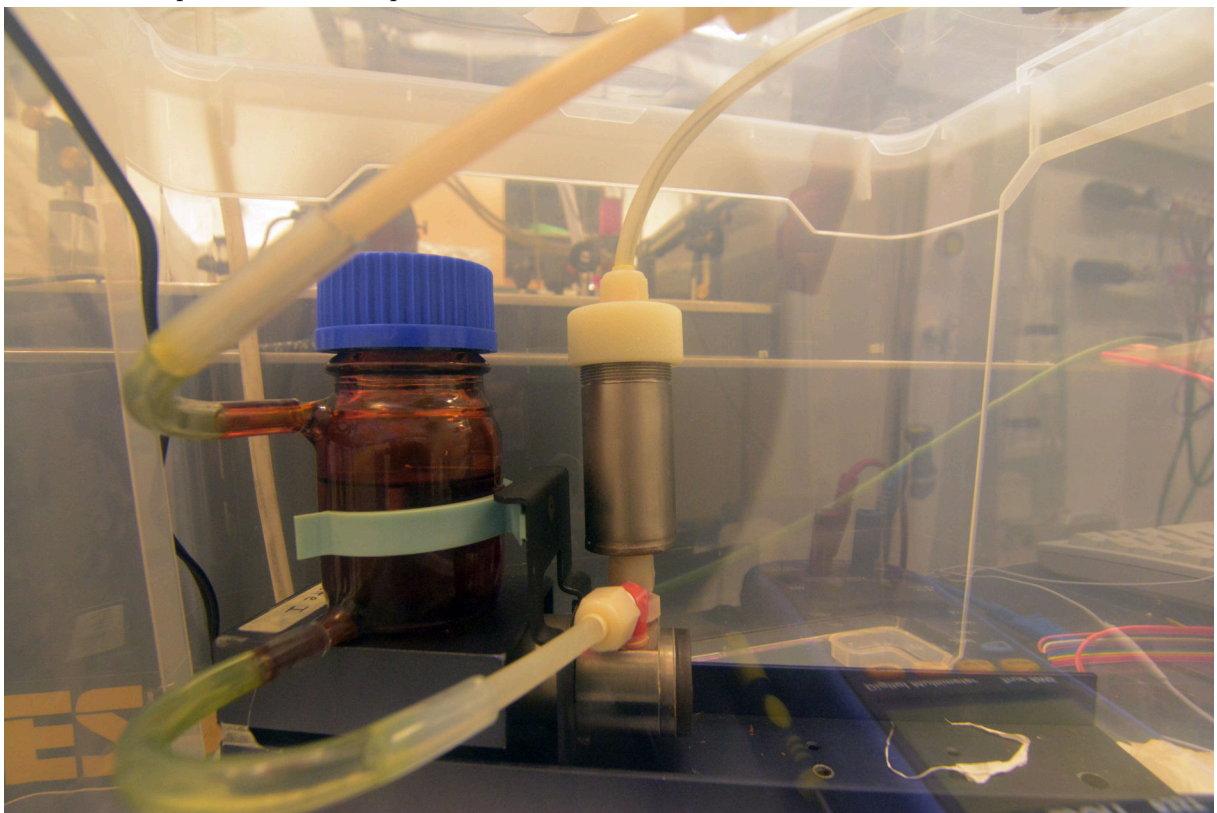
(c) dye pump used for measurements on solution

Figure A.4: Different devices used for liquid or solid samples

References

[1] R. Berera, R. van Grondelle, and J. T. M. Kennis. "Ultrafast transient absorption spectroscopy: principles and application to photosynthetic systems". In: *Photosynthesis Research* 101.2 (2009), pp. 105–118. ISSN: 1573-5079. DOI: 10.1007/s11120-009-9454-y. URL: https://doi.org/10.1007/s11120-009-9454-y.

[2] U. Megerle, I. Pugliesi, C. Schriever, C. F. Sailer, and E. Riedle. "Sub-50 fs broadband absorption spectroscopy with tunable excitation: putting the analysis of ultrafast molecular dynamics on solid ground". In: *Applied Physics B* 96.2 (2009), pp. 215–231. ISSN: 1432-0649. DOI: 10.1007/s00340-009-3610-0. URL: https://doi.org/10.1007/s00340-009-3610-0.

[3] A. M. Weiner. *Ultrafast Optics*. Ed. by G. Boreman. John Wiley & Sons, Inc., 2009.

[4] A. Brodeur and S. L. Chin. "Ultrafast white-light continuum generation and self-focusing in transparent condensed media". In: *J. Opt. Soc. Am. B* 16.4 (1999), pp. 637–650. DOI: 10.1364/JOSAB.16.000637. URL: http://josab.osa.org/abstract.cfm?URI=josab-16-4-637.

[5] Y. P. Raĭzer. "BREAKDOWN AND HEATING OF GASES UNDER THE INFLUENCE OF A LASER BEAM". In: *Soviet Physics Uspekhi* 8.5 (1966), p. 650. URL: http://stacks.iop.org/0038-5670/8/i=5/a=R05.

[6] J. Marburger. "Self-focusing: Theory". In: *Progress in Quantum Electronics* 4 (1975), pp. 35 –110. ISSN: 0079-6727. DOI: https://doi.org/10.1016/0079-6727(75)90003-8. URL: http://www.sciencedirect.com/science/article/pii/0079672775900038.

[7] URL: https://en.wikipedia.org/wiki/Gaussian_beam. (visited 05.2014).

[8] S. Uhlig. *Self-Organized Surface Structures with Ultrafast White-Light*. 2015. ISBN: 978-3-658-09893-3. DOI: 10.1007/978-3-658-09894-0.

[9] M. N. Polyanskiy. *Refractive index database*. https://refractiveindex.info. Accessed on 2018-08-03.

[10] I. Z. Kozma, P. Krok, and E. Riedle. "Direct measurement of the group-velocity mismatch and derivation of the refractive-index dispersion for a variety of solvents in the ultraviolet". In: *J. Opt. Soc. Am. B* 22.7 (2005), pp. 1479–1485. DOI: `10.1364/JOSAB.22.001479`. URL: `http://josab.osa.org/abstract.cfm?URI=josab-22-7-1479`.

[11] *Schott glas SCHOTT Zemax catalog 2017-01-20b*. URL: `http://www.schott.com`. (visited on 07.08.2018).

[12] Y. Wang, S. Zhang, S. Sun, K. Liu, and B. Zhang. "Ultrafast Excited State Dynamics of trans-4-Aminoazobenzene Studied by Femtosecond Transient Absorption Spectroscopy". In: *Chinese Journal of Chemical Physics* 26.6 (2013), pp. 651–655. DOI: `10.1063/1674-0068/26/06/651-655`. eprint: `https://doi.org/10.1063/1674-0068/26/06/651-655`. URL: `https://doi.org/10.1063/1674-0068/26/06/651-655`.

[13] P. J. M. Johnson, V. I. Prokhorenko, and R. J. D. Miller. "Stable UV to IR supercontinuum generation in calcium fluoride with conserved circular polarization states". In: *Opt. Express* 17.24 (2009), pp. 21488–21496. DOI: `10.1364/OE.17.021488`. URL: `http://www.opticsexpress.org/abstract.cfm?URI=oe-17-24-21488`.

[14] S. Schott, A. Steinbacher, J. Buback, P. Nuernberger, and T. Brixner. "Generalized magic angle for time-resolved spectroscopy with laser pulses of arbitrary ellipticity". In: *Journal of Physics B: Atomic, Molecular and Optical Physics* 47.12 (2014), p. 124014. URL: `http://stacks.iop.org/0953-4075/47/i=12/a=124014`.

[15] URL: `https://www.newport.com/n/gaussian-beam-optics`. (visited on 05.10.2017).

[16] H. M. D. Bandara and S. C. Burdette. "Photoisomerization in different classes of azobenzene". In: *Chem. Soc. Rev.* 41 (5 2012), pp. 1809–1825. DOI: `10.1039/C1CS15179G`. URL: `http://dx.doi.org/10.1039/C1CS15179G`.

[17] M. Lorenc, M. Ziolek, R. Naskrecki, J. Karolczak, J. Kubicki, and A. Maciejewski. "Artifacts in femtosecond transient absorption spectroscopy". In: *Applied Physics B* 74.1 (2002), pp. 19–27. ISSN: 1432-0649. DOI: `10.1007/s003400100750`. URL: `https://doi.org/10.1007/s003400100750`.

[18] M. Ziólek, M. Lorenc, and R. Naskrecki. "Determination of the temporal response function in femtosecond pump-probe systems". In: *Applied Physics B* 72.7 (2001), pp. 843–847. ISSN: 1432-0649. DOI: `10.1007/s003400100587`. URL: `https://doi.org/10.1007/s003400100587`.

[19] S. Kovalenko, A Dobryakov, J Ruthmann, and N P. Ernsting. "Femtosecond spectroscopy of condensed phases with chirped supercontinuum probing". In: 59 (Mar. 1999).

[20] P. Maierhofer. "Femtosecond Photodissociation Dynamics in Molecules studied by Time-Resolved Photoelectron-Photoion-Coincidence Spectroscopy". Master Thesis. Institute of Experimental physics, Graz University of Technology, 2016.

[21] M. Bainschab. "Multiphoton Ionization Channels in Molecules Investigated by Photoelectron-Photoion-Coincidence Spectroscopy". Master Thesis. Institute of Experimental physics, Graz University of Technology, 2016.

[22] S. Cesnik. "The Role of Molecular Symmetries in Non-adiabatic Relaxation Dynamics". Master Thesis. Institute of Experimental physics, Graz University of Technology, 2018.

[23] K. Unger, P. Salzmann, C. Masciullo, M. Cecchini, G. Koller, and A. M. Coclite. "Novel Light-Responsive Biocompatible Hydrogels Produced by Initiated Chemical Vapor Deposition". In: *ACS Applied Materials & Interfaces* 9.20 (2017). PMID: 28475310, pp. 17408–17416. DOI: `10.1021/acsami.7b01527`. eprint: `https://doi.org/10.1021/acsami.7b01527`. URL: `https://doi.org/10.1021/acsami.7b01527`.

[24] URL: `https://oceanoptics.com/support/software-downloads/`. (visited on 21.08.2018).

[25] Z. Mahimwalla, K. G. Yager, J.-i. Mamiya, A. Shishido, A. Priimagi, and C. J. Barrett. "Azobenzene photomechanics: prospects and potential applications". In: *Polymer Bulletin* 69.8 (2012), pp. 967–1006. ISSN: 1436-2449. DOI: `10.1007/s00289-012-0792-0`. URL: `https://doi.org/10.1007/s00289-012-0792-0`.

[26] M. Quick et al. "Photoisomerization Dynamics and Pathways of trans- and cis-Azobenzene in Solution from Broadband Femtosecond Spectroscopies and Calculations". In: *The Journal of Physical Chemistry B* 118.29 (2014). PMID: 24983924, pp. 8756–8771. DOI: `10.1021/jp504999f`. eprint: `https://doi.org/10.1021/jp504999f`. URL: `https://doi.org/10.1021/jp504999f`.

[27] A. Nenov et al. "UV-Light-Induced Vibrational Coherences: The Key to Understand Kasha Rule Violation in trans-Azobenzene". In: *The Journal of Physical Chemistry Letters* 9.7 (2018). PMID: 29504764, pp. 1534–1541. DOI: `10.1021/acs.jpclett.8b00152`. eprint: `https://doi.org/10.1021/acs.jpclett.8b00152`. URL: `https://doi.org/10.1021/acs.jpclett.8b00152`.

[28] A. Köhntopp, M. Dittner, and F. Temps. "Femtosecond Time-Resolved Dynamics of trans-Azobenzene on Gold Nanoparticles". In: *The Journal of Physical Chemistry Letters* 7.7 (2016). PMID: 26959865, pp. 1088–1095. DOI: `10.1021/acs.jpclett.6b00102`. eprint: `https://doi.org/10.1021/acs.jpclett.6b00102`. URL: `https://doi.org/10.1021/acs.jpclett.6b00102`.

[29] R. Borrego-Varillas et al. "Tracking azobenzene photoisomerization with sub-20-fs UV pulses". In: *2017 Conference on Lasers and Electro-Optics Europe European Quantum Electronics Conference (CLEO/Europe-EQEC)*. 2017, pp. 1–1. DOI: `10.1109/CLEOE-EQEC.2017.8087489`.

[30] Y. Hirose, H. Yui, and T. Sawada. "Effect of Potential Energy Gap between the n-π* and the π-π* State on Ultrafast Photoisomerization Dynamics of an Azobenzene Derivative". In: *The Journal of Physical Chemistry A* 106.13 (2002), pp. 3067–3071. DOI: `10.1021/`

jp0138375. eprint: `https://doi.org/10.1021/jp0138375`. URL: `https://doi.org/10.1021/jp0138375`.

[31] M. J. Frisch et al. *Gaussian 09, Revision C.01*. Gaussian, Inc., Wallingford CT, 2010.

[32] M. S. Zakerhamidi, A. Ghanadzadeh Gilani, and M. Moghadam. "Solvent Effects on the UV/ Visible Absorption Spectra of Some Aminoazobenzene Dyes". In: 1 (May 2012), pp. 1–8.

[33] P. Linstrom and W. Mallard, eds. *Evaluated Infrared Reference Spectra*. Coblentz Society, Inc. National Institute of Standards and Technology, Gaithersburg MD, 20899. DOI: `10.18434/T4D303`. (visited 12.06.2018).

[34] P. Heim. "Femtosecond Photodissociation Dynamics in Molecules studied by Time-Resolved PEPICO". Master Thesis. Institute of Experimental physics, Graz University of Technology, 2017.

[35] URL: `http://www.ozoptics.com/ALLNEW_PDF/DTS0094.pdf`. (visited on 20.07.2018).

[36] Part of invoice sent by Hellma Analytics Gmbh. URL: `http://www.hellma-analytics.com`.

List of Figures

List of Tables

Danksagung

Zuallererst möchte ich meinem Betreuer Assoc. Prof. Dr. Markus Koch danken. Ich hätte mir kein besseres Betreuungsverhältnis wünschen können. Abgesehen von der fachlichen Unterstützung und dem ausgezeichneten persönlichen Betreuungsverhältnis, will ich mich ganz besonders für das immense Vertrauen, das ich vom ersten Tag an genossen habe bedanken.

Herrn Univ.-Prof. Dr. Wolfgang Ernst möchte ich nicht nur für die Möglichkeit danken am Institut für Experimentalphysik meine Arbeit zu verfassen, sondern auch für kritische Diskussionen und Ideen ohne die weite Teile der Arbeit nicht so gelungen wären.

Das Team der Institutswerkstatt möchte ich für die ausgezeichnete Unterstützung danken. Amtsrat Uwe Seidl gilt mein besonderer Dank. Hilfe auch wenn spät abends noch eine Kleinigkeit gefertigt werden muss, lehrreiche Diskussionen und Ratschläge, das alles ist nicht selbstverständlich.

Meinen Laborpartnern Bernhard Thaler, Pascal Heim, Sascha Ranftl, Stefan Cesnik, Miriam Meyer und Werner Kleinsasser möchte ich für das angenehme und harmonische Arbeitsklima danken. Ganz besonderer Dank gilt Bernhard Thaler und Pascal Heim für die viele Zeit, die für Diskussionen und Unterstützung meiner Arbeit aufgegangen ist.

Assoc. Prof. Anna Coclite möchte ich für die Unterstützung, die viele Zeit und die angeregten Diskussionen danken.

Prof. Chen-Bin (Robin) Huang und Prof. Shang-Da Yang der National Tsing Hua University möchte ich für die großartige Lehre danken, welche mein Interesse für Ultrafast Optics geweckt hat.

Ralf Meyer möchte ich für viele (un)fachliche Diskussionen danken. So mancher Durchbruch wäre ohne den Blick von aussen nicht gelungen. Des Weiteren möchte ich mich bei allen Kollegen am Institut und an der Fakultät für das angenehme Klima und den herzlichen Umgang bedanken.

Meinen Freunden bei der Pfadfindergruppe Graz 11 und ganz besonders dem TI möchte ich für viele wunderschöne Jahre und viele die hoffentlich noch folgen danken. Ich wünsche allen ein herzliches „Gut Pfad!".

Meinen Freunden der ÖGM, Georg , Markus, Max, Patrick , Matthias, Lukas, Max, Thomas, Stefan, Christian, Stefan und Philipp möchte ich für unzählige schöne Erinnerungen an Ski / Berg und Segelausflüge danken.

Marco Alex und Natascha danke ich für zahllose Kletter und Boulderprobleme. Ich freue mich weiterhin auf Bouldern, Burek und Blues.

Meinen Eltern Gerald und Jutta, sowie meinem Bruder Clemens danke ich für die Unterstützung die ich mein Leben lang genossen habe und die Möglichkeit meinen Weg mit der Sicherheit zu gehen, dass ihr immer für mich da seid.

Zuletzt möchte ich Daniela danken, ohne dich hätte ich die Arbeit wahrscheinlich weder angefangen, noch so gut zu Ende gebracht. Dein Vertrauen und deine Unterstützung geben mir Sicherheit und Rückhalt für die ich nicht dankbar genug sein kann.